

ABSTRACT

ALSABBAGH, AHMAD HESHAM. Effect of Neutron Irradiation on Mechanical Behavior of Ultra-Fine Grained Low Carbon Steel – Application to Next Generation Fission Reactors. (Under the direction of K.L Murty).

Designing materials that can enhance performance and withstand extreme reactor operational conditions is a grand challenge in nuclear materials research. Irradiation induced defects result in embrittlement and hardening of reactor structural materials. Hence, the ability to mitigate the effects of radiation damage by removing in-situ radiation induced point defects is crucial to improving the mechanical properties of irradiated metals and enhancing their tailored response in irradiation environments. Ultra-fine grained steel provides large free surface to volume ratio, acting as sinks for migrating irradiation induced point defects. Annihilation of point defects at grain boundaries leads to lower net defect concentration in the grain interior compared to coarser grained counterpart thereby limiting radiation damage effects and resulting in enhanced radiation tolerant structural materials.

Neutron irradiation effects on ultra-fine grain (UFG) low carbon ferritic steel prepared by equal channel angular pressing (ECAP) have been examined. Counterpart samples with conventional grain (CG) sizes were prepared by annealing at high temperatures and have been irradiated alongside with the UFG ones for comparison. Samples were irradiated in the PULSTAR reactor at North Carolina State University to relatively low dose (0.001 dpa) and in the Advanced Test Reactor (ATR) at Idaho National Laboratory (INL) to 1.37 dpa.

Low dose irradiation of ultrafine grained carbon steel revealed minute radiation effects in contrast to the distinct radiation hardening and reduction of ductility in its CG

counterpart. At higher irradiation dose, atom probe tomography revealed manganese and silicon-enriched clusters in both UFG and CG steel after neutron irradiation. X-ray quantitative analysis showed that dislocation density in CG steel increased after irradiation while no significant change was observed in UFG steel, revealing better radiation tolerance. Quantitative correlations between experimental results and modeling were demonstrated based on irradiation induced precipitate strengthening and dislocation forest hardening mechanisms.

© Copyright 2014 Ahmad Alsabbagh

All Rights Reserved

Effect of Neutron Irradiation on Mechanical Behavior of Ultra-Fine Grained Low Carbon
Steel – Application to Next Generation Fission Reactors

by
Ahmad Hesham Hasan Alsabbagh

A dissertation submitted to the Graduate Faculty of
North Carolina State University
in partial fulfillment of the
requirements for the degree of
Doctor of Philosophy

Nuclear Engineering

Raleigh, North Carolina

2014

APPROVED BY:

Dr. K.L Murty
Committee Chair

Dr. Jacob Eapen

Dr. Mohamed Bourham

Dr. Ronald Scattergood

DEDICATION

To the person whom I miss a lot. To the soul of my father Hesham who provided me with the enthusiasm and motivation to get this work done.

BIOGRAPHY

Ahmad Alsabbagh was born in Amman, Jordan in 1985. He received his Bachelor of Science degree in Electrical Engineering in 2008 from University of Jordan, Amman, Jordan. In 2009, he started his graduate studies in the Nuclear Engineering department at North Carolina State University, Raleigh, NC, USA. In 2011, he received his Master degree in Nuclear Engineering. Then, he directly joined Prof. K.L Murty's research group to pursue his PhD studies.

ACKNOWLEDGMENTS

I would like to thank my PhD advisor Prof. K.L Murty for his continuous supervision and support throughout this dissertation. I am deeply obliged for his patience to train me how to investigate, present and publish scientific research. The training and guidance under Prof. Murty has reinforced my decision to explore my future as an academic researcher.

I would like to extend my gratitude to my PhD advisory committee members: Prof. Jacob Eapen, Prof. Mohamed Bourham, and Prof. Ronald Scattergood for their invaluable time and encouraging remarks.

This research was supported by the Advanced Test Reactor National Scientific User Facility (ATR-NSUF). I would like to acknowledge Prof. Ruslan Valiev of Ufa State Aviation Technical University for providing the UFG steel samples. I also want to thank the PULSTAR reactor staff at North Carolina State University, Mr. Scott Lassell, Mr. Gerry Wicks, Mr. Andrew Cook and Mr. Kerry Kincaid, for their assistance throughout the work of this dissertation. I would like also to express my sincere thanks to the Advanced Test Reactor (ATR) user facility team, Dr. Douglas Porter, Dr. Brandon Miller, Ms. Mary Catherine, Mr. Collin Knight, Dr. Leah Squires and Dr. James Cole for their valuable support during my experimental work at Idaho National Laboratory. I am also grateful, to the Center for Advanced Energy Studies (CAES) staff, Ms. Joanna Taylor and Ms. Jatu Burns for their help in testing the irradiated samples. I am grateful for the friendship and technical advices from the past and present colleagues, Dr. Walid Mohamed, Boopathy Kombaiah, Dr. Apu Sarkar, Peiman Roodposhti, Zoe Xiao, Alan Rominger, Dr. Cyrus Proctor and Wesley Holmes.

Finally, I would like to express my appreciation and thanks to my parents for their continuous help and support, and to my brothers and sisters who supported and helped me throughout my graduate studies. This work would never have been completed without the love, support, and patience of my wife Sarah.

TABLE OF CONTENTS

LIST OF TABLES	viii
LIST OF FIGURES	ix
Chapter 1. Introduction	1
Chapter 2. Background	7
2.1 Neutron Radiation Damage in Materials.....	7
2.1.1 Radiation Defects Induced by Intense Nuclear Radiation	9
2.2 Irradiation Effects on Reactor Pressure Vessel Ferritic Steels.....	12
2.3 UFG Materials Processed by ECAP	15
2.4 Irradiation Effects on Nano and Ultra-Fine Grained Materials - Literature Review	19
2.4.1 Reduced Defect Density	20
2.4.2 Irradiation Induced Amorphization.....	24
2.4.3 Irradiation Induced Recrystallization Processes	26
2.4.4 Computer Simulations Studies.....	31
Chapter 3. Materials and Irradiation Experiments	35
3.1 Materials and Sample Perpetration	35
3.1.1 ECAP Imposed Strain Calculations	39
3.2 Irradiation Experiments.....	42
3.2.1 Fast Neutron Spectrum Determination for the dpa Calculations	42
3.2.1.1 Foil Activation Technique.....	46
3.2.2 PULSTAR Irradiation Experiment	54
3.2.2.1 PULSTAR Experimental Characterization Methods	57
3.2.3 ATR Irradiation Experiment	58
3.2.3.1 ATR Experimental Characterization Methods	62
Chapter 4. Microstructural Characteristics	68
4.1 Grain Size Distributions	68
4.2 Irradiation Induced Defects	73
4.3 Irradiation Enhanced Segregation	78
4.4 Irradiation Induced Clustering	83
Chapter 5. Mechanical Properties	90
5.1 Irradiation Induced Hardening and Embrittlement	90
5.1.1 Vickers Micro Hardness	90
5.1.2 Nano Hardness	91
5.1.3 Tensile Test.....	95
5.2 Hardening Mechanisms.....	100
Chapter 6. Conclusions and Future Work.....	104
6.1 Summary and Conclusions.....	104
6.2 Future Work	105
References.....	107
Appendices.....	117
Appendix A.....	118

Dislocation Densities and Their Associated Error Calculations.....	118
Appendix B.....	123
Calculated Irradiation Induced Dislocation Density.....	123

LIST OF TABLES

Table 2.1: Number densities of I-loops and voids in coarse grain pure tungsten and UFG tungsten alloys after neutron irradiation at 600 °C to 2×10^{24} n/m ²	24
Table 3.1: The chemical composition of the steel material (weight percent).	36
Table 3.2: Characteristics of threshold reactions [90–92]	52
Table 3.3: Decay properties of the ¹⁵² Eu standard source [91].	53
Table 4.1: Mean grain size (μm) for both UFG and CG steel pre and post irradiation.	72
Table 4.2: Values of domain size (D_s), microstrain ($\langle \varepsilon_L^2 \rangle^{\frac{1}{2}}$) and dislocation density (ρ) for different samples obtained by Modified Rietveld analysis.	77
Table 5.1: Tensile data for CG steel before and after irradiation to different doses.	97
Table 5.2: Tensile data for UFG steel before and after irradiation to different doses.	97
Table 5.3: Estimated strength increment for both UFG and CG steels.	103
Table B.1: Irradiation-induced dislocation density for both UFG and CG steels.	123

LIST OF FIGURES

Figure 1.1: Light bulbs lit by the world's first electricity generated from nuclear power [2]... 5	5
Figure 1.2: Overview of the generations of nuclear energy systems [5]. 5	5
Figure 1.3: Temperature-neutron dose for various Gen IV reactor systems. The six Gen IV fission systems are: Very High Temperature Reactor (VHTR), Super Critical Water Reactor (SCWR), Lead Fast Reactor (LFR), Gas Fast Reactor (GFR), Sodium Fast Reactor (SFR), and Molten Salt Reactor (MSR) [10]. 6	6
Figure 2.1: Schematic of radiation damage event. Incident energetic particle hits the target material atoms (a) giving birth to PKA (b) which will be displaced and collide with other atom and cause it to be displaced (SKA) (c) displaced atoms will passage through the lattice causing additional knock-on atoms (d) finally radiation induced point defects (vacancy and interstitials) will be produced (e) [Adopted from T. Allen presentation]. 8	8
Figure 2.2: Fuel bin bundles irradiated at Fast Flux Test Facility (FFTF) to 75 dpa. While HT9 shows no swelling (a), D-9 austenitic clad exhibits pin-to-pin variations caused by swelling (b) [13]. 11	11
Figure 2.3: Calculated source and friction hardening components of yield stress as a function of the square-root of neutron fluence in mild steel [28]. 11	11
Figure 2.4: Radiation induced segregation at grain boundary of irradiated stainless steel [30]. 12	12
Figure 2.5: New pressure vessel that failed during its hydrostatic test following its fabrication.[37]. 14	14
Figure 2.6: Charpy impact energy-temperature plots for the unirradiated and irradiated KS-01 weld (0.37 wt.% Cu, 1.23 wt.% Ni) [38]. 15	15
Figure 2.7: Schematic illustration of the passage of a sample through the die in ECAP technique. 18	18
Figure 2.8: Schematic illustration of a typical ECAP facility (a) and the rotational scheme of the four processing routes in ECAP (b).[45, 48] 18	18
Figure 2.9: Void volume swelling in electron irradiated austenite stainless steel at different doses and grain sizes [53]. 20	20
Figure 2.10: Defect density vs. grain size in ion irradiated ZO_2 (a) and Pd (b) [54]. 23	23

Figure 2.11: Electrical resistivity change in irradiated nano and coarse grain gold samples as a function of irradiation dose [55].	23
Figure 2.12: Vickers microhardness as a function of neutron irradiation fluence for different grain size Stainless steel (a), Ni and Ni –W materials (b) [57].....	24
Figure 2.13: XRD profiles of CG TiNi (a) and NC TiNi (b) before and after the irradiation.	26
Figure 2.14: Grain size distribution for nanostructured 316 stainless steel, as deformed, after annealing at 350 °C for 24 h and after ion irradiation at 350 °C irradiation temperature [70].	28
Figure 2.15: Bright field TEM images of the Au, Pt, and Cu films in the initial state and after irradiation by Ar ions (gold and platinum) and Kr ions (copper) at different doses at room temperature [71].....	29
Figure 2.16: Average grain size vs ion irradiation dose. Experimental data vs model at low irradiation temperatures. Pt irradiated with Ar 500 keV ions at 298 K; Pt irradiated with 1 MeV Kr ions at 50 K and 298 K; Zr irradiated with 500 keV Kr ions at 20 K; Cu irradiated with 500 keV Kr ions at 50 K; and Au irradiated with 500 keV Ar ions at 50 K [71].....	30
Figure 2.17: Grain size distributions for UFG Ni before (red) and after (blue) proton irradiation at room temperature [56].....	31
Figure 2.18: Temperature accelerated dynamics (TAD) simulation snap shots for the radiation damage cascade at 300 K in copper at different time intervals to follow the defect kinetics. It shows the damage self-healing near the grain boundary. Black small spheres represent the lattice atoms before irradiation, green spheres are interstitial atoms, red cubes are vacancies, blue spheres are atoms that moves more than 1Å during an event, purple vectors represent the direction of moving atoms and the two horizontal lines in all the snap shots represent the grain boundary [77].....	34
Figure 3.1: Transmission electron microscopy (TEM) micrograph showing the grain size distribution for UFG steel ($d= 0.35\pm 0.18 \mu\text{m}$) (a) and electron back scattered diffraction (EBSD) micrograph for CG Steel ($d= 4.4\pm 1.8 \mu\text{m}$) (b).....	37
Figure 3.2: Vickers micro-hardness as a function of one hour annealing temperature.	37
Figure 3.3: Pre irradiation sample geometries for both UFG and CG steels.	38
Figure 3.4: Photographs of low carbon steel mini tensile sample (a) and tensile test grips (b).	38
Figure 3.5: Schematic illustration of Iwahashi model to calculate the imposed strain through ECAP when the arc of curvature angle (Ψ) equals 0°	39

Figure 3.6: Imposed strain due to 4 passes through the die versus the inner contact angle (Φ) between channels of the die (a). Schematic of ECAP die showing the inner contact angle (Φ) and the arc of curvature angle (Ψ) at the outer point of contact between channels of the die (b).....	42
Figure 3.7: Comparison of yield stress change in 316 steel following irradiation in three different facilities [81].	45
Figure 3.8: Cross sections for threshold reactions of interest [87].	53
Figure 3.9: Calculated HPGe detector efficiency vs. gamma energies.....	54
Figure 3.10: PULSTAR reactor (a) and the irradiation position in the PULSTAR reactor core (b).	56
Figure 3.11: Sample irradiation loading. Sealed quartz tube (a), Aluminum irradiation jig (b) and Aluminum irradiation stringer (c) lined with Cadmium layer (d).....	56
Figure 3.12: Experiment irradiation test assembly for ATR east flux trap position (a) and radial cross section view of the ATR reactor core, E-7 irradiation test position (b).	60
Figure 3.13: Sample holder, sample train and irradiation capsule loading and design.	61
Figure 3.14: Sample irradiation temperature calculated by a detailed finite element model of the experiment using ABAQUS code.....	61
Figure 3.15: Tensile test for radioactive steel samples conducted at Center for Advanced Energy Studies (CAES) using Instron machine.....	66
Figure 3.16: Needle-shape atom probe specimen geometry preparation using the focused ion beam technique.	67
Figure 4.1: TEM bright field micrographs for UFG steel before irradiation (a), after irradiation to 0.001 dpa (b), and after irradiation to 1.37 dpa (c).	70
Figure 4.2: TEM dark field micrographs for UFG steel before irradiation (a), after irradiation to 0.001 dpa (b), and after irradiation to 1.37 dpa (c).	70
Figure 4.3: Optical micrographs for CG steel before irradiation (a) and after irradiation to 0.001 dpa (b).	71
Figure 4.4: EBSD micrographs for CG steel before irradiation (a) and after irradiation to 1.37 dpa (b).	71

Figure 4.5: Grain size distributions of UFG steel (a, b, c) and CG steel (d,e,f) before and after irradiation to different doses.	72
Figure 4.6: TEM micrographs of CG steel unirradiated (a), CG steel irradiated to 0.001 dpa (b), CG steel irradiated to 1.37 dpa (c), UFG steel unirradiated (d), UFG steel irradiated to 0.001 dpa (e) and UFG steel irradiated to 1.37 dpa (f).	75
Figure 4.7: Typical two beam condition diffraction pattern used to observe the defects; same condition was used for all cases.	75
Figure 4.8: XRD profiles for unirradiated and irradiated (1.37 dpa) UFG and CG steels.	76
Figure 4.9: Whole XRD pattern fit for irradiated CG steel at dose 1.37 dpa using LS1 program.	77
Figure 4.10: Representation of three-dimensional reconstruction of UFG steel, (a) before and (b) after neutron irradiation by three-dimensional (3D) atom-probe microscopy.	80
Figure 4.11: Representation of three-dimensional reconstruction of conventional grained steel, (a) before and (b) after neutron irradiation by three-dimensional (3D) atom-probe microscopy.	81
Figure 4.12: Irradiation enhanced segregation at grain boundaries in UFG steel.	82
Figure 4.13: Post irradiation atomic arrangements around carbide precipitate in UFG steel. Atom concentrations inside the selected cylinder are shown in the right.	83
Figure 4.14: Comparison between random distribution of solutes in the matrix and the data obtained for both unirradiated (left) and irradiated CG steel (similar results were obtained from all the examined specimens for both CG and UFG steels).	86
Figure 4.15: Schematic showing the maximum separation method: (a) and (b) solute atom selection (the core atoms); (c) and (d) selection of other atoms within a distance L of the core atoms; (e) and (f) erosion of atoms within a distance E of any other atom. Selected solute atoms are shown black, selected matrix atoms are shown hatched, not selected solute atoms are drawn grey and non-selected matrix atoms are shown white [110].	87
Figure 4.16: Si-Mn-enriched cluster distribution post neutron irradiation for (a) CG and (b) UFG steel. The dimension of the analysis boxes is 20X20X100 nm.	88
Figure 4.17: Size distribution of Si-Mn- enriched precipitates in the neutron irradiated (a) UFG and (b) CG steels.	89
Figure 5.1: Micro-hardness before and after irradiation for both UFG and CG low carbon steels.	91

Figure 5.2: Load versus displacement for the 150 mN peak load experiment. Both UFG and CG steel were irradiated to 1.37 dpa..... 93

Figure 5.3: Nano hardness versus load for irradiated (1.37 dpa) and un-irradiated UFG and CG steels. 94

Figure 5.4: SEM images of nano indents at 210 mN for (a) Un-Irr CG (b) Irr-CG (c) Un-Irr UFG (d) Irr-UFG (1.37 dpa) low carbon steel..... 94

Figure 5.5: Engineering stress-strain curves for both steels (UFG and CG) before and after irradiation to different doses. 98

Figure 5.6: Correlation of yield (a) and tensile (b) strengths with hardness for UFG and CG ferritic steels before and after neutron irradiation..... 99

Chapter 1. Introduction

Energy is essential to economic development and improved quality of life. Nuclear energy is considered to be a relatively sustainable energy source that can provide clean (no carbon dioxide emissions) and economically efficient electric power. Nuclear reactors are capable of producing large amounts of power without the adverse environmental effects that accompany the use of coal or petroleum products. Although renewable energy sources (ex: wind, solar, water fall, etc) are also clean energy sources, limitations on their economic efficiency and reliability when used for base-load power generation are well recognized [1]. Electricity was generated for the first time using nuclear fission on December 20, 1951, and lit four 200-watt light bulbs (Figure 1.1) at the Experimental Breeder Reactor (EBR-I) at Idaho, USA [2]. However, in 1954 [3] the Union of Soviet Socialist Republic (USSR) built the world's first nuclear power plant to generate electricity for a power grid. In 1957 [4] the US had their first commercial nuclear power plant (Shippingport Reactor in Pennsylvania) to provide electrical energy to commercial grid. Since then the nuclear energy became a major contributor in producing the world electricity. During the past six decades reactors have been developed and improved. Nuclear reactor designs are usually categorized by “generation” (ex: I, II and III) based on their utilized technology and safety margins. Current operating reactors are considered second or third generation (Figure 1.2 [5]). At the beginning of 2014 there were 435 operating nuclear power reactors, operating in 31 countries [6]¹. The maximum number of operating reactors is located in North America region with 119 reactors

¹ All statistical data about current operating reactors are acquired from ref 6.

(100 USA, 19 Canada) while only 2 reactors are in Africa (South Africa). The most predominant design is pressure water reactor (PWR) with 274 reactors in operation around the world. The second type of existing reactors is the boiling water reactors (BWR) with 81 operating units. The remaining operating reactors are divided between pressurized heavy water reactors (PHWR), gas-cooled graphite-moderated reactor (GCR), light-water-cooled graphite-moderated reactor (LWGR) and fast breeder reactors (FBR). Seventy two reactors are currently under construction and they are distributed in 16 countries around the world. The age of a reactor is determined by its first grid connection. Seven reactors are considered the oldest reactors in operation, with 45 years of operation (first connected to the grid in 1969). Three of those forty five years old reactors are located in USA, two in India, one in Switzerland and one in Japan. Aging of reactors is defined by the International Atomic Energy Agency (IAEA) as a continuous time-dependent loss of quality of materials, caused by the reactor operating conditions [7]. After operating for long periods, nuclear structural materials will encounter gradual changes in their microstructures and mechanical properties causing them to not perform as expected leading to degradation in their performance capabilities [8].

In order to meet world-wide demand for energy, the concept for the next generation reactors was proposed. In year 2000, the US Department of Energy (DOE) launched the Generation-IV (Gen IV) initiative with international participation to expand nuclear energy and provide improved safety, economy and sustainability of the nuclear power plant systems [9]. Gen IV reactors will operate at higher temperatures, stresses, irradiation levels and in more severe corrosive environments compared to current operating reactors. Figure 1.3 [10]

shows the irradiation dose and temperature limits for diverse Gen IV proposed nuclear systems, and it demonstrate an overview of the severe operation conditions (in terms of operational temperature and displacement damage dose) for Gen IV compared to current generation reactors (generation II). Structural materials for advanced reactors like Gen IV reactors need to be capable of withstanding the severe operation conditions for those reactors without failure [11], and high performance materials will be critical for the success of those proposed reactors. Designing materials for those next generation reactors poses greater challenges because of the extreme operating conditions which require development of new materials more tolerant to those conditions. Progress is also required to further our understanding of materials for existing systems which will be considered as the bedrock for next generation reactors [12]. There are many requirements for reactor structural materials, and they differ based on the function of the material in the reactor. Along with materials' availability, affordability and adequate fabrication and joining properties, neutronic properties such as low absorption cross section for cladding materials need to be considered. Elevated temperature mechanical and thermal properties are crucial for reactor structural materials especially for future next generation reactors that will operate at high temperatures. Since materials for those proposed reactors will also exhibit high irradiation doses, resistance to irradiation-induced property changes is required [13].

The lifetime assessment of advanced nuclear structural materials requires an understanding of their behavior in a range of scales. Irradiation effects, mechanical properties and fracture mechanisms of advanced materials need to be considered. Experimental and simulation models are required to predict the materials' behavior in-service, under the severe

conditions of the advanced nuclear systems. While simulations address the long term behavior and provide fundamental understanding of advanced materials [14], experimental data will mimic the real environment that the materials will encounter during operation to understand the effect of neutron irradiation in reactor components. Current reactor materials are not expedient to be used for the new advanced reactors, and new concepts in materials design are needed to produce materials that are more radiation tailored and can sustain high amount of radiation damage while maintaining their mechanical properties.

Nanocrystalline (NC) and ultra-fine grained (UFG) materials have opened a new and fascinating path for research due to their unique and extraordinary properties [15, 16]. Large grain boundary area density provides free surfaces that attract, absorb and annihilate radiation induced defects [17, 18] thereby reducing radiation damage in the irradiated materials. In this dissertation, I studied the neutron irradiation damage in UFG ferritic low carbon steel and the consequent effects on their microstructural and mechanical properties. Irradiation experiments were performed at different doses; 0.001 dpa in PULSTAR reactor at North Carolina State University and 1.37 dpa in ATR reactor at Idaho National Laboratory. Post irradiation examinations were conducted in the nuclear materials laboratories at North Carolina State University (NCSU), Center for Advanced Energy Studies (CAES) and nuclear materials laboratories at Idaho National Laboratory (INL).

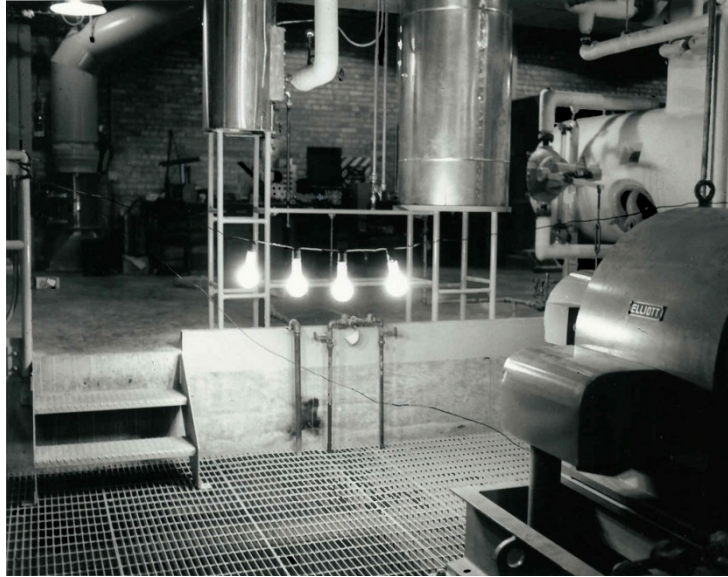


Figure 1.1: Light bulbs lit by the world's first electricity generated from nuclear power [2].

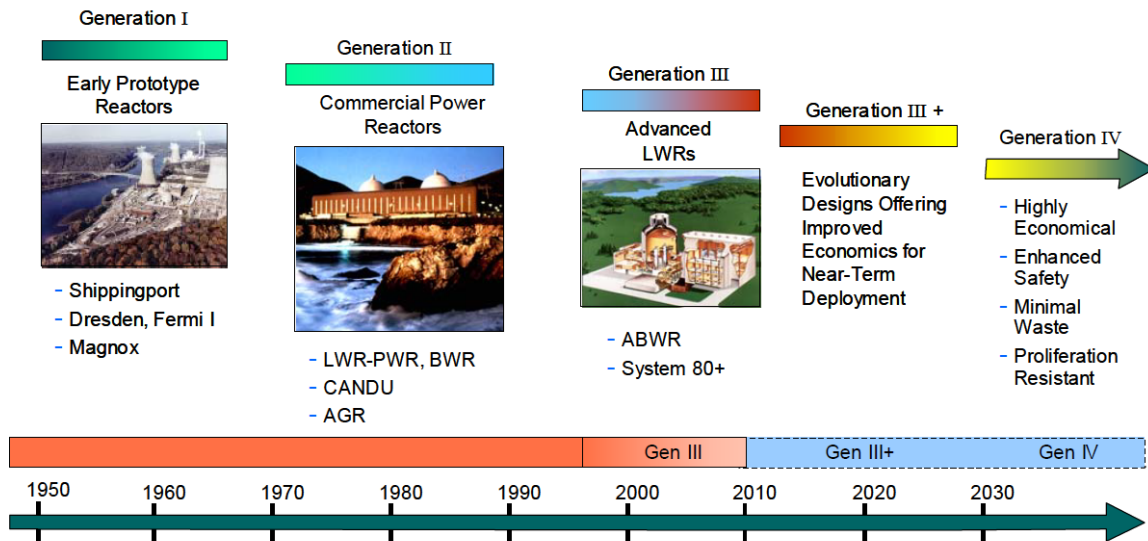


Figure 1.2: Overview of the generations of nuclear energy systems [5].

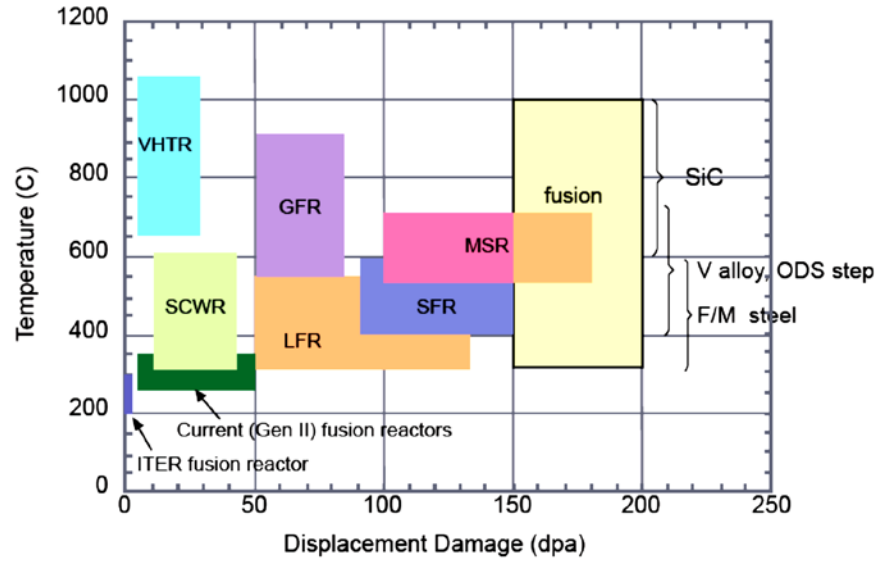


Figure 1.3: Temperature-neutron dose for various Gen IV reactor systems. The six Gen IV fission systems are: Very High Temperature Reactor (VHTR), Super Critical Water Reactor (SCWR), Lead Fast Reactor (LFR), Gas Fast Reactor (GFR), Sodium Fast Reactor (SFR), and Molten Salt Reactor (MSR) [10].

Chapter 2. Background

2.1 *Neutron Radiation Damage in Materials*

Neutrons produced in reactors by fission reaction have a high average energy (2 Mev) and can cause a severe damage in the reactor structural materials. Collisions of incoming neutrons with atoms in the crystal lattice of the target material cause part of the neutron energy to be transferred to the target atoms. If the transferred energy is higher than the displacement threshold energy of the target atom (~40 eV for steel [19]), the atom will be displaced from its lattice position giving birth to the primary knock-on atom (PKA). The PKA can induce subsequent lattice site displacements of other atoms (known as secondary knock-on atoms) if it possesses sufficient energy, or come to rest in the lattice at an interstitial site if it does not (Figure 2.1) thereby creating a Frenkel defect pair. This process continues creating a displacement cascade [20]. Materials' damage caused by irradiation consists of interstitials and vacancies (point defects). Interstitial is an atom that is located in a non-regular lattice site while vacancy is a missing lattice atom. Because of the thermal motion of the atoms in the lattice, self-annealing of the damage will take place and most of the radiation induced damage (about 80% [21]) will be annihilated by recombination between the vacancies and interstitials. However, the point defects which survive and stay in the matrix will give rise to significant changes in the microstructural and mechanical properties of the irradiated material. Depending on material, temperature and dose rate, excess vacancies and interstitials can be created at several orders of magnitude above thermal equilibrium. Defect populations in excess of equilibrium must be removed and the system

tries to move back to equilibrium. Defects can be removed in a number of ways: recombination, diffusion to surfaces, diffusion to particles or precipitates, diffusion to grain boundaries or cluster formation. However, neutrons have no charge and thus they are not affected by the electric fields surrounding the atomic nuclei and can travel for a long distance inside the target material, therefore the resultant irradiation damage is not localized but distributed through the solid.

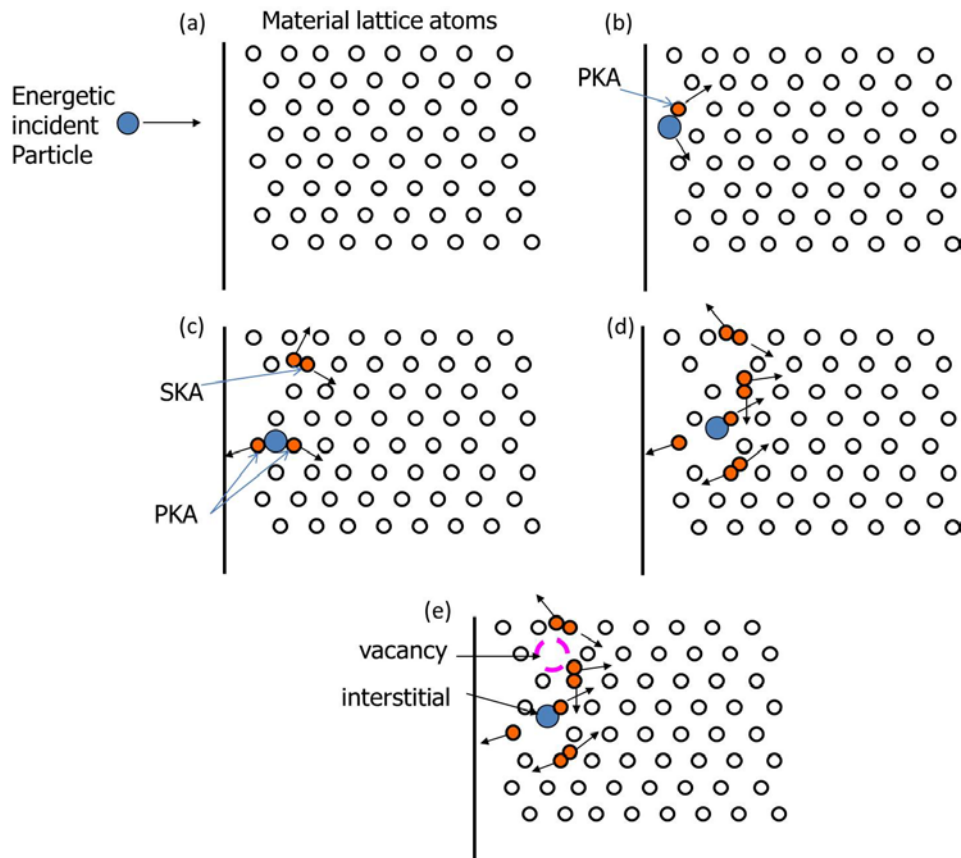


Figure 2.1: Schematic of radiation damage event. Incident energetic particle hits the target material atoms (a) giving birth to PKA (b) which will be displaced and collide with other atom and cause it to be displaced (SKA) (c) displaced atoms will pass through the lattice causing additional knock-on atoms (d) finally radiation induced point defects (vacancy and interstitials) will be produced (e) [Adopted from T. Allen presentation].

2.1.1 Radiation Defects Induced by Intense Nuclear Radiation

In nuclear applications, fission fragments and neutrons cause the bulk of the radiation damage since they have enough energy to cause displacements and are produced in sufficient number density to cause radiation damage. As explained earlier, the interactions between incoming energetic particles and material crystal lattice give rise to point defects (vacancies and interstitials). However, if large number of vacancies clusters together, it will result in “depleted zones”. Vacancy clusters can grow by absorbing other vacancies, and the resulting large vacancy clusters are called voids [22]. Voids are volume defects (3D) that have a profound influence on materials properties since they affect the density of the material. Voids will be more severe when they are filled by an inert gas which stabilizes it. Helium is a common inert gas that is produced by transmutation reactions in reactor structural materials such as Nickel ($^{59}\text{Ni} + ^1_0\text{n} \rightarrow ^{56}\text{Fe} + ^4_2\text{He}$). When the He fills the void it becomes stable, and it cannot be annealed out, so it becomes a permanent defect. Those voids that are stabilized by inert gas are called cavities or bubbles [23]. Cavities lead to volume expansion and decrease in the material density; this phenomenon is known as irradiation induced swelling [24]. If irradiation induced swelling continued to increase with fluence, then large increases in the size of the reactor structural materials could be expected, leading to catastrophic results. Some materials are more affected by swelling than others (Figure 2.2). However, irradiation induced swelling depends on irradiation temperature, dose, material composition and increased helium generation rates [13].

Moreover, irradiation also induces line defects (1D, ex: dislocations), planer defects [25] (2D, ex: dislocation loops) and volume defects [26] (3D, ex: precipitates or solute clusters) that will affect the microstructure of the irradiated material and consequently influence its physical and mechanical properties [19]. Interactions between dislocations themselves (forest strengthening) or dislocations and other volume defects impede the glide of those dislocations through the crystallite, increasing the stress needed for plastic deformation (friction hardening). However, radiation damage can also affect the stress required to start the dislocation motion on its glide plane (source hardening) [27]. Figure 2.3 illustrates the different effects of neutron irradiation on the two components that comprise yield stress in mild steel. While the friction stress follows the square root dependence, the source hardening decreases as neutron radiation fluence increases, because impurity atoms get attracted to radiation produced defects leading to reduced net concentration of interstitial atoms in solution available for locking the dislocation sources (this trend is opposite to that expected in fcc metals) [28].

Irradiation produces fluxes of point defects near surfaces, dislocations, grain boundaries and other defect sinks, different atomic species in irradiated alloys move at different rates and in different directions in response to these point defects (toward sinks or away from them). Enrichment or depletion of each element occurs according to the relative interaction of each element with the defect flux. Segregation of alloys elements leads to changes in alloys local compositions and can degrade the integrity of structural reactor materials. Figure 2.4 shows radiation induced segregation profile for different elements of neutron irradiated stainless steel.

Irradiation damage causes different effects in the microstructural, mechanical and physical properties of the irradiated materials, books by Was [19], Olander [20] and Murty et al. [29] introduce these effects and illustrate their consequences on the materials integrity.

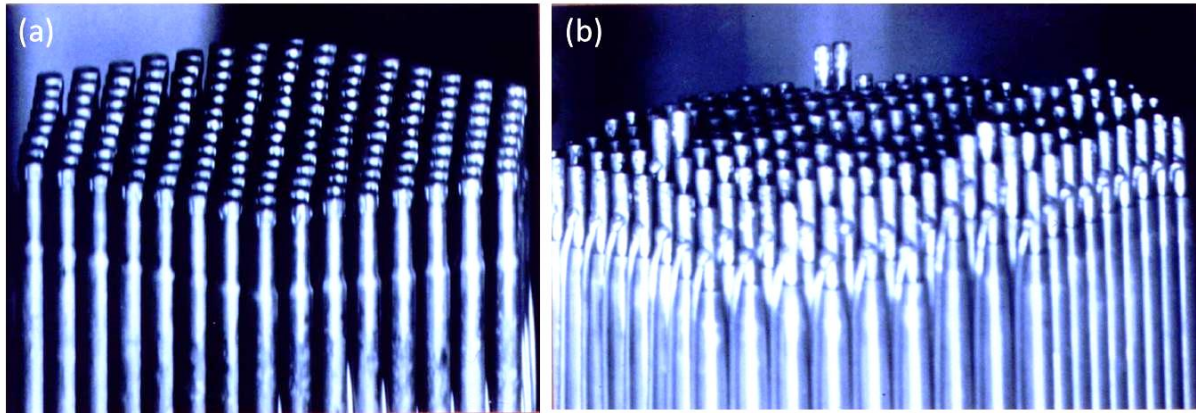


Figure 2.2: Fuel bin bundles irradiated at Fast Flux Test Facility (FFTF) to 75 dpa. While HT9 shows no swelling (a), D-9 austenitic clad exhibits pin-to-pin variations caused by swelling (b) [13].

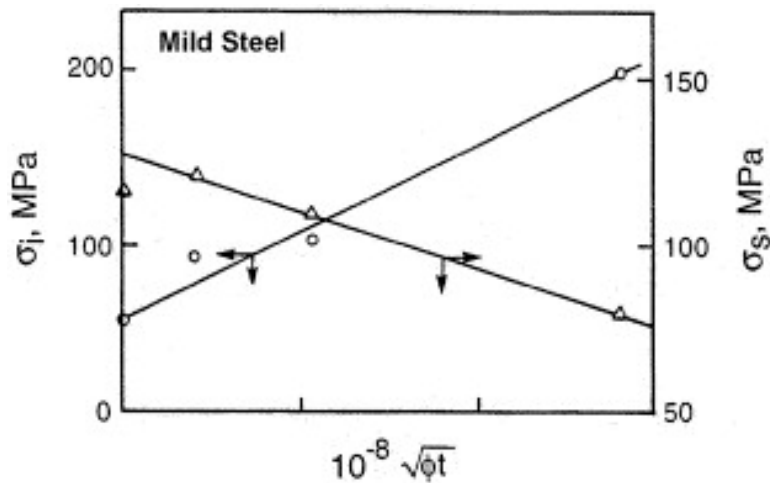


Figure 2.3: Calculated source and friction hardening components of yield stress as a function of the square-root of neutron fluence in mild steel [28].

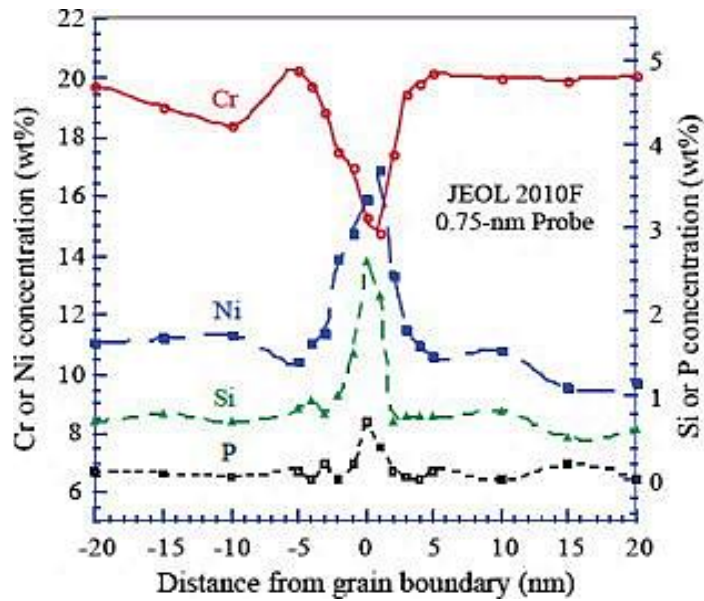


Figure 2.4: Radiation induced segregation at grain boundary of irradiated stainless steel [30].

2.2 Irradiation Effects on Reactor Pressure Vessel Ferritic Steels

Ferritic steels have been used widely as structural materials in light water reactors, but they suffer from irradiation hardening and embrittlement accompanied by increased ductile to brittle transition temperature (DBTT) and decreased upper shelf energy [27]. Previous studies have shown that major factors affecting low carbon steels under neutron irradiation are neutron fluence, irradiation temperature and chemical composition [31]. Due to their adequate mechanical properties and relatively low cost, ferritic steels are usually used to construct the reactor pressure vessel (RPV). The RPV serves as both a pressure and containment barrier for the radioactive fission products produced during the nuclear fission reaction, and thus plays a significant role in reactor safety. However, RPV is an irreplaceable

reactor component so if its mechanical properties degrade sufficiently, this means the end of the reactor life. The thickness of the vessel is about 20 cm with interior lined by a thin layer (5–10 mm) of an austenitic stainless steel to provide corrosion resistance to the reactor coolant [32]. Intensive studies have been conducted on the RPV steel to ascertain that the vessel will not fracture under any possible circumstances. Figure 2.5 shows a pressure vessel that failed during hydrostatic testing (this is not due to irradiation but it shows the catastrophic results that may occur if the pressure vessel steel fails). Since the RPV is relatively far from the reactor core, the fast neutron flux is three to four orders of magnitude lower at the RPV compared to core internal structures (For most Western-type light water reactor (LWR) pressure vessels, the flux of neutrons with energy higher than 1 MeV at the irradiation peak location of an RPV is around 10^{10} n.cm⁻².s⁻¹ while it is 6×10^{13} n.cm⁻².s⁻¹ for reactor internal structures) [33]; however, it is still of sufficient intensity to induce changes in the properties of ferritic steels. In order for the reactor license to be renewed, the integrity of the RPV steel needs to be assured. Thus the reactor vessel surveillance program (RVSP) was initiated to provide the needed data to examine the adequacy of the RPV steel for maintaining its purpose. When the reactor is designed and built, samples from different locations of the RPV steel were added to an irradiation capsule known as “Surveillance Capsule” which was loaded relatively close to the reactor core (closer than the RPV) to ensure that the surveillance samples will reach higher damage level than the RPV steel itself. Material specimens exposed to neutron irradiation in surveillance capsules are withdrawn periodically from the reactor vessel and fracture toughness test data are obtained from them to assure that its fracture toughness is above a certain level of the required safety margin

[34]. Neutron irradiation can cause severe elevation of the brittle fracture temperatures in steels due to precipitation and defect hardening. Figure 2.6 shows the effect of neutron irradiation on the DBTT of RPV steel and the data clearly reveals the increase in the transition temperature and the decrease of the shelf energy. The primary mechanism of embrittlement in RPV steels is the hardening formed by irradiation induced fine scale microstructural features [35]. In steels with high copper levels, high number density of copper-enriched precipitates is formed during neutron irradiation, acting as a major contributor in degrading RPV steel mechanical properties [36]. However, more data is needed to examine irradiation effects on ferritic steels with different compositions and microstructures toward development of radiation tolerant ferritic steels.

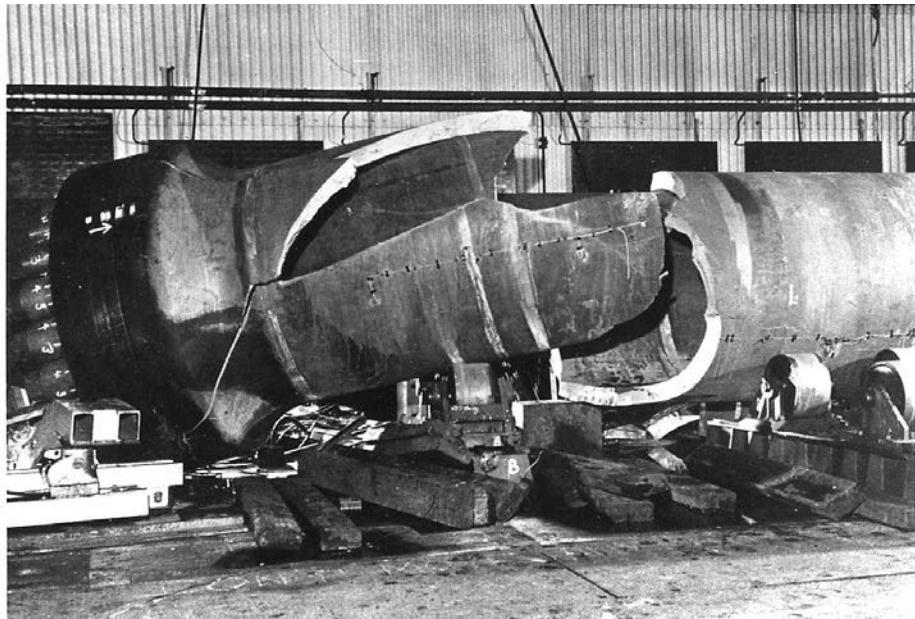


Figure 2.5: New pressure vessel that failed during its hydrostatic test following its fabrication.[37]

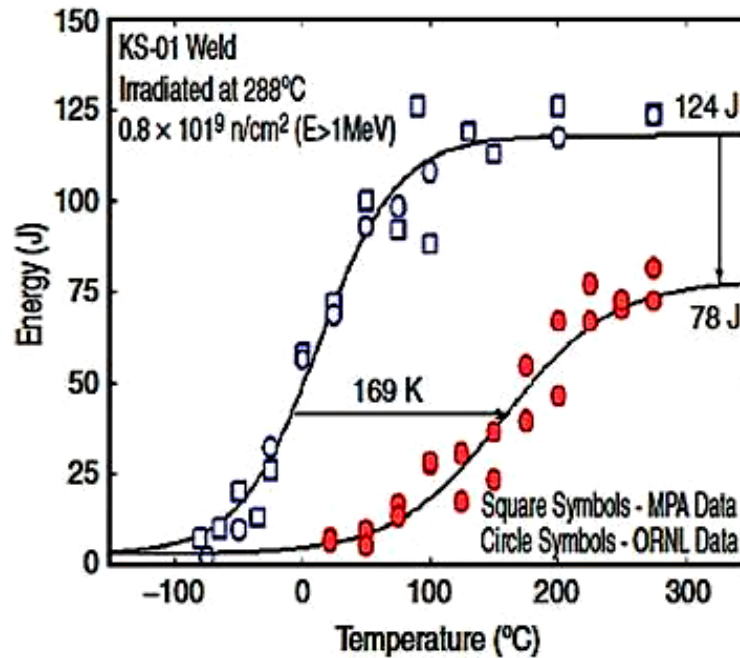


Figure 2.6: Charpy impact energy-temperature plots for the unirradiated and irradiated KS-01 weld (0.37 wt.% Cu, 1.23 wt.% Ni) [38].

2.3 UFG Materials Processed by ECAP

While nano grained materials have a grain size less than 100nm, ultra-fine grained materials are with grain size between 100nm-1000nm [39]. UFG and NC materials can be produced by two major approaches [40]: bottom-up methods which involve consolidating nano or ultra-fine grained materials from the atomic scale; examples of methods that use this approach are electro-deposition [41] and inert gas condensation [15, 42]. The second method is the top-down approach that involves refining the coarse grain materials to produce the UFG and NC ones. Severe plastic deformation (SPD) is the common technique for this

approach, in which very high plastic strain is imposed in the material to refine its grain size [43]. Two basic procedures for SPD are commonly used to produce the ultra-fine grained materials: high pressure torsion (HPT) [44] and equal channel angular pressing (ECAP) procedure [45, 46]. While HPT produces relatively small size specimens, ECAP technique provides large bulk metals and considered as one of the most efficient techniques in producing ultra-fine grained materials by SPD [46]. ECAP process involves imposing a very high plastic strain to the polycrystalline material by passing it through a special die. The die is constructed of two channels which are equal in cross-section and intersect at an angle of Φ (Figure 2.7). The total strain accumulated by passage through the die depends on the channels' intersecting angle (Φ), outer arc of curvature angle (Ψ) and the number of passages through the die (N_{pass}) [47]. Figure 2.8a [48] shows a schematic illustration of ECAP processing where the X plane (perpendicular to the pressing direction), and Y, Z planes (side and top faces of the pressed sample) have the same dimensions as of the original specimen. The combination of high pressure and large uniform shear strain that is applied on the material results in a considerable refining of the grains. Thus, larger grain boundary surface area per unit volume will be produced. Since the grains are oriented in different directions, dislocations will need more energy to travel to the adjacent grains and this impediment of dislocation movement will prevent the plastic behavior of the material, leading to improvement in the strength.

Since the cross-sectional area of the work piece remains the same when it processed through the die, there is no geometric restriction on the strain that can be achieved, and it is possible to repeat the pressings for several cycles to obtain exceptional high strains [46]. The

sample is inserted in the die and then it is removed, rotated and reinserted again in the die. Four processing routes have been identified to define the rotational angle between each passage through the die (A, B_a, B_c and C) [45, 46]. Figure 2.8b [45] illustrates the difference between the ECAP processing routes; in route A the sample is inserted in the die for the second pass without any rotation. For route B_a the sample is rotated 90° in alternate direction. In route B_c the sample is rotated 90° in the same direction after each pass while in route C the sample is rotated through 180° between each pressing. It was found that route B_c is the most efficient processing route [49] because of the eventual restoration of the cubic element after 4n passes, where n is an integer. Many factors made the ECAP one of the unique industrial processes [50] such as the enormous deformation without changing the cross-sectional dimensions, the large size production of bulk metals, the uniform structure of the worked material and the relatively low pressure that is needed for extrusion.

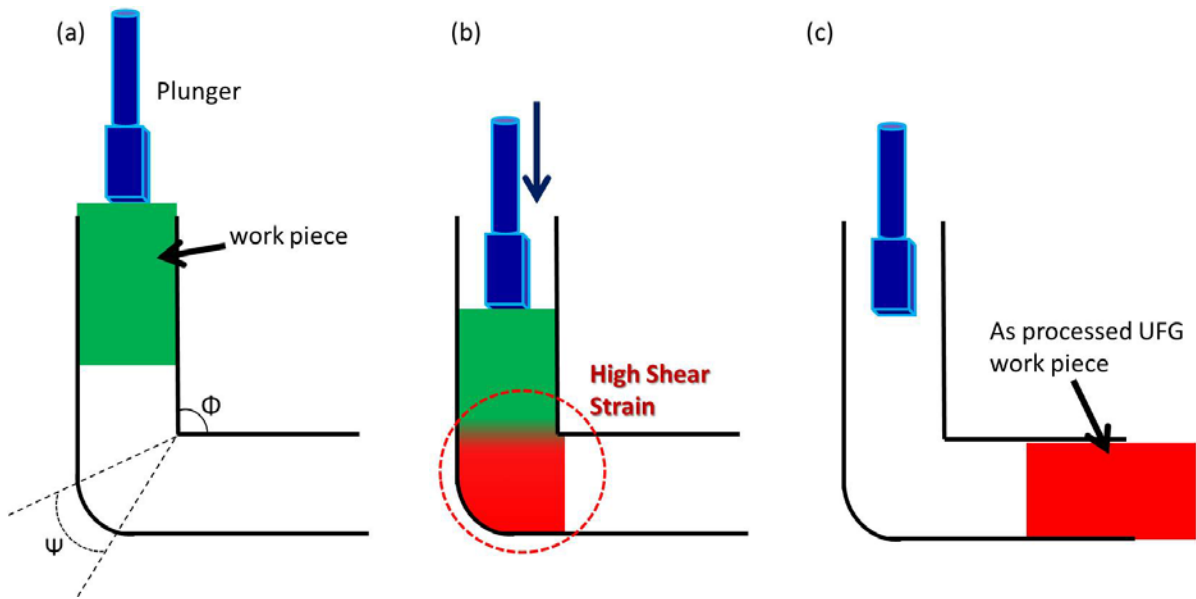


Figure 2.7: Schematic illustration of the passage of a sample through the die in ECAP technique.

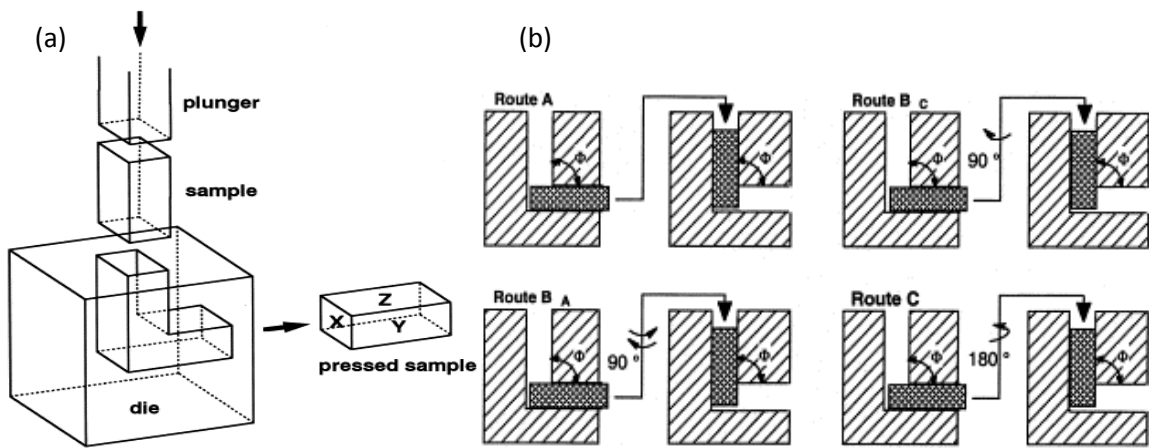


Figure 2.8: Schematic illustration of a typical ECAP facility (a) and the rotational scheme of the four processing routes in ECAP (b).[45, 48]

2.4 Irradiation Effects on Nano and Ultra-Fine Grained Materials - Literature Review

Nano and ultra-fine structured materials have opened a new and fascinating path in materials research due to their unique and improved properties. Small grain size enhances the strength of the material (Hall-Petch relationship), indicating promising potential for these materials. High grain boundary density provides large free surface to volume ratio and offers short circuit diffusion paths toward grain boundaries. Moreover, Nano structured materials also showed higher heat capacity and enhanced magnetic properties as compared with conventional materials [15].

Extreme operating conditions in advanced reactors accelerate the aging process in reactor structural materials leading to degradation in their performance and eventual failure. Recombination of radiation-induced point defects at free surfaces such as grain boundaries is energetically favorable and is one mechanism whereby the rate of radiation damage build-up can be retarded. Hence, large volume fraction of grain boundaries in UFG materials can act as an important sink for radiation damage; it provides free surfaces that attract, absorb and annihilate point and line defects produced by neutron radiation exposure. Thus, high grain boundary density may prevent, delay or minimize the effects of radiation damage in materials [51, 52].

The influence of materials' grain size on its irradiation resistance was first observed in early seventies by Singh [53] who illustrated that void formation is reduced by decreasing grain size. Using austenite stainless steel irradiated by 1 MeV electrons, Singh showed that voids reach a clearly resolvable size at higher doses as the grain size decreases. He also

demonstrated that the larger the grain size the higher the void volume swelling at all dose levels (Figure 2.9) indicating that ultra-fine grained materials show better resistance to irradiation induced swelling.

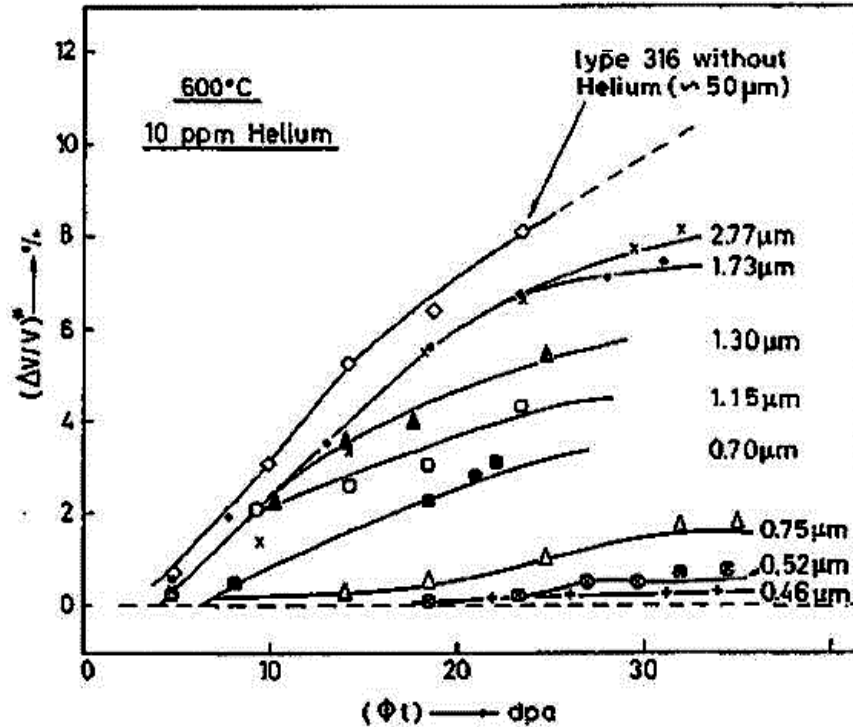


Figure 2.9: Void volume swelling in electron irradiated austenite stainless steel at different doses and grain sizes [53].

2.4.1 Reduced Defect Density

Rose et al. [54] studied the defect evolution in nanostructured materials using transmission electron microscopy (TEM). They showed that defect densities in nanocrystalline Pd (metallic material) and ZrO_2 (ionic material) prepared by inert gas

condensation technique (IGC) and irradiated by 4 MeV Kr ions at room temperature, decrease as the grain size decreases (Figure 2.10). Defects are not present for grain sizes below 30 nm (Pd) and 15 nm (ZrO₂). The difference in the defect free grain size is due to different diffusion lengths for point defects in palladium compared to zirconium oxide. Later, Chimi et al. [55] used the electrical resistivity measurements to investigate the radiation resistance of nanocrystalline gold and compared it to coarse grained counterparts. Results indicate that rate of resistivity change in nanocrystalline Au irradiated by C ions at 300K is smaller than in its coarse grain counterparts, owing to the decrease of defect accumulation rate in the nanocrystalline material (Figure 2.11). Analogous results from other studies [56] suggested good irradiation resistance of nanocrystalline materials due to the lower irradiation induced defect densities. Matsuoka et al. [57] studied the effects of neutron irradiation on UFG SUS316L stainless steel developed by mechanical alloying (MA) and NC Ni and Ni–W prepared by electrodeposition technique. Their TEM observations revealed defect-free zones along grain boundaries in SUS316L steels, suggesting that the grain boundaries are acting as sinks for radiation induced defects. Vickers microhardness data of the studied materials with different grain sizes were reported before and after neutron irradiation to 1.14×10^{24} n/m² at 290 °C. Figure 2.12 illustrates that while irradiation causes increased hardness in coarse grain stainless steel samples, the hardness of the UFG hot isotactic pressed (HIP) SUS316L stainless steel (grain size of 0.1 and 0.3 μm) was almost unchanged. Similar results were obtained in the case of NC Ni (grain size 50 nm). It's important to note that NC Ni (grain size of 50 nm) exhibited grain growth after irradiation up to one order of magnitude (50 nm to 500 nm). Thus, grain growth may be responsible to compensate for the irradiation hardening

in this case. Interestingly, large increase in the hardness of the NC Ni-W was noted after irradiation in spite of the grain growth from 6 to 8.5 nm. For Ni-W material with grain size less than about 10 nm, it was observed that as the grain size decreases, the hardness will decrease (inverse Hall–Petch relationship) [58]. So, this increase in hardness might be caused mainly by the grain growth during the irradiation. Another neutron irradiation study was carried out by Kurishita et al. [59]. They studied neutron and ion (He) irradiation effects on ultra-fine grained tungsten alloy (W-(0.25-0.8) wt% TiC) fabricated by mechanical alloying (MA) in different gas atmospheres (Ar, H₂). After neutron irradiation both interstitial-type dislocation loops (I-loop) and void number densities were calculated using TEM (Table 2.1). Void density decreases drastically in UFG W-0.5TiC alloys compared to CG pure tungsten, whereas I-loop number densities didn't show significant difference. Irradiation hardening was assessed utilizing Vickers micro hardness test. CG pure tungsten exhibited an increase in hardness after neutron irradiation ($\Delta HV=98$) while UFG alloys didn't show significant change indicating better irradiation hardening resistance. Kurishita et al. also showed that after ion irradiation by 3MeV He at 550 °C, the critical fluence for exfoliation and surface cracking along grain boundaries will occur at 2×10^{22} He/m² in the coarse grain commercial tungsten, while it will occur at about 10 times higher fluence (3×10^{23} He/m²) in case of UFG W-0.5TiC-H₂, illustrating higher surface damage resistance. Recently, Sun et al. [60] also observed lower densities of helium bubbles in the irradiated UFG Fe-14Cr-16Ni (wt%) austenite steel (grain size of 400 nm) compared to the CG counterparts (grain size of 17 μm) after irradiation with 100 keV helium ions at room temperature. Consequently, less irradiation hardening values were measured in the UFG material.

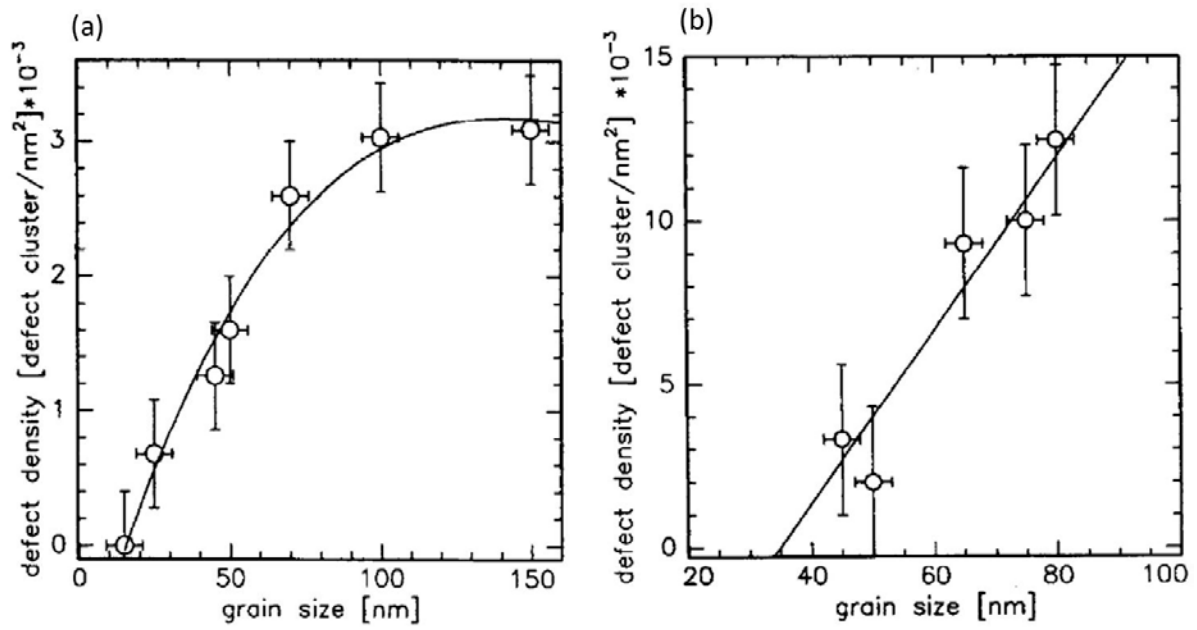


Figure 2.10: Defect density vs. grain size in ion irradiated ZO_2 (a) and Pd (b) [54].

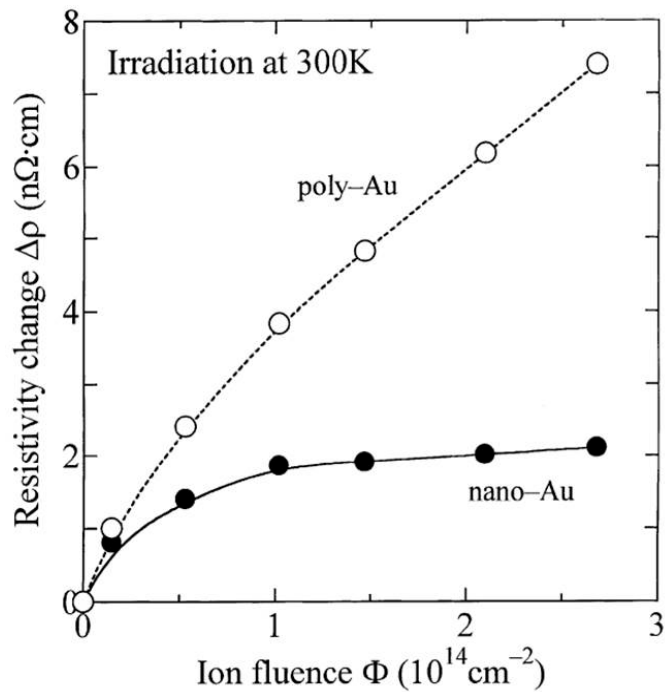


Figure 2.11: Electrical resistivity change in irradiated nano and coarse grain gold samples as a function of irradiation dose [55].

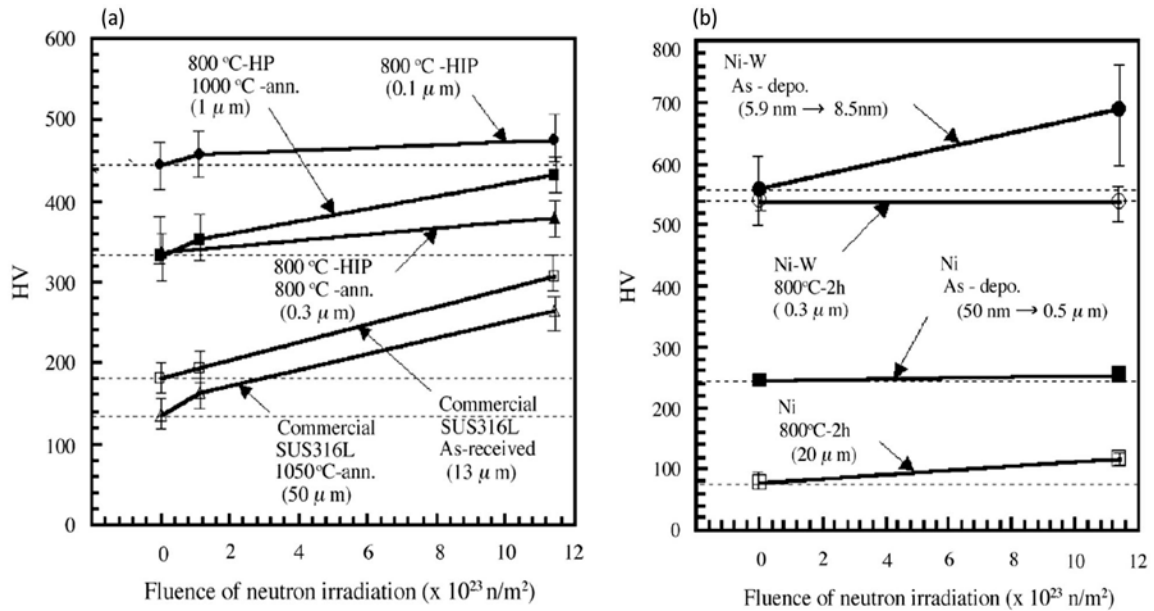


Figure 2.12: Vickers microhardness as a function of neutron irradiation fluence for different grain size Stainless steel (a), Ni and Ni –W materials (b) [57].

Table 2.1: Number densities of I-loops and voids in coarse grain pure tungsten and UFG tungsten alloys after neutron irradiation at 600 °C to 2×10^{24} n/m².

Number density (N/μm ³)	Pure W	W-0.5TiC-H ₂	W-0.5TiC-Ar
I-loop	6×10^3	5×10^3	5×10^3
Void	125×10^3	32×10^3	25×10^3

2.4.2 Irradiation Induced Amorphization

Amorphization induced by irradiation is affected by four factors: type of the material, grain size, temperature and irradiation dose [51]. Irradiation often enhances amorphization in coarse grained materials [61, 62]. However, experimental results have controversial results regarding radiation induced amorphization in nano and ultra-fine structured materials [63–

65] . Meldrum et al. [63], found that nanocrystalline zirconia (ZrO_2) irradiated by Xe ions can be amorphized at a dose of 0.9 dpa, while coarse grain counterparts didn't show any evidence of amorphization even after irradiation to 640 dpa. On other hand, Shen et al. [66] showed that NC ionic material ($MgGaO_4$) has an enhanced irradiation amorphization resistance. While coarse grain $MgGaO_4$ began amorphization at fluence of around 5×10^{19} Kr/m², NC counterparts remained crystalline even at higher fluences. Similar results were obtained by Kilmametov et al. [64] where nanocrystalline $Ti_{49.5}Ni_{50.6}$ showed better irradiation amorphization resistance than its coarse grain counterparts. Figure 2.13 shows X-ray diffractograms for Ar⁺ ion irradiated TiNi and it illustrates that CG material exhibits increasing broad background with increasing intensity even at relatively small dose (0.4 dpa) indicating partial amorphization. Moreover, in case of CG TiNi both (100) and (200) peaks disappear after irradiation. In contrast, the NC TiNi shows no amorphous background even after irradiation to 5.6 dpa and the peak (200) was still shown revealing smaller tendency for irradiation induced amorphization. The article by Ovid'ko and Sheinerman [67] demonstrated that in nanostructured materials, two scenarios may affect radiation induced amorphization: first, grain boundaries act as sinks for radiation damage leading to reduced defect densities and thus hinder and suppress amorphization driven by defect accumulation. Secondly, nanostructured materials provide high-density of free surfaces (grain boundaries) which characterized by excess energy and essentially contribute to the total energy of the crystalline state. Ovid'ko and Sheinerman suggested a theoretical model to explain the contradiction in the experimental results and delineate the two different scenarios mentioned above. More

experimental results on the effect of irradiation on amorphization of NC and UFG materials are summarized in reviews [17, 18].

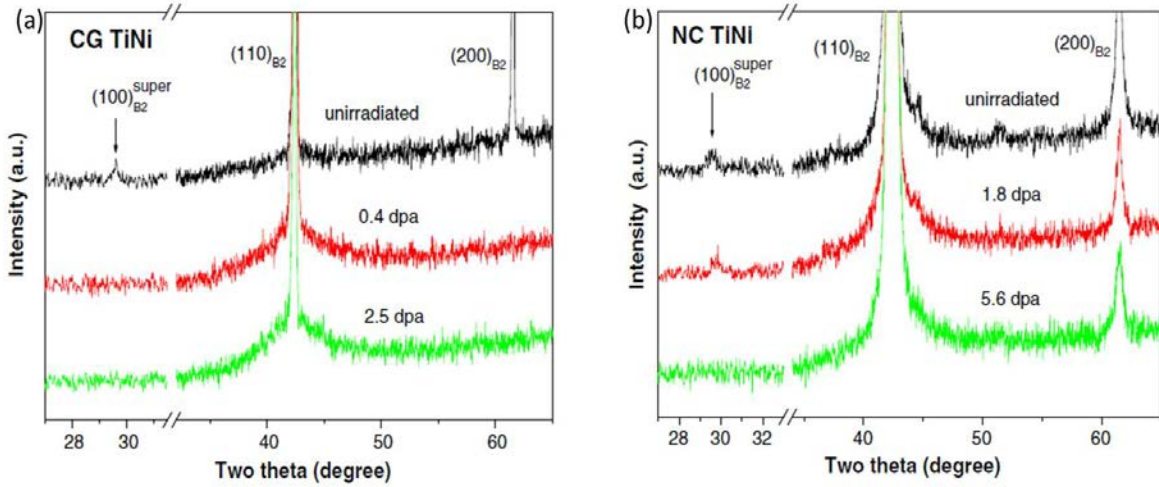


Figure 2.13: XRD profiles of CG TiNi (a) and NC TiNi (b) before and after the irradiation.

2.4.3 Irradiation Induced Recrystallization Processes

Grain growth may occur during irradiation if the volume of the irradiation displacement cascade exceeds the grain size or overlaps the grain boundaries. Hence, recrystallization occurs during cooling and shrinking of the cascade resulting in grain growth [68]. It was shown by TEM that after irradiation with Kr^+ ions at room temperature, grain growth was clearly observed in nanocrystalline Pd [69]. Radiguet et al. [70] investigated the effect of irradiation on the microstructure of nanostructured 316 austenite stainless steel produced by high pressure torsion technique (HPT). They found that while irradiation with

iron ions at 350 °C causes grain growth in the material (40 nm before irradiation and 60 nm post irradiation), annealing the NC stainless steel at 350 °C (same as irradiation temperature) for 24 hours has no influence on the average grain size (Figure 2.14) indicating that the observed grain growth in the irradiated samples was not thermally activated but instead it was due to irradiation damage. Kaoumi et al. [71] showed that grain growth in irradiated materials can be divided into three regions: non thermal growth at low irradiation temperatures (below 0.15-0.22 T_m) (Figure 2.15 shows grain-growth induced by ion irradiation at room temperature), thermally assisted region where both irradiation effects and thermal motions may increase the grain growth rate, and high temperature region where grain growth is dominated by the increase of irradiation temperature (i.e., thermal effect). They proposed a model to describe grain growth in the low temperature region where grain growth is induced by ion irradiation damage. After the collision displacement cascade, the remaining kinetic energy of the recoil atoms is thermalized within the crystal lattice resulting in a short lived thermal spike in a very localized region. If the spike occurs near grain boundary, atoms which are thermally activated within the thermal spike region can jump across the boundary resulting in grain boundary migration and hence grain growth. The model relates the average grain size with the ion dose and it illustrated a good agreement with experiments (Figure 2.16). However, some studies showed a contradictory behavior of nano and ultra-fine grained materials under irradiation. Nita et al. [56, 72] observed grain size refinement in SPD Ni following irradiation with 590 MeV protons at room temperature and Figure 2.17 elucidated the average grain size deduced from TEM observations. Average grain size for UFG Ni decreased from 115 nm before irradiation to 38 nm after irradiation. They suggested

that the grain refinement may be due to migration of defect clusters produced by irradiation to sub-grain boundaries and forming a cell structure that eventually may result in the formation of new smaller grains. In order to clarify the mechanisms of recrystallization and grain growth in nano and ultra-fine structured materials, more studies are needed on irradiation experiments on different materials at various irradiation temperatures and doses to demonstrate the influence of irradiation on the average grain size.

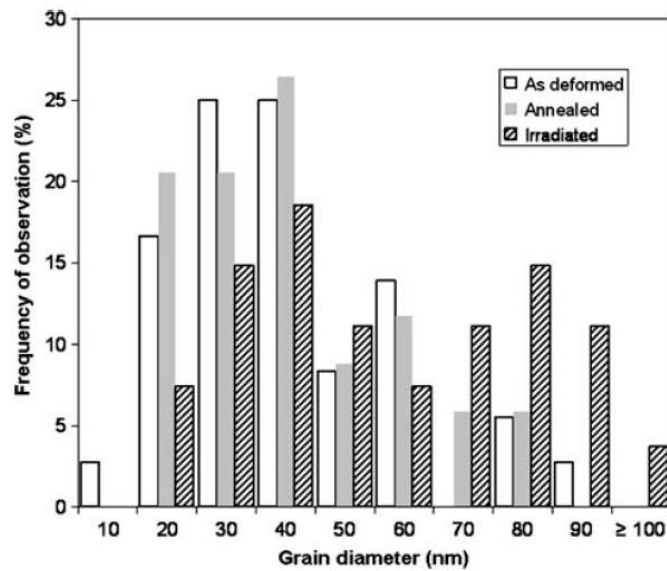


Figure 2.14: Grain size distribution for nanostructured 316 stainless steel, as deformed, after annealing at 350 °C for 24 h and after ion irradiation at 350 °C irradiation temperature [70].

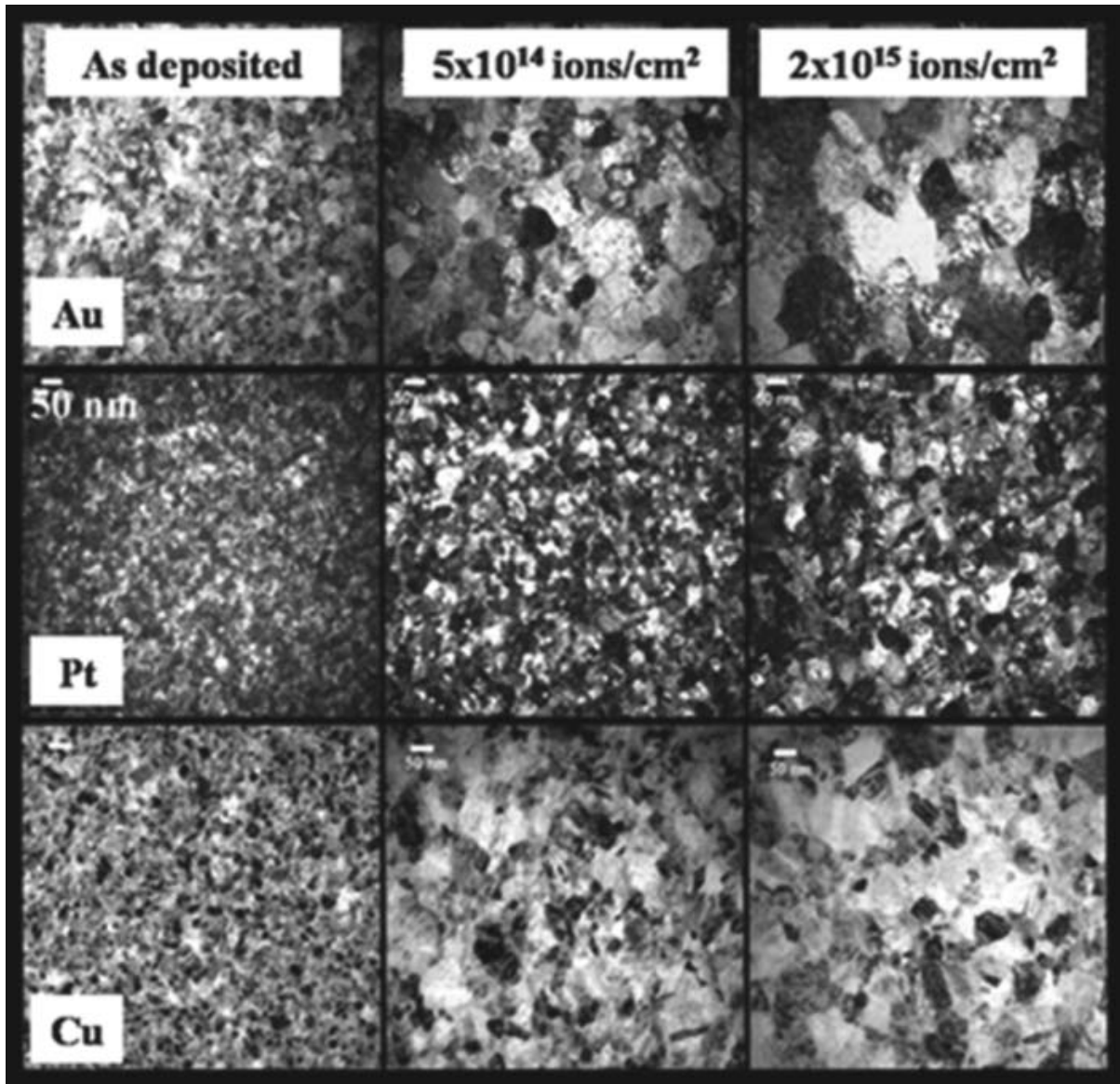


Figure 2.15: Bright field TEM images of the Au, Pt, and Cu films in the initial state and after irradiation by Ar ions (gold and platinum) and Kr ions (copper) at different doses at room temperature [71].

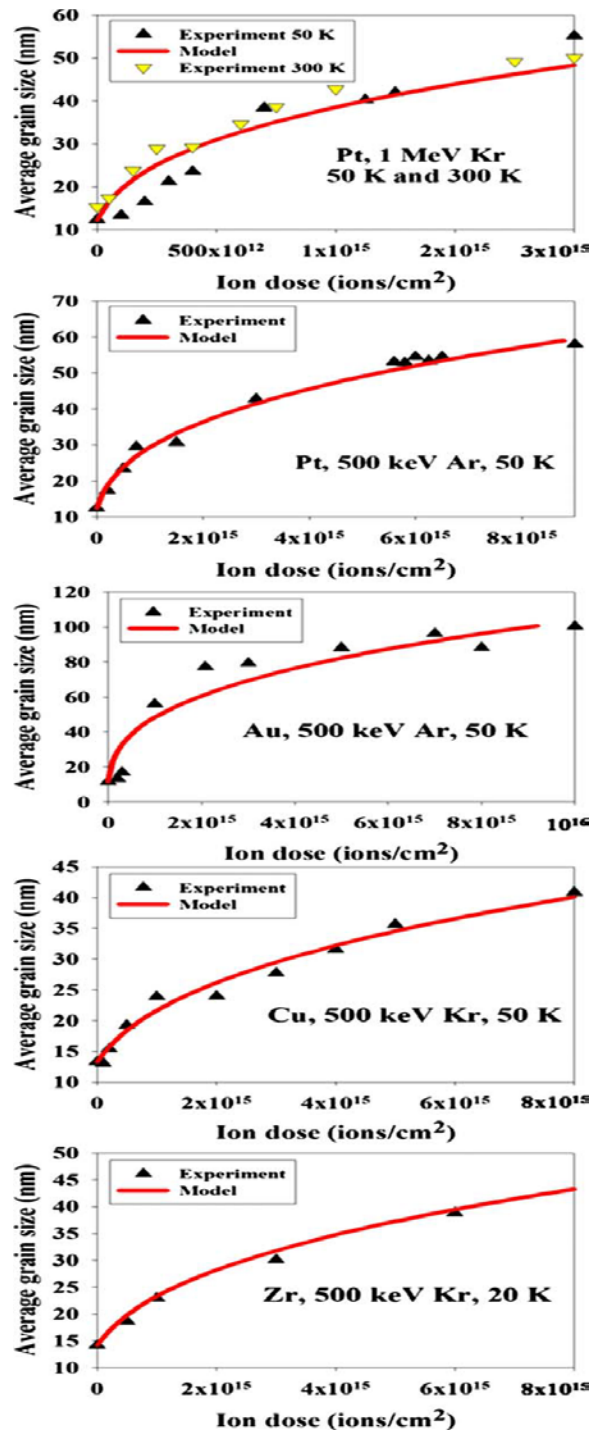


Figure 2.16: Average grain size vs ion irradiation dose. Experimental data vs model at low irradiation temperatures. Pt irradiated with Ar 500 keV ions at 298 K; Pt irradiated with 1 MeV Kr ions at 50 K and 298 K; Zr irradiated with 500 keV Kr ions at 20 K; Cu irradiated with 500 keV Kr ions at 50 K; and Au irradiated with 500 keV Ar ions at 50 K [71].

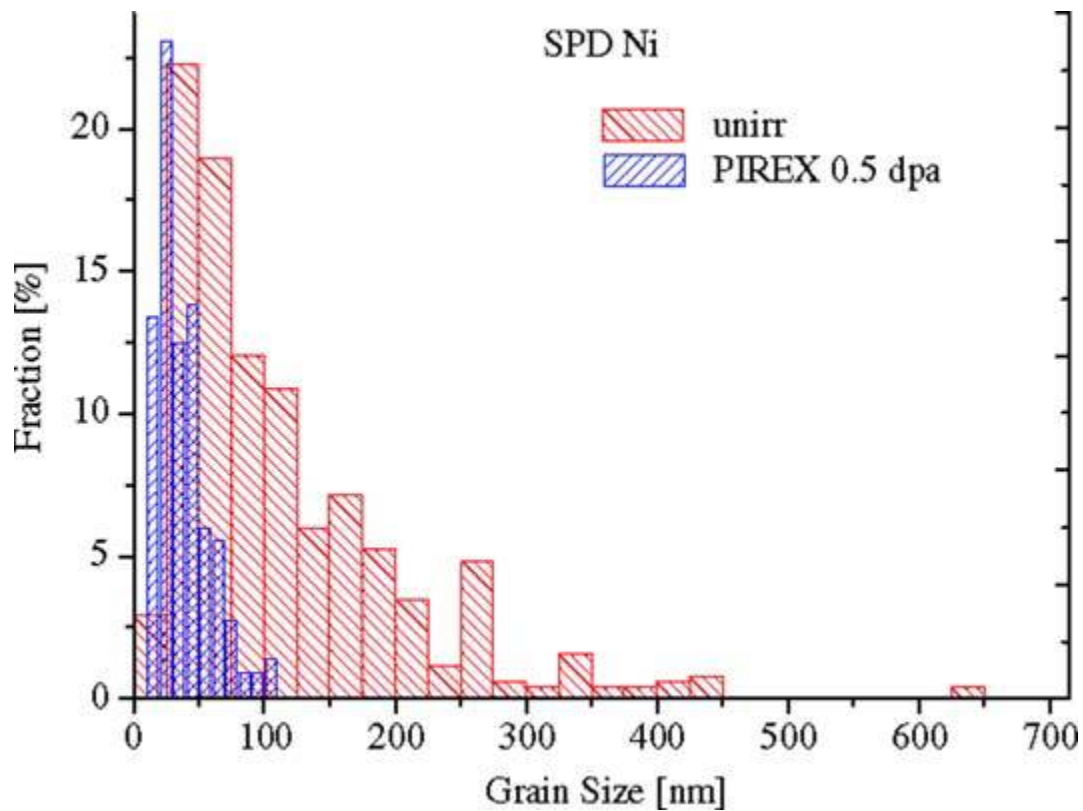


Figure 2.17: Grain size distributions for UFG Ni before (red) and after (blue) proton irradiation at room temperature [56].

2.4.4 Computer Simulations Studies

The combination of the experimental results (neutron and ion irradiation) along with predictive simulation models is a great tool to develop improved candidate materials for advanced reactors. Computer simulations allow us to investigate the irradiation interaction with matter at atomic scale. Modeling of radiation damage and displacement cascades in materials has been investigated utilizing different materials and crystal structures [73, 74]. The consequences of irradiation on NC and UFG materials were investigated using different

computer simulations. Through molecular dynamics (MD) simulations on nanostructured bcc molybdenum Millett et al. [75] demonstrated that grain boundary sinks have equal bias to both interstitials and vacancies. Samaras et al. [21] investigated the primary damage state after irradiation in both NC iron (bcc) and Ni (fcc) and they concluded that grain boundaries play a significant role in damage production during displacement cascade. Analogous study was performed on copper [76]. In order to understand the atomistic mechanism leading to irradiation tolerance behavior of the nano and ultra-fine grained materials, and to understand how defects interact with grain boundaries, Bai et al.[77] elucidated using different simulation methods (MD, temperature accelerated dynamics (TAD) and molecular statics) that grain boundaries upon irradiation are loaded with interstitials and eventually they become sources emitting interstitials via replacement process to annihilate vacancies in the bulk (Figure 2.18). Moreover, they found that interstitial-rich grain boundaries reduce vacancy diffusion barriers thus enhancing vacancies hopping and vacancies can migrate to the grain boundary more easily. Their “loading-unloading” model explains the previous experimental observations where the nano and ultra-fine grain materials may have better or worse radiation tolerance properties compared to their coarse grain counterparts, depending on the experimental conditions. Using MD simulation studies on copper, Bai et al.[77] also found that the number of surviving defects after irradiation depends on the distance between the initial PKA and the grain boundary, and the optimum distance where the number of defects is minimum was found to be 20 nm. Molecular dynamics computer simulations on irradiated NC Ni [68] showed that grain growth is observed if the irradiation damage spike volume reaches the grain boundary. However, if it doesn't then, irradiation induced grain

growth will not occur. Samaras et al. [78] also used molecular dynamics simulation to investigate the role of GBs in irradiated NC Ni. They showed that grain boundaries act as sinks for interstitials leaving the interior of the grain with only vacancy defects which may be removed by surrounding grain boundaries or triple junction regions.

As a conclusion from this literature review, knowledge about neutron irradiation on UFG grain materials is scarce and most of the previous studies were performed using charged particle irradiations which would not have the same effect as neutron irradiation because, for the same incident particle energy, the heavier particles are slower, stopped easier and deposit their entire energy over much shorter distances. Hence, innovative research that elucidates how UFG materials behave under neutron irradiation is required.

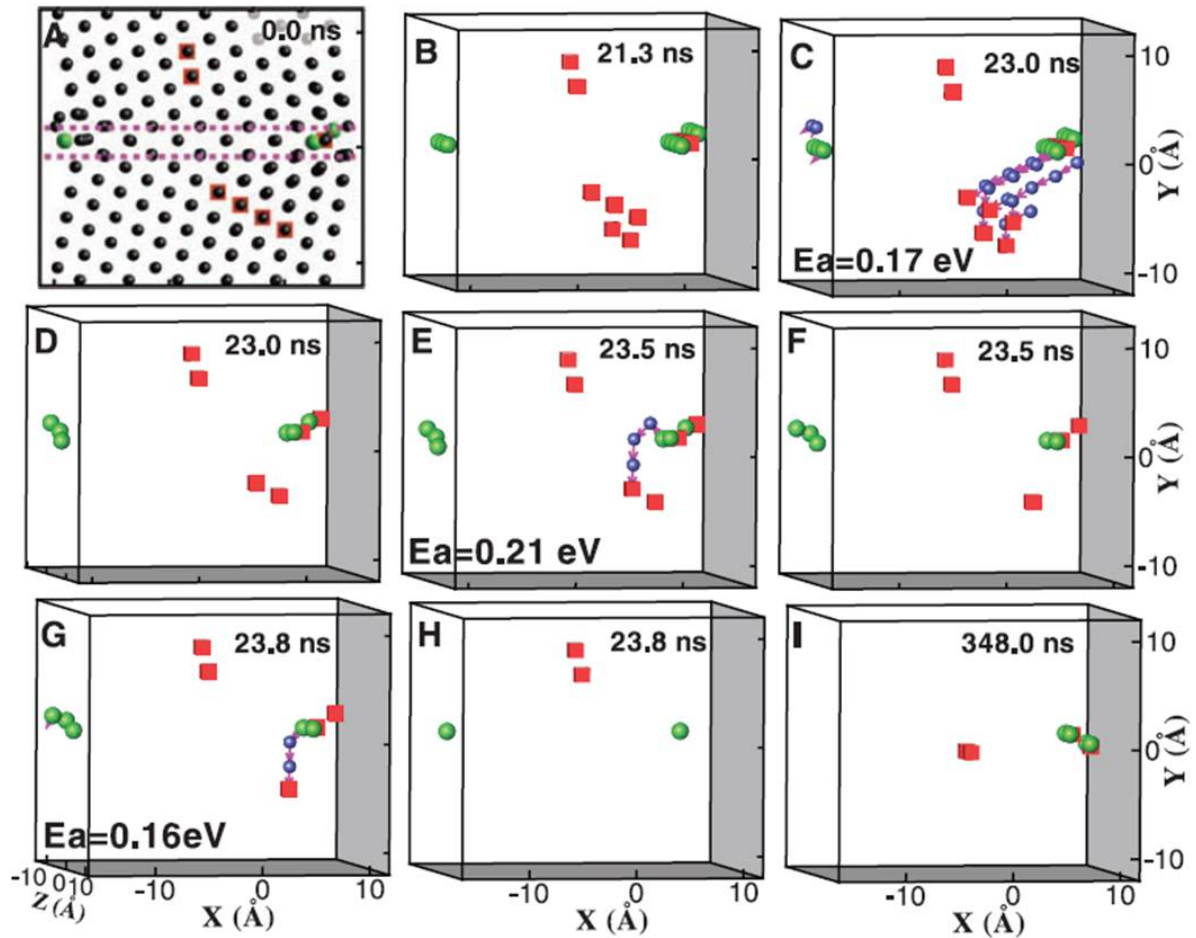


Figure 2.18: Temperature accelerated dynamics (TAD) simulation snapshots for the radiation damage cascade at 300 K in copper at different time intervals to follow the defect kinetics. It shows the damage self-healing near the grain boundary. Black small spheres represent the lattice atoms before irradiation, green spheres are interstitial atoms, red cubes are vacancies, blue spheres are atoms that moves more than 1 \AA during an event, purple vectors represent the direction of moving atoms and the two horizontal lines in all the snapshots represent the grain boundary [77].

Chapter 3. Materials and Irradiation Experiments

This chapter provides detailed information about the alloy used in this study, the processing procedure, sample preparation and irradiation experiment procedures and calculations. The irradiation experiments were performed in two reactors: 1) PULSTAR reactor at North Carolina State University (NCSU) at Raleigh, North Carolina and 2) Advanced Test Reactor (ATR) at Idaho National Laboratory (INL) at Idaho Falls, Idaho.

3.1 Materials and Sample Perpetration

Two material cases are considered in this study; ultra-fine grain low carbon steel (weight composition is shown in Table 3.1) processed through ECAP (section 2.3) and their conventional coarse grain counterparts that were produced by annealing the UFG material at 800 °C for one hour. UFG steel was made by ECAP using Bc route [45] with four passes where the material is rotated 90° in the same direction after each pass. This processing route ensures eventual restoration of the material cubic element (section 2.3). Pre-irradiated mean grain sizes for the UFG and CG steels are 0.35 ± 0.18 and 4.4 ± 1.8 μm , respectively (Figure 3.1).

The UFG steel was received from UFA State University in the form of parallelepiped bar with 1×1 cm^2 cross-sectional area. As mentioned earlier, the coarse grain counterparts were produced in the nuclear materials laboratory at NCSU by annealing the UFG samples to 800°C for 1 hour. The heat treatment was performed in flowing argon atmosphere to minimize oxidation of the sample surfaces. Micro-hardness values of the UFG steel samples

before and after annealing process (Figure 3.2) showed that Vickers micro-hardness of the as-prepared and the post-annealed samples treated up to 420°C have nearly the same value equal to 3.09 GPa. Annealing at higher temperatures leads to a gradual decrease in the micro-hardness values of the samples to attain 1.28 GPa for the sample that was annealed at 800°C and this annealed material is considered as conventional grain sized (CG) steel in this study. Following heat treatment, the thin oxide layer created during heat treatment was removed using 600 grit SiC grinding paper. Prior to irradiation, specimens with four different geometries were prepared from both UFG and CG steels. Figure 3.3 shows the geometries for the four types of specimens used in this study. Samples were cut from the bulk material and were prepared by grinding with a series of silicon carbide papers (600, 800 and 1200 grits) to optical flatness and then polished in colloidal silica resulting in deformation free surfaces. In order to minimize induced radioactivity, relatively small disc and coupon samples along with miniature tensile specimens were used in this study, and special tensile grips were designed for testing those miniature tensile samples (Figure 3.4).

Table 3.1: The chemical composition of the steel material (weight percent).

Elements	C	Si	Mn	Fe
Wt%	0.1	0.27	0.5	Balance

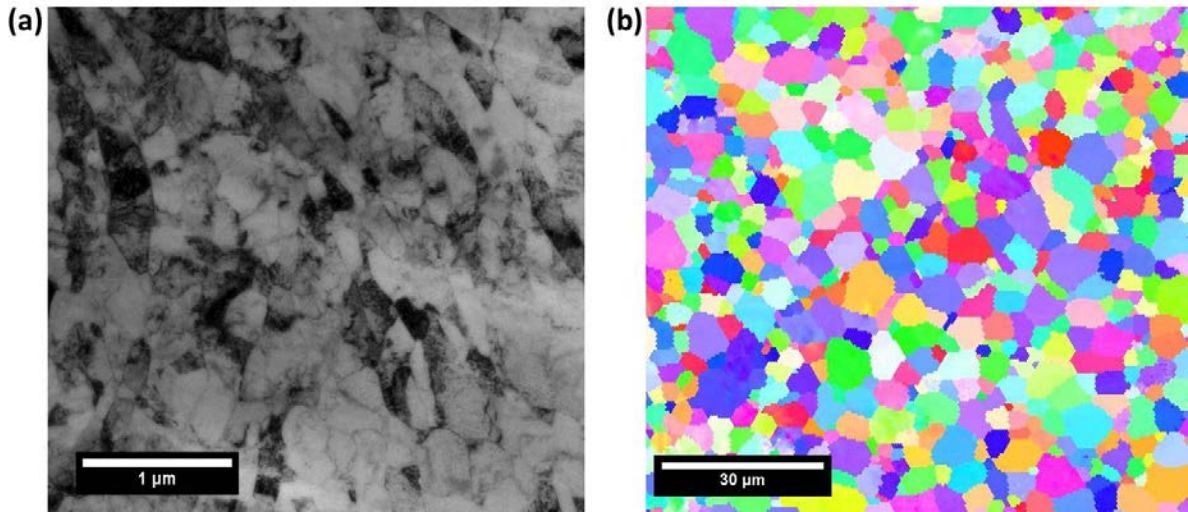


Figure 3.1: Transmission electron microscopy (TEM) micrograph showing the grain size distribution for UFG steel ($d= 0.35\pm 0.18 \mu\text{m}$) (a) and electron back scattered diffraction (EBSD) micrograph for CG Steel ($d= 4.4\pm 1.8 \mu\text{m}$) (b).

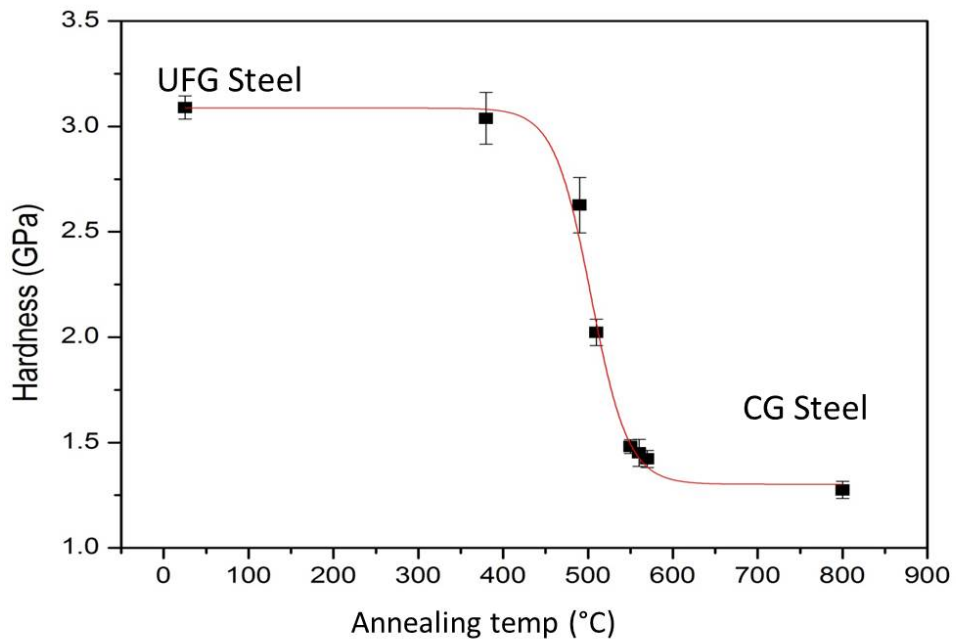
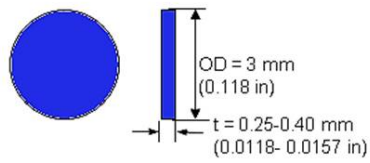
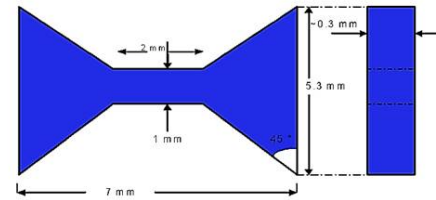


Figure 3.2: Vickers micro-hardness as a function of one hour annealing temperature.

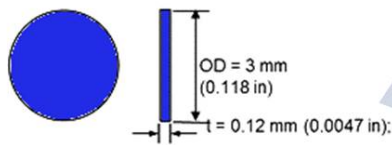
APT & EBSD:



Tensile test:



TEM:



Hardness test:

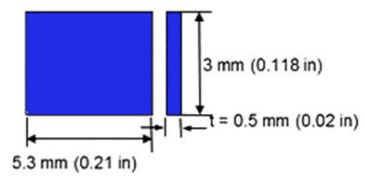


Figure 3.3: Pre irradiation sample geometries for both UFG and CG steels.

(a)



(b)



Figure 3.4: Photographs of low carbon steel mini tensile sample (a) and tensile test grips (b).

3.1.1 ECAP Imposed Strain Calculations

ECAP process imposes high shear strain to the work piece resulting in significant grain refinement. The strain introduced to the work piece due to the ECA pressing is calculated using Iwahashi model [47]. Iwahashi analysis assumes that the dies are fabricated as illustrated in Figure 3.5 and the specimen is lubricated so that frictional effects may be neglected.

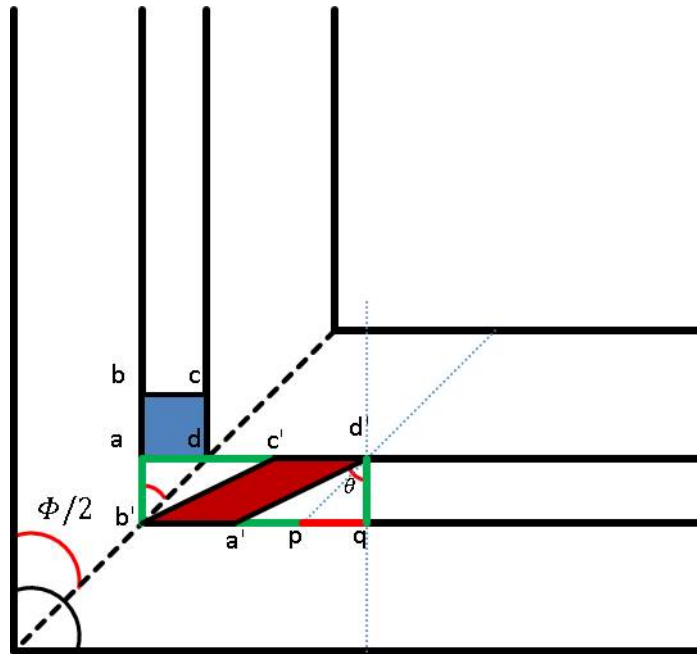


Figure 3.5: Schematic illustration of Iwahashi model to calculate the imposed strain through ECAP when the arc of curvature angle (Ψ) equals 0° .

Using the notations in Figure 3.5, a small element in the sample, initially square in cross-section with dimensions given by $abcd$, becomes deformed by shear on passage through the die into the configuration given by $a'b'c'd'$.

The shear strain (γ) is given by:

$$\gamma = \tan(\theta) = \frac{a'q}{d'q}. \quad (3.1)$$

But $d'q = ad$ because ECAP process does not change the cross-sectional dimensions of the deformed work piece. Due to geometry $b'a = c'd = a'p = pq$ and $a'p = pq = ad \cot\left(\frac{\Phi}{2}\right)$

$$\text{Then } a'q = 2 ad \cot\left(\frac{\Phi}{2}\right), \quad (3.2)$$

where Φ is the inner contact angle between the two intersecting channels. From Equ 3.1 and Equ 3.2 the shear strain is given by:

$$\gamma = 2 \cot\left(\frac{\Phi}{2}\right). \quad (3.3)$$

However, the equivalent Von Mises strain is given by:

$$\varepsilon_{eq} = \left(\frac{2 \left(\varepsilon_x^2 + \varepsilon_y^2 + \varepsilon_z^2 + \frac{\gamma_{xy}^2 + \gamma_{xz}^2 + \gamma_{yz}^2}{2} \right)}{3} \right)^{0.5}. \quad (3.4)$$

Knowing that the imposed strain has only shear component,

$$\varepsilon = \left(\frac{2 \cot\left(\frac{\Phi}{2}\right)}{\sqrt{3}} \right). \quad (3.5)$$

The imposed strain is proportional to the number of passes through the die (N_{pass}) and thus the total strain is given by,

$$\varepsilon = N_{pass} \left(\frac{2 \cot\left(\frac{\Phi}{2}\right)}{\sqrt{3}} \right). \quad (3.6)$$

However, it was shown [47] that if the arc of curvature angle (Ψ) (Figure 3.6 b) at the outer point of contact between channels of the die was not zero then the total imposed strain is given by:

$$\varepsilon_{eq} = \frac{2N_{pass}}{\sqrt{3}} \left(\cot\left(\frac{\Phi}{2} + \frac{\Psi}{2}\right) + \frac{\Psi}{2} \csc\left(\frac{\Phi}{2} + \frac{\Psi}{2}\right) \right). \quad (3.7)$$

In our study, the inner contact angle (Φ) and the arc of curvature (Ψ) at the outer point of contact between channels of the die were 90 and 0 deg, respectively. Using Equ.3.7 the imposed strain is calculated and found to be 4.618. As shown in Figure 3.6 the imposed strain is inversely proportional to both inner (Φ) and outer (Ψ) angles and the largest imposed strain can be attained when $\Phi=90^\circ$ and $\Psi=0^\circ$.

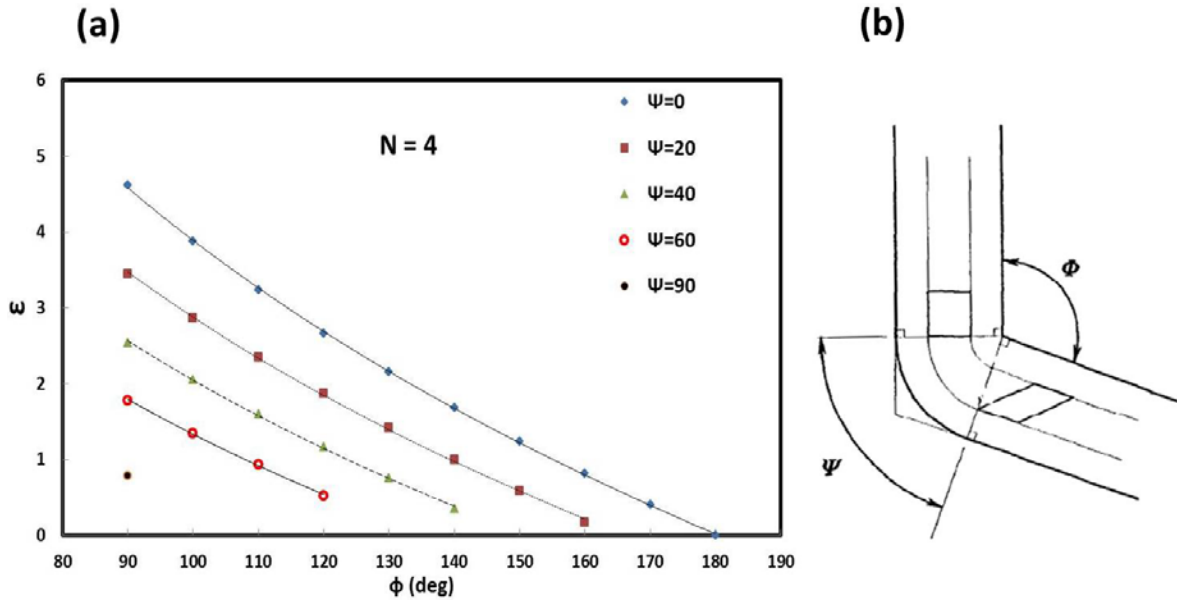


Figure 3.6: Imposed strain due to 4 passes through the die versus the inner contact angle (Φ) between channels of the die (a). Schematic of ECAP die showing the inner contact angle (Φ) and the arc of curvature angle (Ψ) at the outer point of contact between channels of the die (b).

3.2 Irradiation Experiments

Sample neutron irradiation was performed in two reactors at different irradiation doses. In this section, the irradiation procedures and calculations of irradiation parameters are presented for both PULSTAR and ATR experiments.

3.2.1 Fast Neutron Spectrum Determination for the dpa Calculations

In order to predict the effects of radiation on materials following neutron irradiation, a quantitative description of the irradiation damage produced by the incoming neutrons has to be considered. Displacements per atom (dpa) is a quantity that describes damage level in the

irradiated materials and can be defined as the average number of times each atom of a solid is displaced from its lattice site during radiation exposure [79]. As a standard parameter in determining radiation damage in materials, dpa measures the destruction energy deposited by neutrons in terms of the number of atoms that are permanently displaced from their lattice position to a stable interstitial position [80]. The dpa is used to correlate the damage in materials irradiated at different neutron environments. Different neutron irradiation facilities have different neutron spectra and can lead to different levels of radiation damage in materials. However, dpa quantity can account for these spectral differences and fit the data in one curve so that the irradiation effects on materials irradiated at different environments can be compared. Figure 3.7 shows the relationship between the irradiation dose and the irradiation effect (irradiation hardening) in 316 stainless steel alloy irradiated at three different neutron energy flux spectra. It can be shown that unlike fluence ($\Phi \times t_{irr}$), dpa can properly relate the results from the three different facilities and hence, the irradiation effects data from the different facilities can be compared easily. The dpa quantity can be calculated from the following equation [19]:

$$dpa = \frac{R_{dis} \cdot t}{N}, \quad (3.8)$$

where R_{dis} is the number of displacements per unit volume per unit time (displacement rate), N is the atomic number density and t is the irradiation time. The displacement rate can be evaluated as,

$$R_{dis} = N \int_{E_{min}}^{E_{max}} \phi(E_i) \sigma_d(E_i) dE_i, \quad (3.9)$$

where $\phi(E_i)$ is the energy dependent neutron flux, $\sigma_d(E_i)$ is the energy dependent displacement cross-section and E_{\max} and E_{\min} are the maximum and minimum energy of the incident neutrons.

As shown in Equ 3.9, unless the neutron flux spectrum at the irradiation position in the reactor is well defined, the dpa measurement will not be accurate, and the objective of predicting the change in the material properties after irradiation based on the dpa measurement will not be precise. Thus, the rest of this section illustrates the technique and the measurements that were conducted to map the high energy flux at the material irradiation position in the PULSTAR reactor at North Carolina State University.

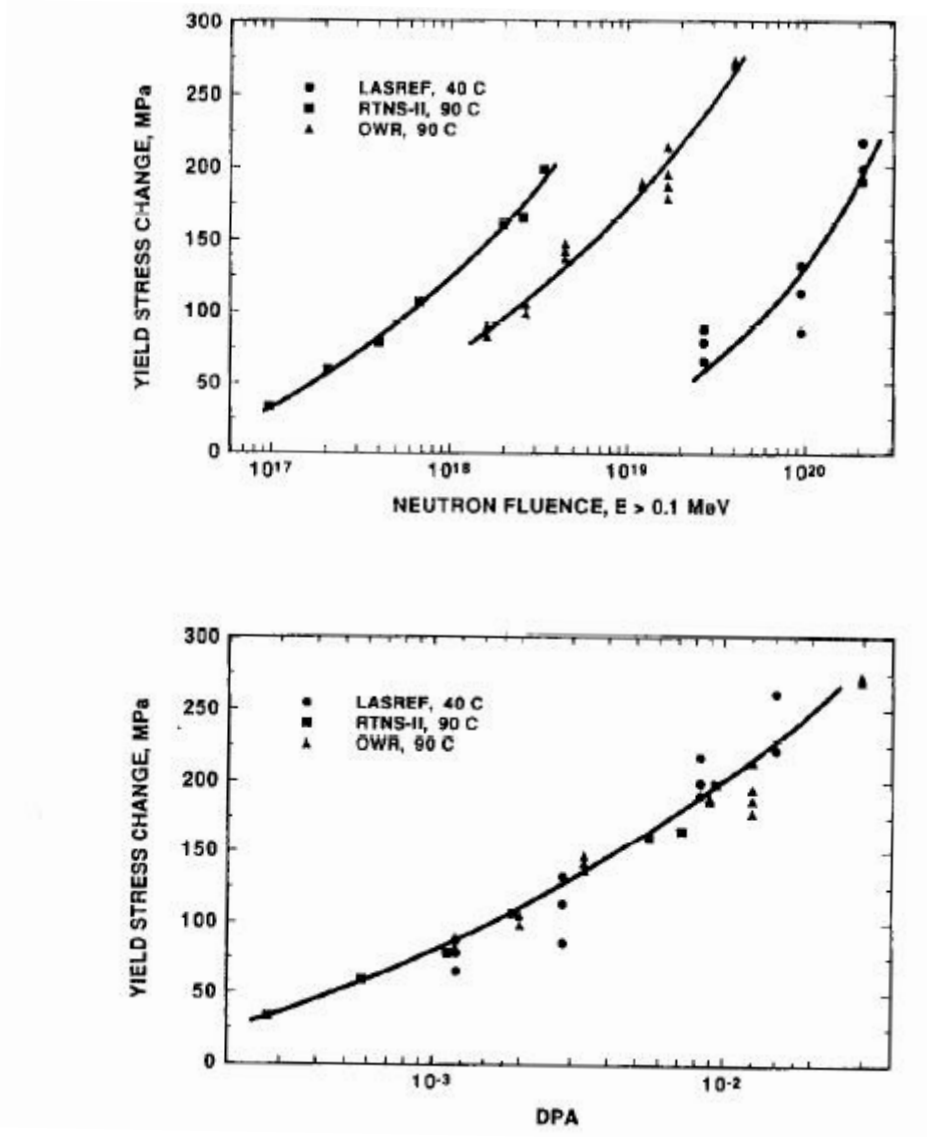


Figure 3.7: Comparison of yield stress change in 316 steel following irradiation in three different facilities [81].

3.2.1.1 Foil Activation Technique

Several measuring techniques are used to determine the fast neutron flux spectrum. One of the most common techniques for fission reactors is the activation of multiple threshold detectors [81]. It involves the irradiation of target materials (foils) with a flux of neutrons for a pre-determined period. The foil is removed after a measured period of time and the induced activity is determined [82]. The neutrons interact with the nucleus of the target material and produce new radioactive isotopes. These radioactive isotopes emit a unique combination of gamma rays that can be detected and then used to measure the neutron spectrum inside the reactor at the position of the irradiation experiment. Neutron interactions with material nucleus can have many different reaction types such as: (n,γ) , (n,α) , (n,p) , $(n,2n)$, etc. Each of these interactions has a probability of occurring defined by its cross-section. Some interactions such as (n,γ) reactions can occur at any incident neutron energy, while others require neutrons above a minimum (threshold) energy for the reaction to occur. Different materials undergo different neutron reactions that have different threshold energies. The foils have to meet some conditions in order to be suitable for this activation technique [82, 83]:

- The different reaction cross-sections should cover the entire neutron energy of the flux spectrum of interest.
- In order to obtain higher saturation activity, foil materials is preferred to have high cross-section for the activation reaction of interest.

- Foils need to be highly pure to avoid any interference reactions and insure that the calculated activity is produced only from the reaction of interest.
- The reaction cross-sections, gamma ray abundances and the half-life of the produced radioactive nuclide should be accurately known.

The decay of the produced radioisotope normally involves emission of either gamma rays or beta particles. Gamma detection is preferred over the beta because with gamma detection it's easier to discriminate the interfering activities and background. Moreover, gamma detection minimizes the effect of self-absorption because of its penetration nature [84]. However, the specific activity induced in the detector (irradiated foil) can be measured using the gamma ray spectroscopy of the irradiated foil material. Gamma rays are emitted by excited nuclei in their transition to lower nuclear levels. Because nuclear states have very well defined energies, the energies of gamma rays emitted in state-to-state transitions are also specific to a particular nuclide [85]. The gamma rays emitted from the radioactive foils are detected and used to determine the irradiated foil activity. As the foil is irradiated, new radioactive nuclear species will be produced but at the same time they also undergo radioactive decay. The production rate is given by [86],

$$\left. \begin{aligned} R &= N^* \int_{E_{\min}}^{E_{\max}} \phi(E) \sigma_{act}(E) dE \\ N^* &= \frac{\delta m A_v}{A} \end{aligned} \right\}, \quad (3.10)$$

where R is the activation reaction rate per second, N* is the number of the target nuclei in the foil at time of irradiation, m is the sample mass, δ is the isotopic abundance of the target nuclide, A_v is Avogadro's number and A is the atomic mass number of the sample, $\phi(E)$ is

the neutron flux and $\sigma_{act}(E)$ is the activation reaction cross-section. Both $\phi(E)$ and $\sigma_{act}(E)$ are functions of the incident neutron energy.

The rate of decay is given by,

$$\left. \begin{aligned} \text{Decay rate} &= N_{radio} \cdot \lambda \\ \lambda &= \frac{\ln(2)}{T_{half}} \end{aligned} \right\}, \quad (3.11)$$

where N_{radio} is the total number of radioactive nuclei, λ is the decay constant, T_{half} is the time needed for half of the radioactive nuclides to decay. Then, the rate of change in the total number of radioactive nuclei is given by,

$$\frac{dN_{radio}}{dt} = \text{Production rate} - \text{Decay rate} = R - N_{radio} \cdot \lambda, \quad (3.12)$$

Assuming that the flux does not change during the irradiation experiment and neglecting the decrease in the number of the target nuclei during irradiation (N^* is constant), then the differential equation (equ 3.12) can be solved knowing that the total number of radioactive nuclei before irradiation is zero $\{N_{radio}(0)=0\}$,

$$N_{radio}(t) = \frac{R}{\lambda}(1 - e^{-\lambda t}). \quad (3.13)$$

The activity of the foil is given by,

$$A(t) = N_{radio}(t) \cdot \lambda = R(1 - e^{-\lambda t}), \quad (3.14)$$

where t is the irradiation time. As shown in equ 3.14, the activity of the irradiated foil is proportional to the neutron flux. Let the irradiation time be t_{irr} , the activity of the foil at the end of irradiation is,

$$A_0 = R(1 - e^{-\lambda t_{irr}}). \quad (3.15)$$

Note that if t_{irr} was very long (many times longer than the half-life of the radioisotope), the activity reach a saturation value ($A_{sat} = R$). After irradiation, the foil activity starts decaying. Considering the end of irradiation as time $t=0$, then at time t after irradiation stops the activity is given by,

$$A(t) = A_0(e^{-\lambda t}). \quad (3.16)$$

During the decay time, the foil will be moved to an appropriate counter and if the sample is counted between t_1 and t_2 , the number of disintegration in that period is,

$$\frac{C-B}{\gamma\epsilon} = \int_{t_1}^{t_2} A(t) dt = \int_{t_1}^{t_2} A_0(e^{-\lambda t}) dt = \int_{t_1}^{t_2} R(1-e^{-\lambda t_{irr}})(e^{-\lambda t}) dt, \quad (3.17)$$

where C is the number of counts in the time interval between t_1 and t_2 ($t_{count} = t_2 - t_1$), B is the number of background counts during counting interval time (t_{count}), γ is the gamma ray abundance (yield) and ϵ is the detector efficiency. Note that t_1 is the elapsed time from the end of the irradiation period to the start of the counting period (t_{decay}). Then equ 3.17 becomes:

$$\frac{C-B}{\gamma\epsilon} = \frac{R(1-e^{-\lambda t_{irr}})(1-e^{-\lambda t_{count}})(e^{-\lambda t_{decay}})}{\lambda}. \quad (3.18)$$

Substituting equ 3.10 in equ 3.18 and rearranging the equation, the reaction rate per second and per nucleus of interest for each irradiated foil comes out to be,

$$R^* = \int_{E_{min}}^{E_{max}} \phi(E)\sigma_{act}(E)dE = \frac{\lambda (C-B)}{\epsilon N^* \gamma (1-e^{-\lambda t_{irr}})(1-e^{-\lambda t_{counting}})(e^{-\lambda t_{decay}})}. \quad (3.19)$$

The fast neutron flux spectrum at the irradiation location in the PULSTAR reactor was determined using the neutron activation of multiple threshold detectors. Foils of 8

different materials for which the activation reactions cover a range of threshold energies were irradiated for a pre-determined period. Table 3.2 shows the experimental foils and their threshold energies for different reactions. The cross-sections for the reactions of interest are shown in Figure 3.8 (cross-sectional data is taken from the evaluated nuclear data file (ENDF) [87]). Since materials' radiation damage assessment is the purpose of the material irradiation facility at the PULSTAR reactor and the neutrons of interest are fast neutrons with energies greater than 0.1 MeV, all reactions were chosen with cross-section threshold energy that covers the energies of interest. After irradiation, the foils were cooled for some time so that they can be handled safely. One of the constraints was that if the sample cooled for a long time, the radioisotope of interest may totally decay (Ex: ^{27}Mg isotope produced from the reaction $^{27}\text{Al} (n,p)^{27}\text{Mg}$ has a 9.46 min half-life). Therefore, the irradiation and decay times for each foil were chosen so that the sample will have a countable induced activity from the reaction of interest and a low radioactivity dose so it can be handled safely. Induced γ -ray activity of the irradiated foils was measured using a high purity germanium (HPGe) detector for a period depending on the decay half-lives and the foil exposure time. Detector efficiency was determined using a calibrated ^{152}Eu (Europium) point source for which the rate of disintegration is known accurately. ^{152}Eu standard source was used because it has a long half-life (15.537 year) and emits many different gamma rays that cover wide range of the gamma energies as shown in Table 3.3. The detection efficiency for each gamma ray that is emitted from the standard ^{152}Eu source was measured at the same counting conditions that were used later to measure the activities of the radionuclides,

$$\varepsilon_{\gamma} = \frac{\text{number of pulses recorded}}{\text{number of radiation quanta emitted by the source}} = \frac{C}{\gamma A_0 e^{-\lambda t}}, \quad (3.20)$$

where γ is the gamma ray abundance (yield), A_0 is the initial activity of the source at time of standardization, λ is the decay constant and t is the elapsed (decay) time since standardization. Detector efficiencies for the different γ energies were fitted to a non-linear power function that describes the detector efficiency over the entire energy range, so that the detector efficiency can be determined for energies other than those of the standard source (Figure 3.9). All the measurements were done with the same source-detector geometry to maintain the same solid angle for the source (radioactive isotope) with respect to the detector. The neutron fluence and its energy distribution are then derived from the measurements of the neutron induced γ -ray activity in the foils by means of a deconvolution algorithm; STAYSL code [88] was used to solve the dosimetry unfolding problem by the method of least squares to find the flux spectrum. The code uses an iteration method with an initial trial spectrum which is modified until the calculated γ -ray activities are in agreement with the measured ones within a user preset standard deviation [85]. The STAYSL code is available from the Radiation Shielding Information Center (RSIC) at Oak Ridge National Laboratory.

Neutron damage in the irradiated samples was quantified in terms of dpa. Using the pre-calculated neutron flux spectrum at the irradiation position as an input into SPECTER code [89]. SPECTER code calculates the number of displacements per atom in addition to hydrogen and helium gas generation for an input neutron flux spectrum based on a differential cross section library. The results showed that the steel samples were irradiated to a neutron fluence of 2.2×10^{22} neutrons/m² ($E > 0.1$ MeV), corresponding to a dose of

1.15×10^{-3} dpa. Accurate calculation of the dpa using the fast neutron flux spectrum is used to quantify the damage in the irradiated materials and compare the damage for different doses obtained at other irradiation facilities.

Table 3.2: Characteristics of threshold reactions [90–92]

Material	Reactions of interest	Threshold Energy (MeV)	Radio-isotope half life	Gamma Energy (KeV)	Gamma abundance (yield)
Ni	$58\text{Ni}(n,2n)57\text{Ni}$	13	35.6 hours	1377	81.70%
	$58\text{Ni}(n,p)58\text{Co}$	1	70.88 days	810	99%
Al	$27\text{Al}(n,\alpha)24\text{Na}$	4.5	14.96 hours	1368	100%
	$27\text{Al}(n,p)27\text{Mg}$	2.25	9.46 minutes	843	100%
Mg	$24\text{Mg}(n,p)24\text{Na}$	5	14.96 hours	1368	100%
In	$115\text{In}(n,n)115\text{mIn}$	0.34	4.486 hours	335	45.83%
Co	$59\text{Co}(n,\alpha)56\text{Mn}$	4	2.58 hours	846.7	98.90%
Ti	$47\text{Ti}(n,p)47\text{Sc}$	0.1	80.38 hours	159.37	68.30%
Cu	$63\text{Cu}(n,\alpha)60\text{Co}$	2	5.27years	1173	100%
Au	$197\text{Au}(n,2n)196\text{Au}$	8.25	6.18days	355	87%

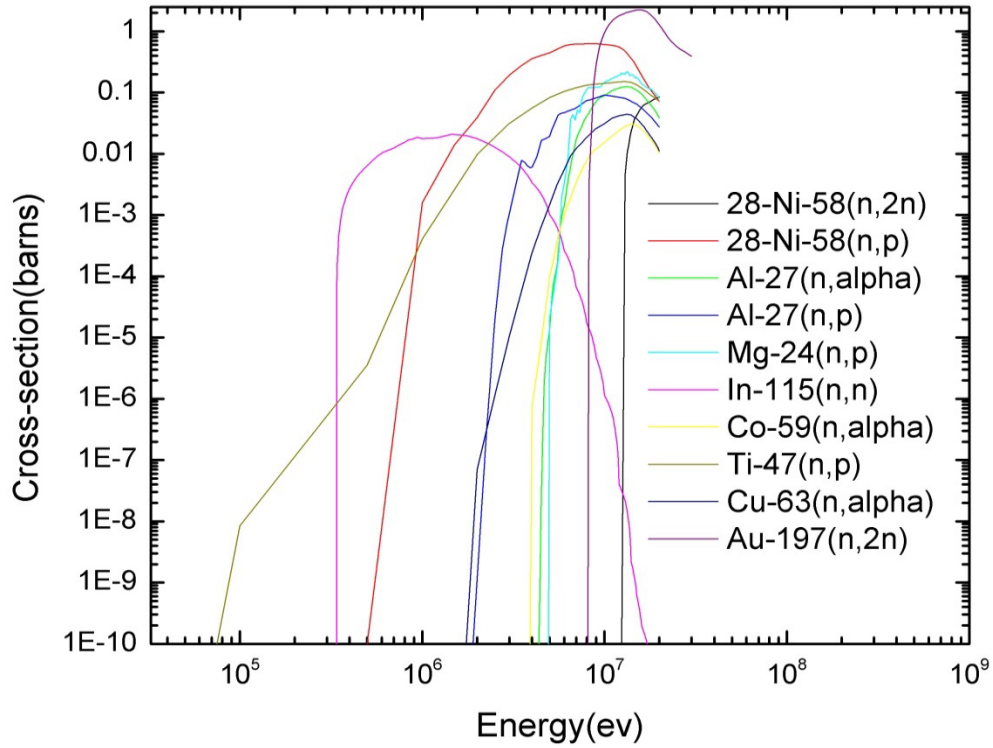


Figure 3.8: Cross sections for threshold reactions of interest [87].

Table 3.3: Decay properties of the ^{152}Eu standard source [91].

Nuclide	Half-Life	Gamma-Ray Energy (keV)	Gamma-Ray Probability per Decay (%)
^{152}Eu	15.537y	1408.006	21.005
		1112.074	13.644
		1085.869	10.207
		964.079	14.605
		867.378	4.245
		778.9040	12.942
		443.965	2.821
		411.1163	2.234
		344.2785	26.5
		244.6975	7.583
		121.7817	28.58

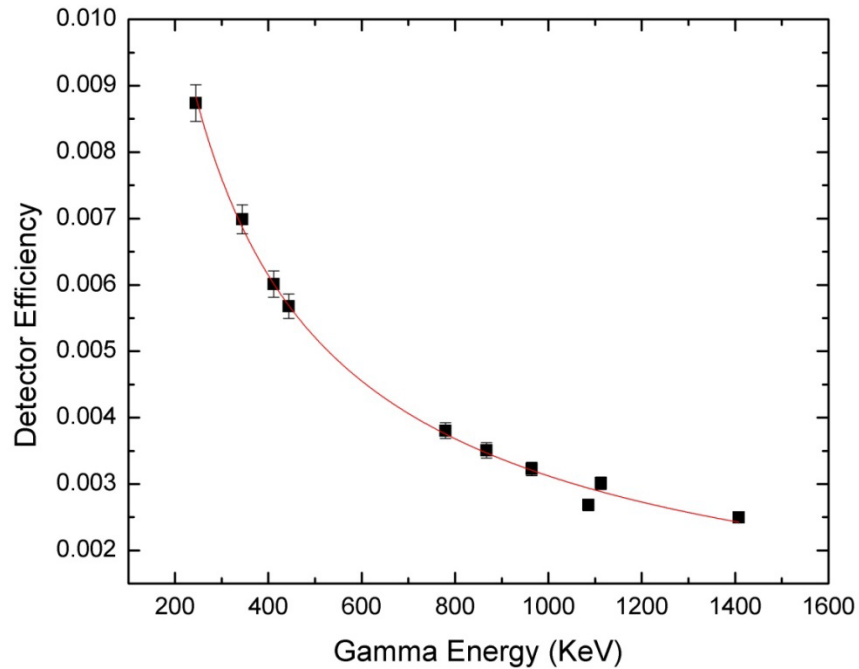


Figure 3.9: Calculated HPGe detector efficiency vs. gamma energies.

3.2.2 PULSTAR Irradiation Experiment

The PULSTAR reactor is a 1-MWth research open pool reactor located at North Carolina State University (NCSU) campus. The reactor is fueled with low enriched (4% of U^{235}) pin-type fuel consisting of uranium dioxide pellets (UO_2) in Zircaloy cladding [93]. PULSTAR reactor uses the light water as moderator, coolant and partial shielding. The inherent structure of the PULSTAR core and reactivity considerations did not permit irradiation in the core and thus a vertical irradiation tube at core boundary was used as irradiation site. The PULSTAR reactor has four ex-core irradiation ports and the nuclear

material irradiation was conducted in the west rotation exposure port (WREP) shown in Figure 3.10.

The samples were sealed in quartz tubes and loaded in an aluminum jig that has holes with the same diameter as the quartz tubes (Figure 3.11). The jig was inserted in the bottom of a cadmium lined stringer to screen out the low-energy neutrons and thus reducing the production of long lived radioactive transmutations which will increase the time for the activity to decay before handling the samples safely. The radiation stringer was left in the reactor for about 2.5 months with an effective full power time of 7.2×10^5 s (200 hours). After irradiation, all the samples along with the aluminum jig became highly radioactive and thus were left in the reactor pool for more than nine months for the activity to decay so that the samples can be handled without any remote handling facility. MCNP calculations showed that heat generation rate during irradiation due to the (n, γ) reaction is insufficient to increase the samples temperature above the reactor water temperature. Thus, the maximum ambient temperature of steel samples over the 200 hrs of irradiation was about 55°C same as the reactor operating temperature.

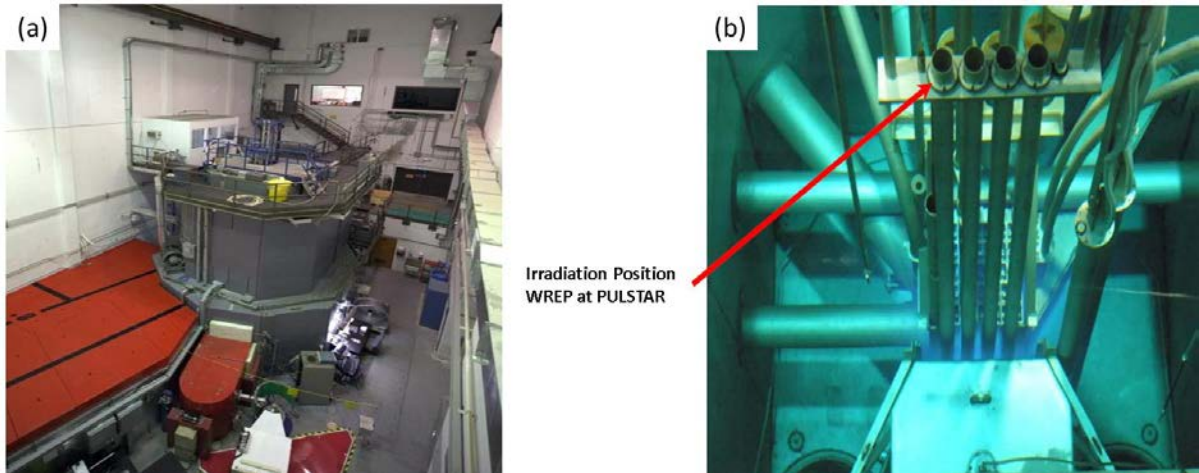


Figure 3.10: PULSTAR reactor (a) and the irradiation position in the PULSTAR reactor core (b).



Figure 3.11: Sample irradiation loading. Sealed quartz tube (a), Aluminum irradiation jig (b) and Aluminum irradiation stringer (c) lined with Cadmium layer (d).

3.2.2.1 PULSTAR Experimental Characterization Methods

After waiting for the samples to cool down to low doses, they were transferred to the Nuclear Materials Laboratory (NML) at NCSU where the microstructure and mechanical properties were evaluated. The effect of low dose neutron irradiation on the microstructural properties of UFG and CG steels were investigated using TEM, optical microscopy and X-ray diffraction analysis. TEM was conducted using JEOL 2000FX. X-ray diffraction was performed using a Rigku SmartLab X-ray diffractometer, the radiation source was Cu K α ($\lambda=0.154056$ nm) and the scan range was 40-120 degrees. The microstructures of the CG low carbon steel were investigated by optical microscopy. Both unirradiated and irradiated CG samples were ground with a series of silicon carbide papers to optical flatness and then polished in colloidal silica to mirror finish. The samples were then etched using 2 ml HNO₃ and 100 ml Alcohol, and their microstructure was explored using Buehler ViewMet optical microscope. Irradiation induced hardening in the steel samples was quantified using both microhardness and tensile tests. Vickers hardness testing was performed on unirradiated and post-irradiated specimens using Buehler Micromet 5103 Instrument. Indentations were performed with a Vickers indenter tip using 0.5 kg load. Ten indents were taken on each specimen to obtain good statistics. Room temperature tensile tests were conducted to evaluate the hardening and delineate the embrittlement susceptibility of the neutron irradiated specimens. Unirradiated and post-irradiated samples were strained to failure at a strain-rate of 10^{-3}s^{-1} using Instron 3342 tensile machine, and three tests were performed for each condition.

3.2.3 ATR Irradiation Experiment

The Advanced Test Reactor (ATR) is located at Idaho National Laboratory (INL), Idaho. ATR has been operating since 1967 and is currently one of only three remaining operating reactors at the INL site[94]. It is considered one of the world's leading test reactors for providing the capability for studying the effects of intense neutron and gamma radiation on reactor materials and nuclear fuels. It can operate at a maximum power of 250 MW and has a "Four Leaf Clover" core design (Figure 3.12b) that allows for a variety of testing locations at different power levels [94].

The irradiation experiment was carried out in the E-7 position of the East Flux Trap (Figure 3.12b) in the ATR. The materials were irradiated for two irradiation cycles, the first cycle was 43.7 days and second one was 51.7 day, so the total irradiation time was 95.4 days. The materials were irradiated to a neutron fluence of 1.78×10^{25} neutrons/m² ($E > 0.1$ MeV), corresponding to a dose of 1.37 dpa. Figure 3.12(a) is a schematic of the irradiation test assembly consisting of the experiment basket and capsule assemblies. Each capsule contains a test train assembly consisting of aluminum blocks that hold the samples (Figure 3.13). The samples (UFG and CG steel) were loaded in sample holders (Figure 3.13) and a thin aluminum disc was tack-welded to the open end of each holder to hold the samples inside it. Each group of sample holders was strung together using aluminum rods (Figure 3.13d) and was assembled into a sample train which was designed to hold the samples for easier removal following irradiation and also to help keeping the samples at the desired irradiation temperature. Lastly, the sample trains were sealed in a stainless steel containment capsule

that is essentially a sealed pressure vessel designed to isolate the test specimens. The integrity of the capsules was ensured using helium leak testing, dye penetrant testing and visual inspection. The experimental basket of the test assembly (Figure 3.12a) is an aluminum tube designed to interface the capsule assembly with the ATR. The experiment thermal analysis was performed using a detailed finite element model of the experiment using ABAQUS code [95]. MCNP code [96] was used to calculate the heat generation rate for each part of the experiment which was then used as an input to the finite element model (Figure 3.14). The specimen temperature during irradiation was found to vary between 70 °C to 100 °C depending on the sample position in the irradiation capsule. The low irradiation temperature is mainly due to the small helium gas gaps between specimens and holder, and between holder and capsule.

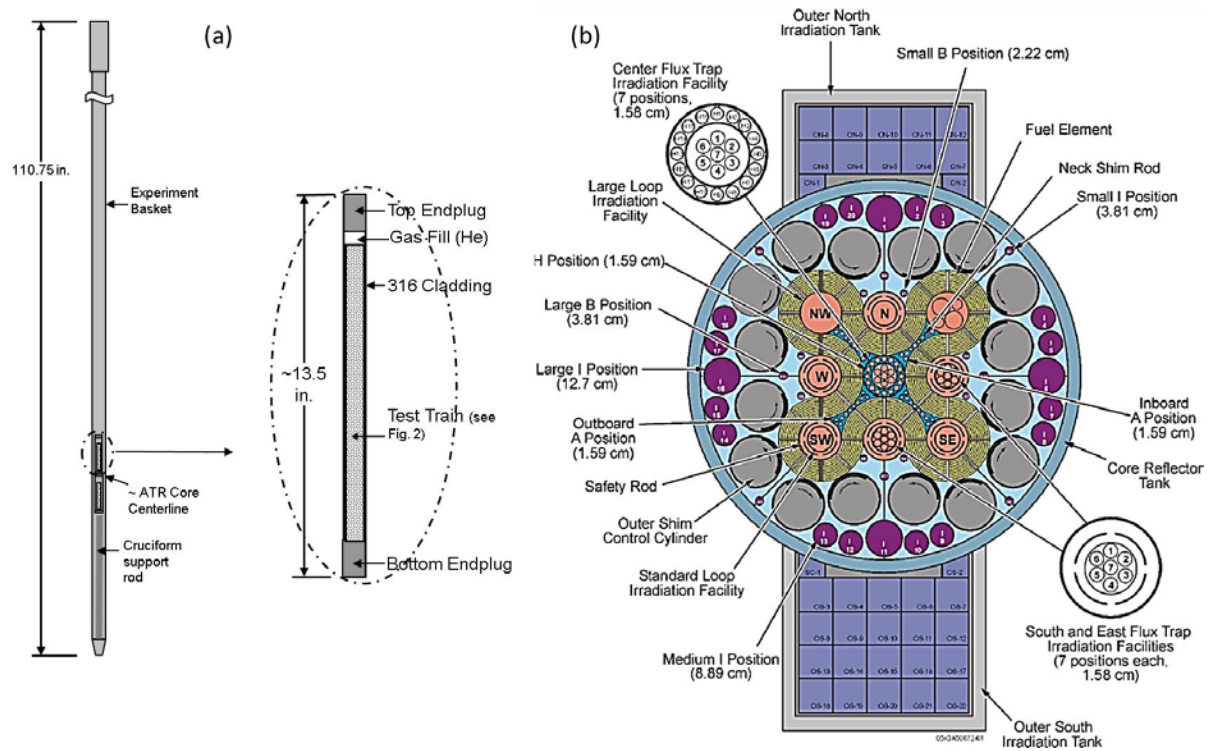


Figure 3.12: Experiment irradiation test assembly for ATR east flux trap position (a) and radial cross section view of the ATR reactor core, E-7 irradiation test position (b).

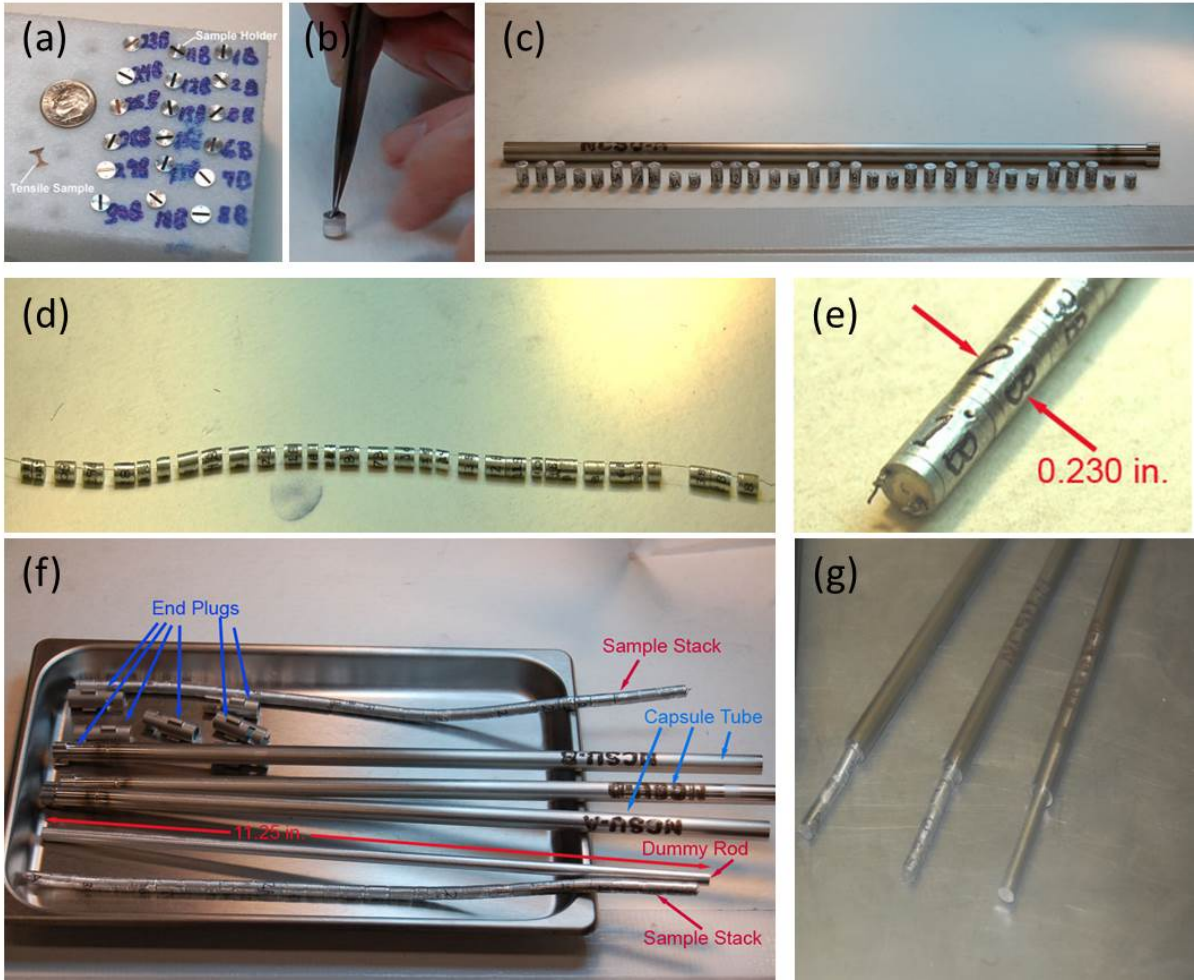


Figure 3.13: Sample holder, sample train and irradiation capsule loading and design.

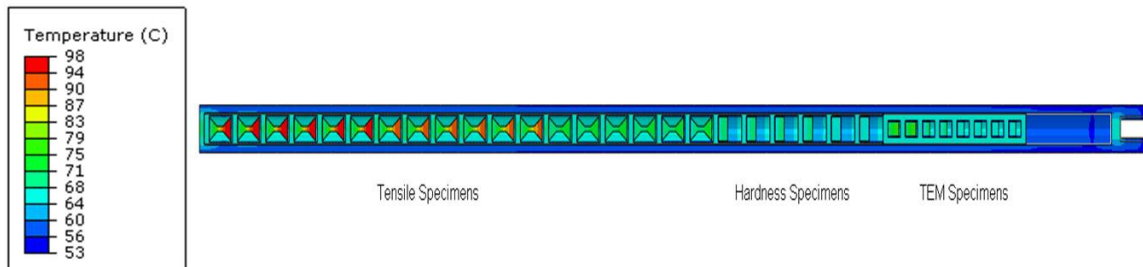


Figure 3.14: Sample irradiation temperature calculated by a detailed finite element model of the experiment using ABAQUS code.

3.2.3.1 ATR Experimental Characterization Methods

The grain sizes for both steel cases (UFG and CG) were investigated using different methods. Electron backscattered diffraction (EBSD) was used to demonstrate the grain size distribution in CG steel and transmission electron microscopy (TEM) was used to obtain mean values of the grain size in UFG steel. The EBSD measurements were conducted on a Quanta 3D FEG scanning electron microscope. Crystallographic orientation mappings were taken using a step size of 0.5 μm in an area of 100 μm x 100 μm . The colors in the EBSD pole inverse images represent the different orientations, e.g., red, green and blue indicate the (0 0 1), (1 0 1) and (1 1 1) planes respectively.

The defect structure and materials microstructures were investigated using two TEM microscopes; using a Tecnai 300KV TF30 FEG-STEM at the Center for Advance Energy Studies (CAES) at Idaho where the samples were prepared using FIB technique (FIB was carried out using a Quanta 3D field emission gun (FEG) instrument) and using JEOL 2010 TEM at the Electron Microscopy Laboratory (EML) at Idaho National Laboratory (INL) where samples were prepared by Jet-polishing technique. Each TEM disk was further thinned mechanically to a final thickness of 100 to 150 μm using 1200 grit SiC paper. Then, a perforation was made in the center of the disk using a South Bay Model 550 electrochemical single jet polisher. The samples were electropolished using a mixture of 5 vol.% perchloric acid and 95 vol.% methanol. The polishing solution was cooled to -45°C using liquid nitrogen or dry-ice cooled methanol bath. The voltage applied to the sample was adjusted to around 80V and the jet polishing current was around 70mA. X-ray diffraction (XRD) of the UFG and CG steels before and after irradiation was performed using PANalytical

diffractometer with $\text{CuK}\alpha$ radiation (wavelength 0.15406 nm). All the diffraction profiles were obtained by varying 2θ from 40° – 120° with a scan step of 0.026° and the samples were rotated at 4 sec/rev.

Atom probe tomography (APT) has the ability to provide valuable microstructural information by both 3D imaging and chemical composition measurements at the atomic scale. The atom probe technique produces three dimensional positions of atoms which are evaporated from a sharply pointed tip by inducing a very high electric field at the tip surface [97]. APT also provides a distinct vision on solute behavior and neutron-induced clustering in the material [98]. The microstructure of the neutron irradiated low carbon steel for both grain sizes (CG and UFG) was also characterized via local electrode atom probe (LEAP) using CAMECA Instruments LEAP 4000X HR. The analyses were acquired using voltage pulsing (20% pulse fraction) at a specimen temperature of 50 K. LEAP tomographic data were analyzed employing IVAS v3.6.6 (CAMECA Instrument). A focused ion beam (FIB) was used to prepare specimens for atom probe tomography. FIB was carried out using a Quanta 3D field emission gun (FEG) instrument with a Ga ion source. The LEAP specimens were needle shaped with an apex radius of ~ 30 nm using FIB (Figure 3.16). Due to the irradiation embrittlement some atom probe specimens fractured under the high stresses applied during the test. Thus, six tips were prepared from each sample and 3 tips from each sample were analyzed to maintain good statistics.

Due to the neutron irradiation damage, the mechanical properties will be altered and those properties were conveniently determined at the micro and nano scales. Both nano and micro hardness tests were conducted to examine the material ability against deformation at

different scales. The nano hardness of the steel samples (both UFG and CG) before and after irradiation was characterized using a Hysitron TI-950 nano indenter equipped with a Berkovich diamond tip having a face angle of 142.3° . Several indents on standard fused silica sample were performed before each run to calibrate the indenter shape. Twelve indentations were created on each sample (un-irradiated UFG, irradiated UFG, un-irradiated CG and irradiated CG steel samples) using load range 45 mN – 210 mN with indents separated by $60\ \mu\text{m}$ from each other. Ten measurements were repeated at each load to obtain good statistics. Indentations were scanned and imaged using JEOL JSM-6610 LV scanning electron microscopy (SEM). Micro hardness measurements were carried out on the steel samples pre and post irradiation using Leco LM247AT Vickers micro hardness tester at a load of 500 g-f ($\sim 5\text{N}$). Twelve indents were made on each sample with a dwell time of 13 seconds and their average value is reported. The indents were $300\ \mu\text{m}$ apart to avoid any influence from the previous indents on the hardness value.

Fitting the unloading part of the nano indentation load-displacement curves to a power equation was used to evaluate the nano hardness based on Oliver and Pharr model [99]. The Oliver and Pharr method is considered to be the most common one to analyze the load-displacement curves in which the unloading data are described by a simple power law relation,

$$P = A(h - h_f)^m, \quad (3.21)$$

where P is the indentation load, A and m are fitting parameters, h_f is the final displacement (depth) which is also found by a least squares fitting procedure and h is the displacement at

any time during the test. The derivative of the power law relation (with respect to h) is evaluated at the maximum load to calculate the contact stiffness S,

$$S = \frac{dP}{dh}(h = h_{\max}) = mA(h - h_f)^{m-1}. \quad (3.22)$$

The contact depth which corresponds to the vertical distance along which contact is made between the indenter and the specimen is given by,

$$h_c = h_{\max} - \varepsilon \frac{P_{\max}}{S}, \quad (3.23)$$

where P_{\max} is the peak load, h_{\max} is the indentation depth at maximum load and ε is an indenter geometry constant. In this study $\varepsilon=0.75$ (paraboloid geometry). Contact area is determined using both the depth of contact (h_c) and the area function of the indenter that relates the cross-sectional area of the indenter to the distance from its tip ($A_c = f(h_c)$).

Finally the hardness is measured by dividing the peak indentation load over the contact area,

$$H = \frac{P_{\max}}{A_c}. \quad (3.24)$$

In order to delineate irradiation induced embrittlement and hardening, tensile tests were performed on the unirradiated and irradiated samples using a closed loop Instron 5967 machine with 5K N load cell. The tensile tests were carried out at a cross-head speed of 2×10^{-3} mm/s (strain rate of 1×10^{-3} s⁻¹) at room temperature. Since the tensile samples were relatively bigger than other test samples, they were more radioactive. A single representative sample read on contact 50 mRem/hr gamma and 1.5 mRem/hr gamma at 30 cm. Therefore, special clothing was used to shield the radiation, and direct contact with the samples during testing was avoided. Special lead gloves were used to shield gamma radiation during the

loading and unloading of the tensile samples (Figure 3.15) and continuous check for any contamination during the test was performed using Geiger counter.



Figure 3.15: Tensile test for radioactive steel samples conducted at Center for Advanced Energy Studies (CAES) using Instron machine.

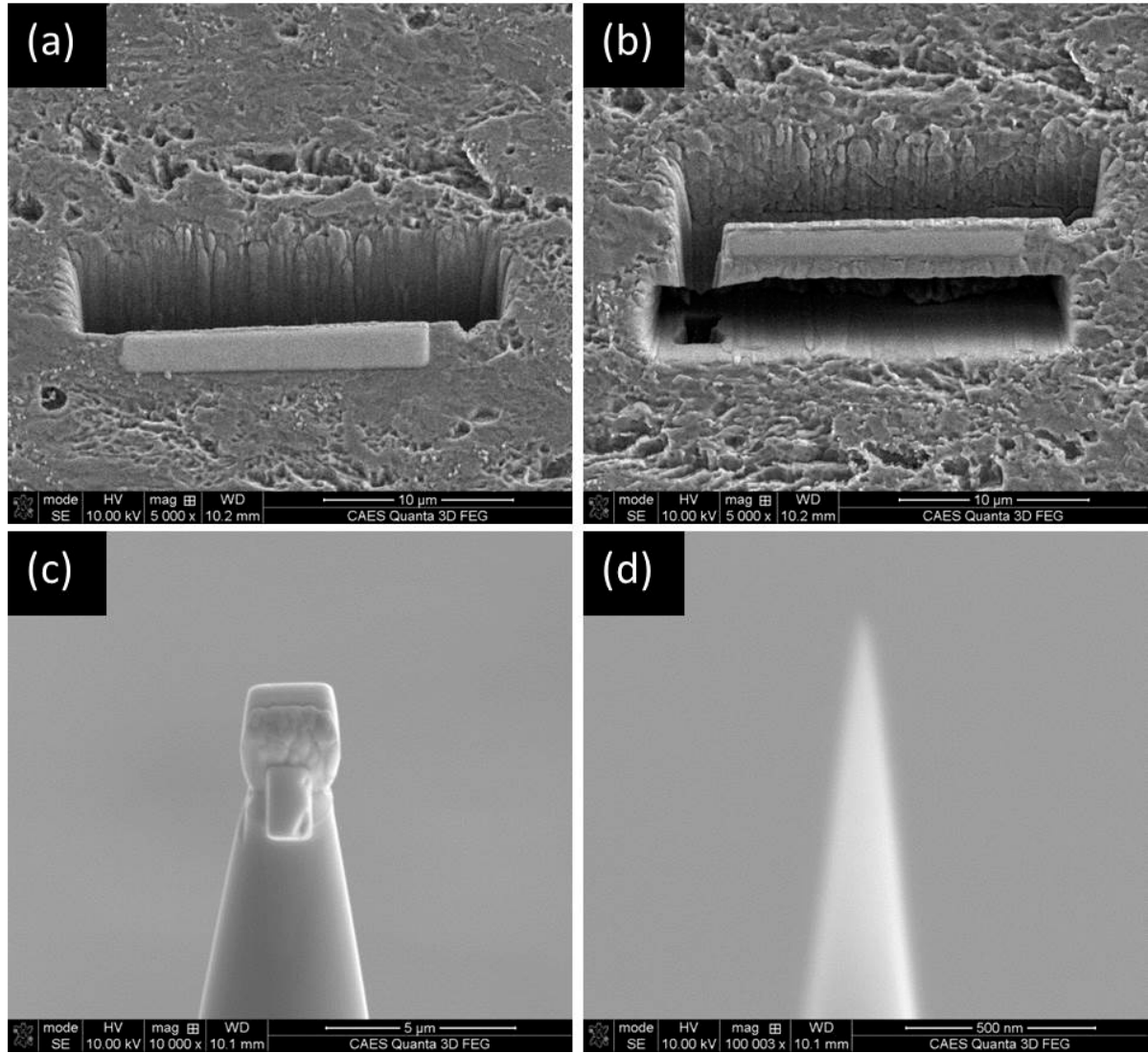


Figure 3.16: Needle-shape atom probe specimen geometry preparation using the focused ion beam technique.

Chapter 4. Microstructural Characteristics

In this chapter, the results of the post irradiation experiments on microstructures at two different doses on both UFG and CG steels are presented and discussed. Radiation exposure poses different effects at different doses. While low doses (0.001 dpa) induce irradiation hardening and embrittlement, irradiation at higher dose (above ~ 1 dpa) causes more damage and poses significant potential for radiation enhanced segregation (RES) [30, 100] at grain boundaries and radiation induced precipitation (RIP) [10]. These microstructural phenomena are investigated and discussed in this chapter.

4.1 Grain Size Distributions

The grain size for both steels was measured before and after irradiation to different doses. TEM studies were conducted to determine grain size distributions in UFG steel and the bright field (BF) TEM images are shown in Figure 4.1 for both pre and post irradiation cases. Randomly oriented ultra-fine grain microstructure is observed in both unirradiated and irradiated materials. The TEM images show highly strained areas because of the SPD processing. Dark field (DF) TEM images revealed better estimations for the grain size of UFG and nano materials than BF images and thus, many DF images were collected for each case (Figure 4.2) and an average of about four hundred grains (from both DF and BF images) was used to estimate the average grain size. Mean grain sizes along with their standard deviations are shown in Table 4.1. As expected from the low irradiation temperature, no significant grain growth occurred following irradiation unlike in the case of Cu where

radiation-induced grain growth was reported [76]. However, broad distributions of grain size were noted in both irradiated and unirradiated UFG steels (Figure 4.5).

Grain sizes distributions were also determined for CG steel. Figure 4.3 and Figure 4.4 show optical micrographs for both unirradiated and the 0.001 dpa irradiated CG steel and EBSD micrographs for unirradiated and irradiated (1.37 dpa) CG steel, respectively. Different methods (optical and EBSD) were used since EBSD is not available at NCSU campus for characterizing low dose irradiated samples. The mean grain sizes along with their standard deviations are included in Table 4.1 for each condition. Similar to UFG steel, broad distributions of grain size were revealed in both irradiated and unirradiated CG steels (Figure 4.5). After irradiation to 1.37 dpa no significant change in grain size is observed. However, post irradiation to low dpa (0.001), grain size of CG samples tends to exhibit slight increase albeit very small considering the measurement scatter (grain size distribution); the values are overlapping in terms of the data scatter (4.4 ± 1.8 and 5.9 ± 2.4 μm). The increase in grain size could be attributed to the difference between optical and EBSD micrographs; in optical microscopy if a grain was not etched it will not be observed leading to slight increase in grain size.

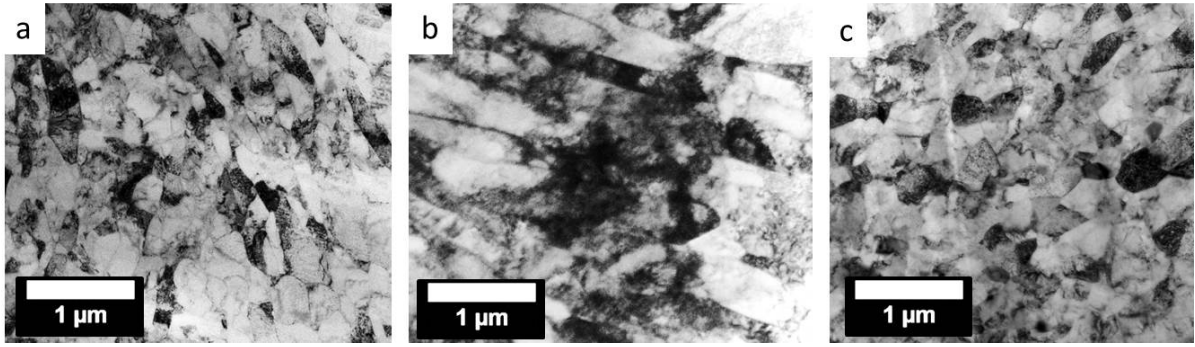


Figure 4.1: TEM bright field micrographs for UFG steel before irradiation (a), after irradiation to 0.001 dpa (b), and after irradiation to 1.37 dpa (c).

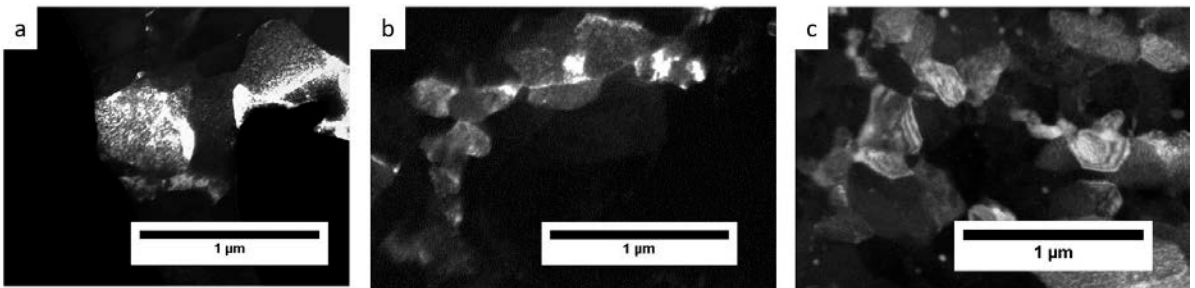


Figure 4.2: TEM dark field micrographs for UFG steel before irradiation (a), after irradiation to 0.001 dpa (b), and after irradiation to 1.37 dpa (c).

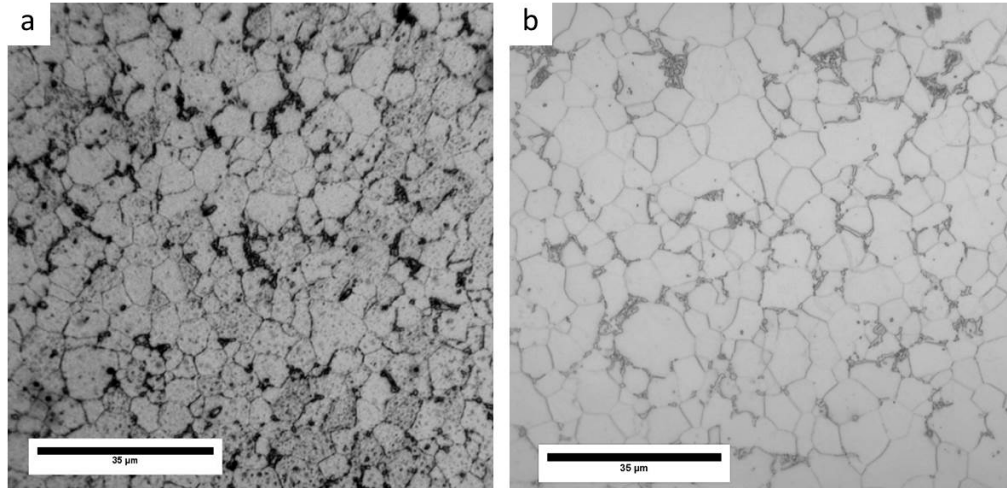


Figure 4.3: Optical micrographs for CG steel before irradiation (a) and after irradiation to 0.001 dpa (b).

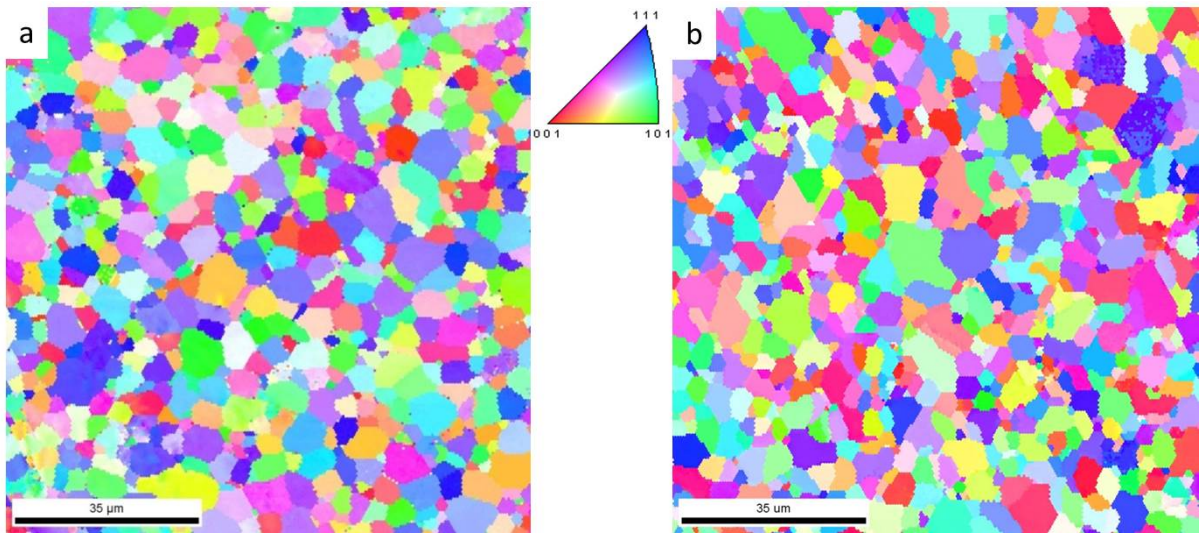


Figure 4.4: EBSD micrographs for CG steel before irradiation (a) and after irradiation to 1.37 dpa (b).

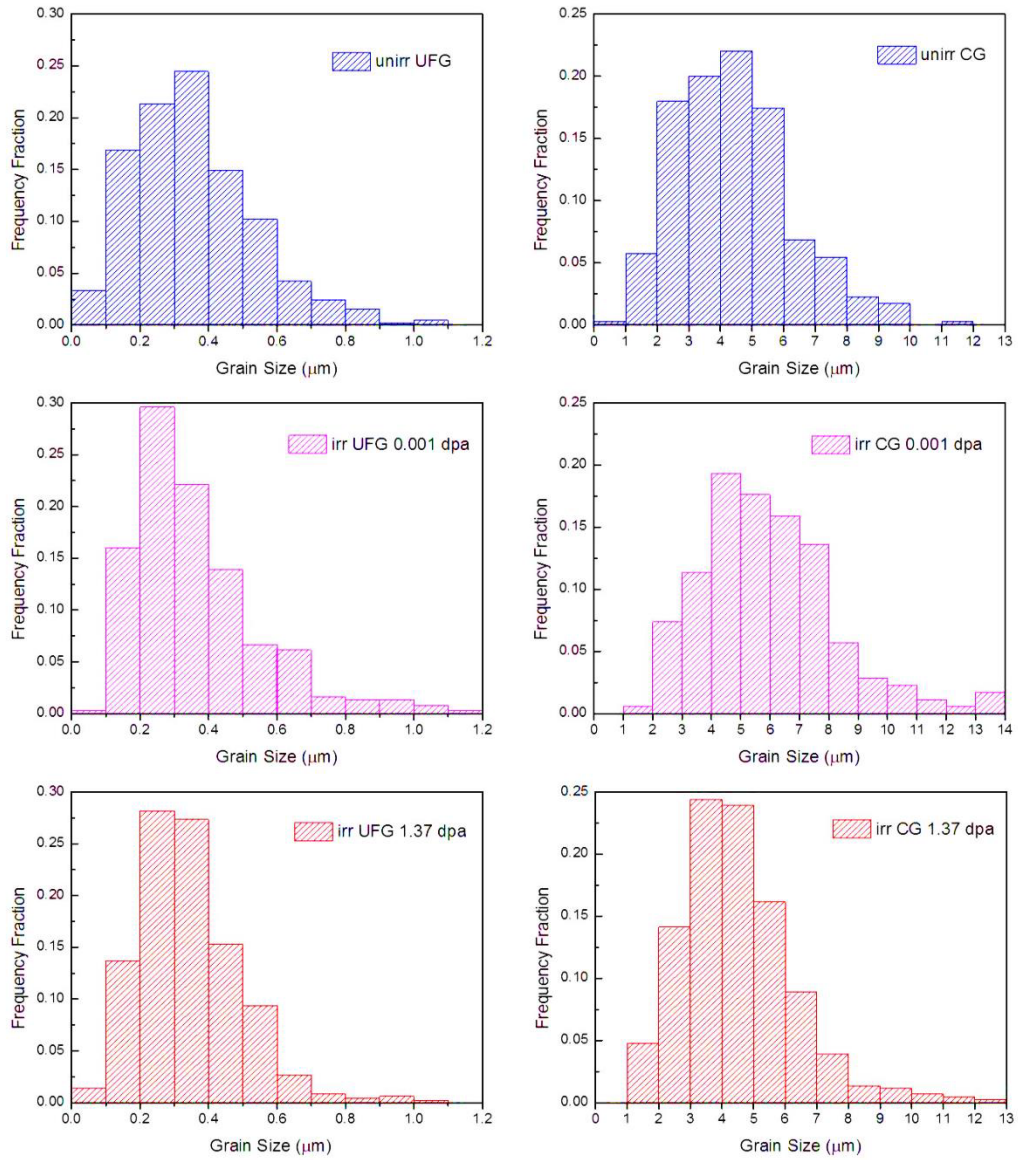


Figure 4.5: Grain size distributions of UFG steel (a, b, c) and CG steel (d,e,f) before and after irradiation to different doses.

Table 4.1: Mean grain size (μm) for both UFG and CG steel pre and post irradiation.

Mean Grain Size	Un Irradiated	0.001 dpa	1.37 dpa
UFG Steel	0.35 ± 0.18	0.36 ± 0.19	0.34 ± 0.15
CG Steel	4.42 ± 1.82	5.89 ± 2.35	4.51 ± 1.78

4.2 *Irradiation Induced Defects*

Figure 4.6 shows TEM observations under two beam conditions for both UFG and CG steels before and after irradiation. All images were obtained at $g=\langle 011 \rangle$ two beam condition (Figure 4.7); this condition is commonly used to reveal the defects in ferritic steels. TEM results obtained from neutron irradiated UFG steel (Figure 4.6 d, e and f) are remarkably different compared to the conventional grained irradiated steel. TEM observations reveal no evidence of irradiation induced defects or increase in dislocation density in UFG steel after irradiation. However, in CG steel, dislocation networks were observed post irradiation to low dose, whereas after irradiation to 1.37 dpa, high number of irradiation-induced sand-like black dot defects are observed in the grain interior of CG steel (Figure 4.6 c). In order to quantify the damage observed in TEM images, X-ray analysis is performed on both UFG and CG steels before and after irradiation to 1.37 dpa (Figure 4.8). The XRD peaks show that there were no phase changes due to irradiation in both steels. All the X-ray diffraction peaks were fitted simultaneously using Modified Rietveld technique with suitable weightage by a pseudo-Voigt (pV) function using the LS1 program [101]. Rietveld method was developed in 1967 [102] to investigate materials microstructures using X-ray diffraction line profile analysis. Later, Lutterotti proposed the modified Rietveld technique that offers several advantages with respect to traditional Rietveld methods [101]. LS1 program uses the Modified Rietveld technique in its analysis and includes the simultaneous refinement of the crystal structure and the microstructural parameters like the domain size and the microstrain within the domain. The method involves Fourier analysis of the broadened peaks. Considering an isotropic model, the lattice parameters (a), surface

weighted average domain size (D_s) and the average microstrain $\langle \varepsilon_L^2 \rangle^{\frac{1}{2}}$ were used simultaneously as the fitting parameters to obtain the best fit [103]. Figure 4.9 represents a typical whole pattern fit using LS1 program for irradiated CG steel. Using the results obtained from the XRD analysis, the dislocation density, ρ has been estimated from the following relations [104],

$$\left. \begin{aligned} \rho &= (\rho_D \rho_S)^{\frac{1}{2}} \\ \rho_D &= \frac{3}{D_s^2} \\ \rho_S &= k \langle \varepsilon_L^2 \rangle / b^2 \end{aligned} \right\}, \quad (4.1)$$

where ρ_D and ρ_S are the dislocation densities due to domain size and strain respectively, k is material constant equal to 14.4 for bcc metals [104]. The dislocation density calculations for both steels (UFG and CG) and their associate error analyses are included in Appendix A, and the X-ray analysis results are summarized in Table 4.2. Significant changes are observed in the values of the domain size and micro strain of the CG steel after irradiation to 1.37 dpa due to the increased defect concentration after neutron irradiation. As shown in Equ 4.1, dislocation density is proportional to the micro strain but inversely proportional to the domain size and thus the dislocation density for irradiated CG steel is found to be about 4 times higher than before irradiation. On the other hand, UFG steel didn't show significant change in its dislocation densities (values are within the error bars). This can be attributed to the high density of grain boundaries in UFG steel that act as sinks for irradiation-induced defects. This agrees with the earlier results obtained from the transmission electron microscopy.

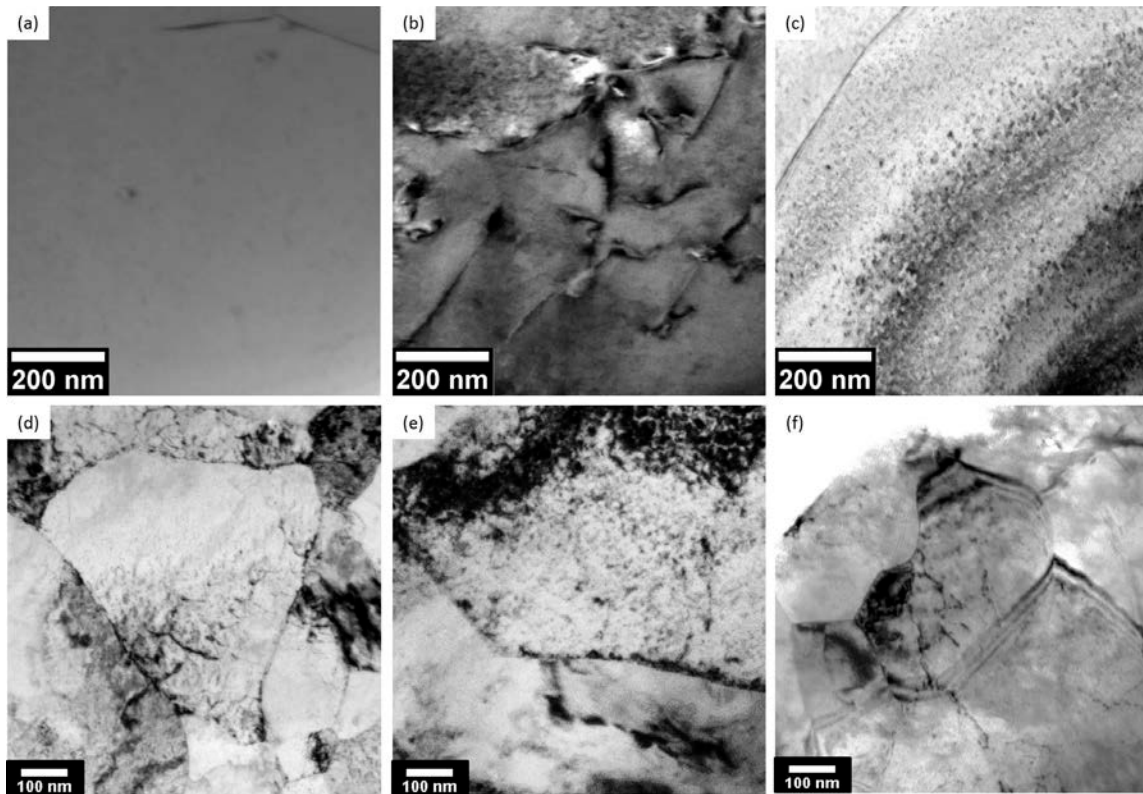


Figure 4.6: TEM micrographs of CG steel unirradiated (a), CG steel irradiated to 0.001 dpa (b), CG steel irradiated to 1.37 dpa (c), UFG steel unirradiated (d), UFG steel irradiated to 0.001 dpa (e) and UFG steel irradiated to 1.37 dpa (f).

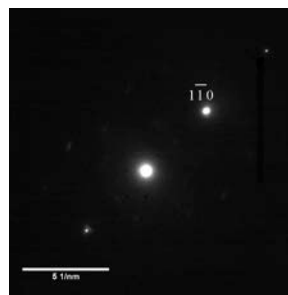


Figure 4.7: Typical two beam condition diffraction pattern used to observe the defects; same condition was used for all cases.

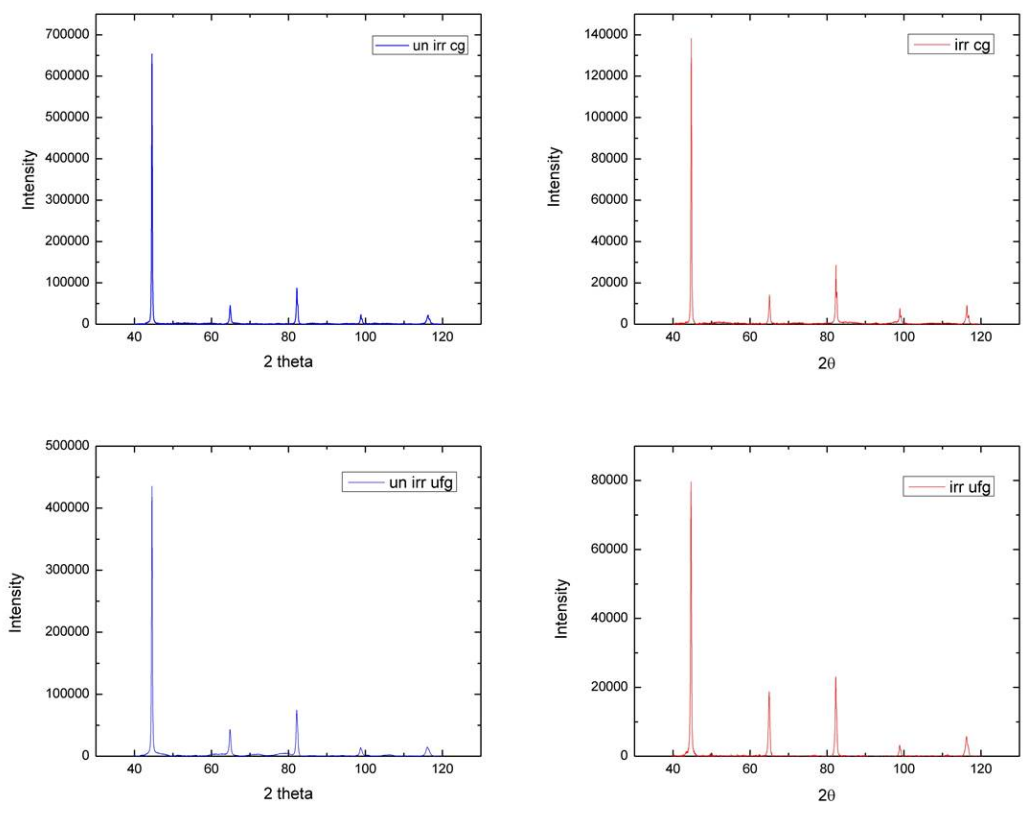


Figure 4.8: XRD profiles for unirradiated and irradiated (1.37 dpa) UFG and CG steels.

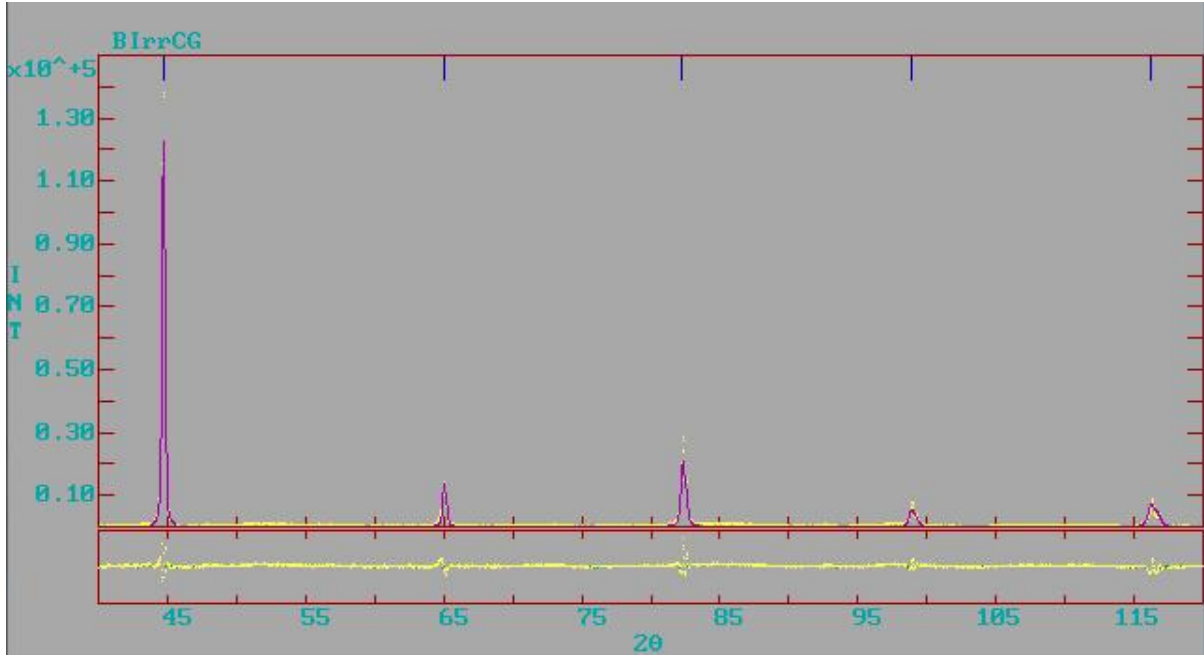


Figure 4.9: Whole XRD pattern fit for irradiated CG steel at dose 1.37 dpa using LS1 program.

Table 4.2: Values of domain size (D_s), microstrain ($\langle \epsilon_L^2 \rangle^{\frac{1}{2}}$) and dislocation density (ρ) for different samples obtained by Modified Rietveld analysis.

Sample	D_s (Å)	$\langle \epsilon_L^2 \rangle^{\frac{1}{2}}$	ρ (m ⁻²)
Unirr CG	1850	7.4×10^{-4}	$1.06 (\pm 0.13) \times 10^{14}$
Irr CG (1.37 dpa)	622	1.00×10^{-3}	$4.26 (\pm 0.56) \times 10^{14}$
Unirr UFG	385	1.38×10^{-3}	$9.50 (\pm 1.24) \times 10^{14}$
Irr UFG (1.37 dpa)	366	1.24×10^{-3}	$8.98 (\pm 1.39) \times 10^{14}$

4.3 Irradiation Enhanced Segregation

The embrittlement of steels is due to the interactions of many microstructural variables that occur at the nano and micro scales. Hence, steel microstructural changes due to neutron irradiation were investigated using APT to understand the changes that occur post neutron irradiation. The reconstructed three dimensional atom maps of Si, Mn and C are shown in Figure 4.10 and Figure 4.11 for UFG and CG steels respectively. In UFG steel (Figure 4.10), the grain boundaries were observed in both unirradiated and irradiated samples by solute enrichment that can only be attributed to segregation at grain boundaries. In CG steel, the average total length of the matter analyzed for both unirradiated and irradiated is about 150 nm. Since the mean grain size for CG steel is about 4.4 μm , no grain boundary was observed in these volumes. The concentration profiles across the grain boundary are plotted in Figure 4.12 for both irradiated and unirradiated UFG steels. The results revealed that for unirradiated as fabricated steel, both Si and C atoms show enrichment at grain boundaries while Mn atoms slightly deplete. Alloying elements will segregate near boundaries so that strain energy can be minimized [105]. However, irradiation-induced defects (vacancies and self-interstitials) influence the mobility and tendency for segregation of the solutes and can change the make-up of enriching and/or depleting species based on their relative diffusivities. Post irradiation examinations indicate grain boundary segregation with all solute atoms. While Si and Mn are considered to be substitutional solute atoms in bcc iron, C is an interstitial solute. After irradiation, point defects produced due to the interactions between neutrons and lattice atoms tend to recombine at grain boundaries. Hence, there are two kinds of atom fluxes that need to be considered; first, solute atoms moving opposite the vacancy

flux (away from grain boundary) and secondly, the interstitial solute atoms which move toward the grain boundary. In the Inverse Kirkendall effect, the flux of vacancies tends to make the more mobile solute atoms move in the opposite direction to the vacancies. Hence, when the participation of one solute element in the atom fluxes is higher than others, a net accumulation of this element and a corresponding depletion of other elements happen at the grain boundary giving rise to concentration gradients [106]. Also, point defects tend to have a preferential association with particular alloying elements [19]. For the solute drag effect, oversized solutes tend to associate with vacancies while undersize with interstitials and the pair migrates together to a sink [107]. Due to the high grain boundary density of the UFG steels, the probability that irradiation produced defects find a sink vs. recombination is increased and consequently the degree of radiation-induced segregation increases at the grain boundaries. Figure 4.12 shows that Mn and Si have a higher level of grain boundary segregation compared to C even though the activation energy for C interstitial diffusion in iron is lower than substitutional diffusion of Si and Mn in iron. This is because most of the C atoms tend to diffuse to form carbide precipitates and to dislocations which act as traps for interstitials. Thus fewer numbers of C atoms are available to segregate around the grain boundary. APT results also revealed that Mn solute atoms diffused along with carbon atoms resulting in high concentration of Mn atoms at the carbide boundaries. However, Si atoms don't follow similar trend (Figure 4.13).

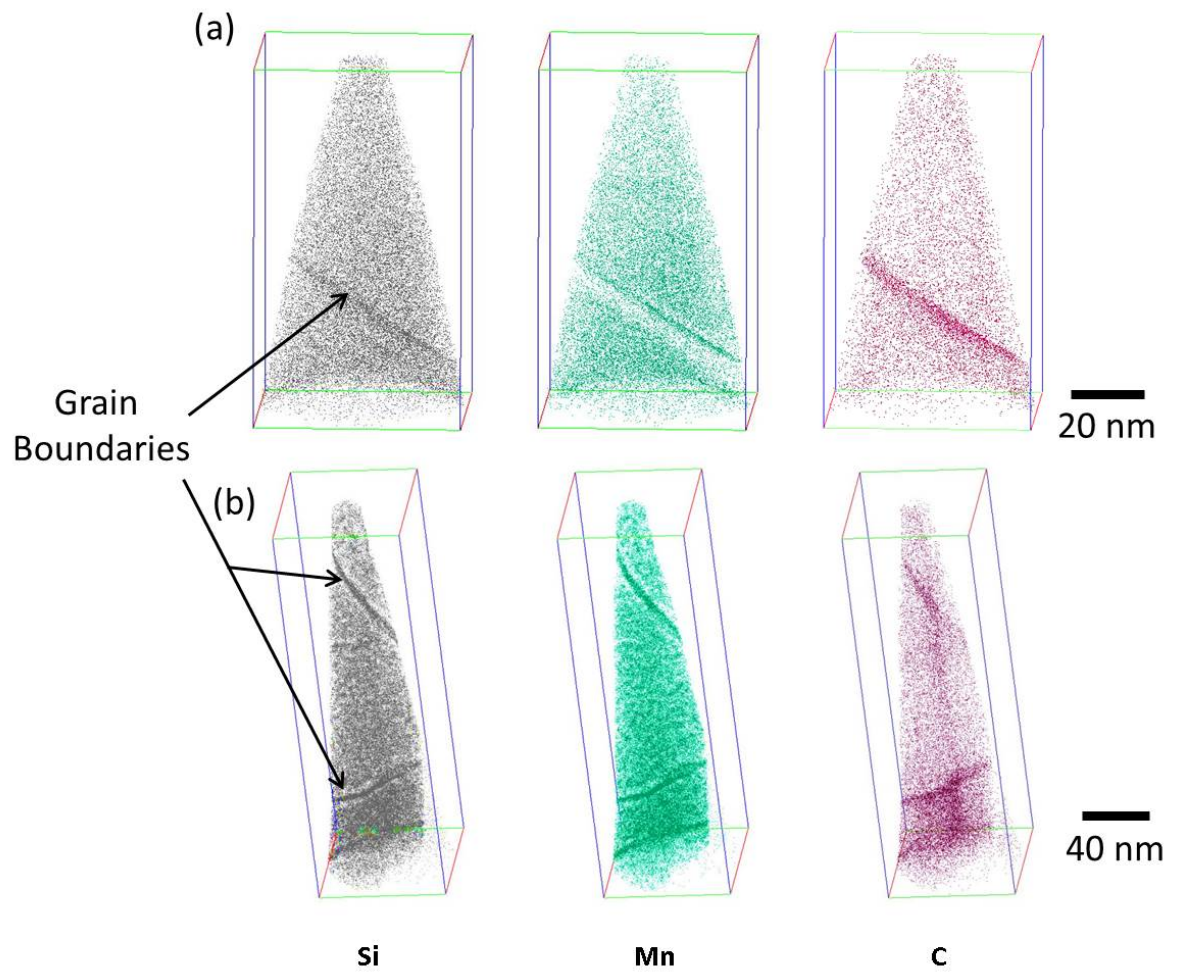


Figure 4.10: Representation of three-dimensional reconstruction of UFG steel, (a) before and (b) after neutron irradiation by three-dimensional (3D) atom-probe microscopy.

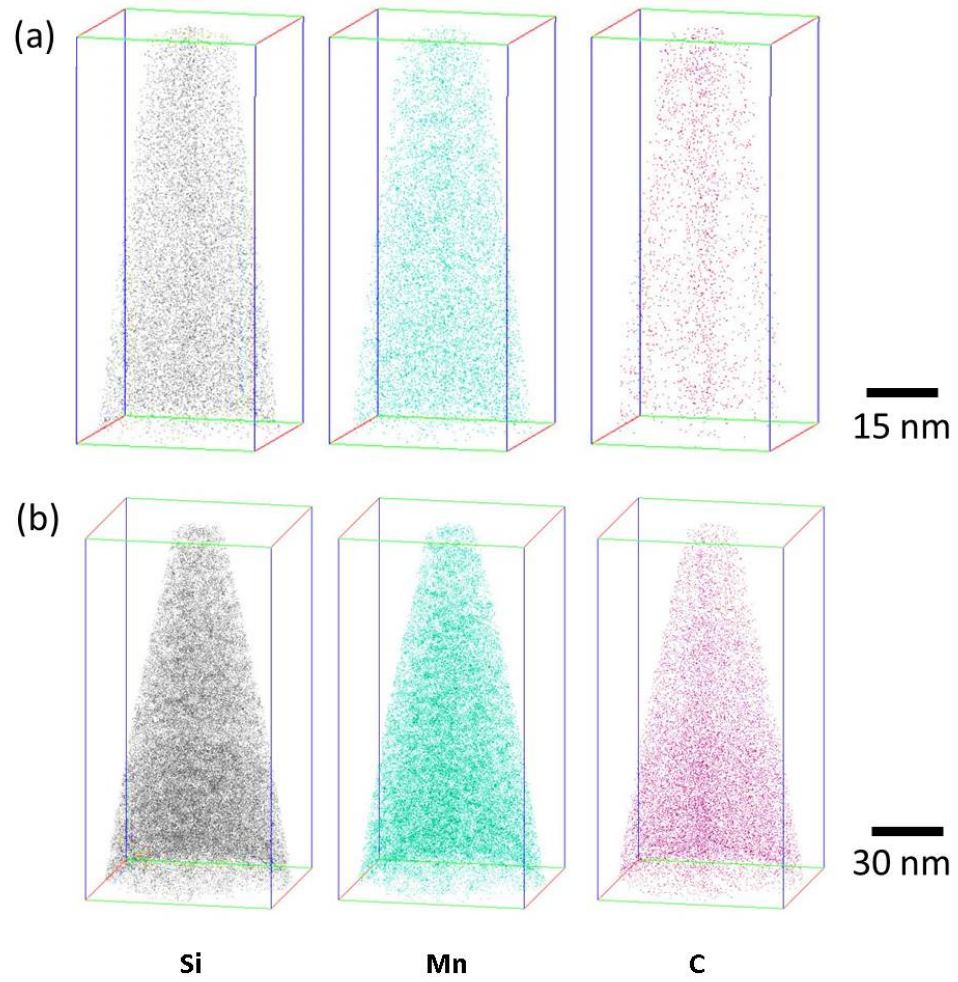


Figure 4.11: Representation of three-dimensional reconstruction of conventional grained steel, (a) before and (b) after neutron irradiation by three-dimensional (3D) atom-probe microscopy.

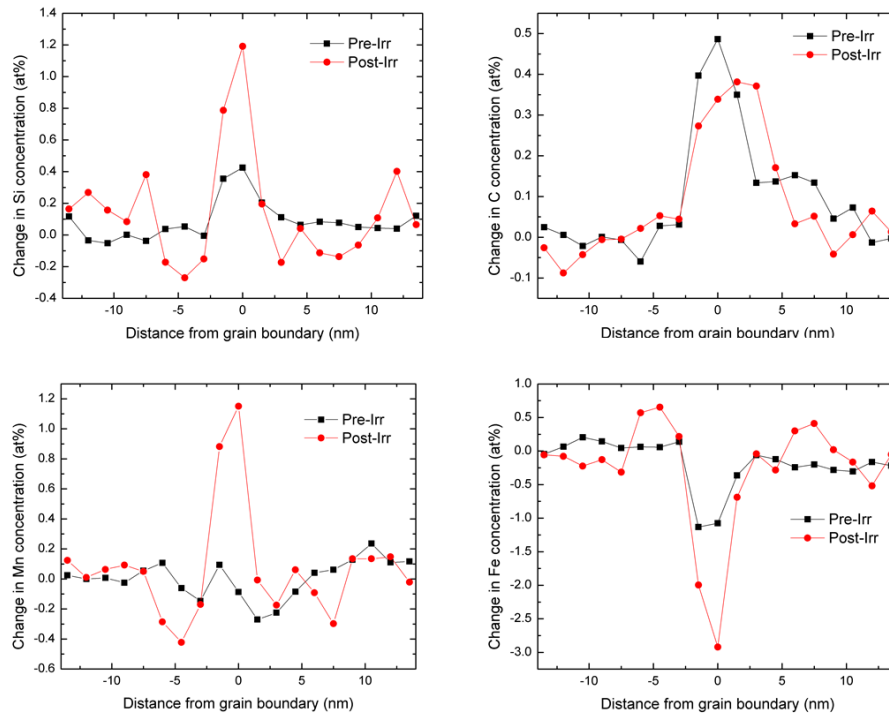


Figure 4.12: Irradiation enhanced segregation at grain boundaries in UFG steel.

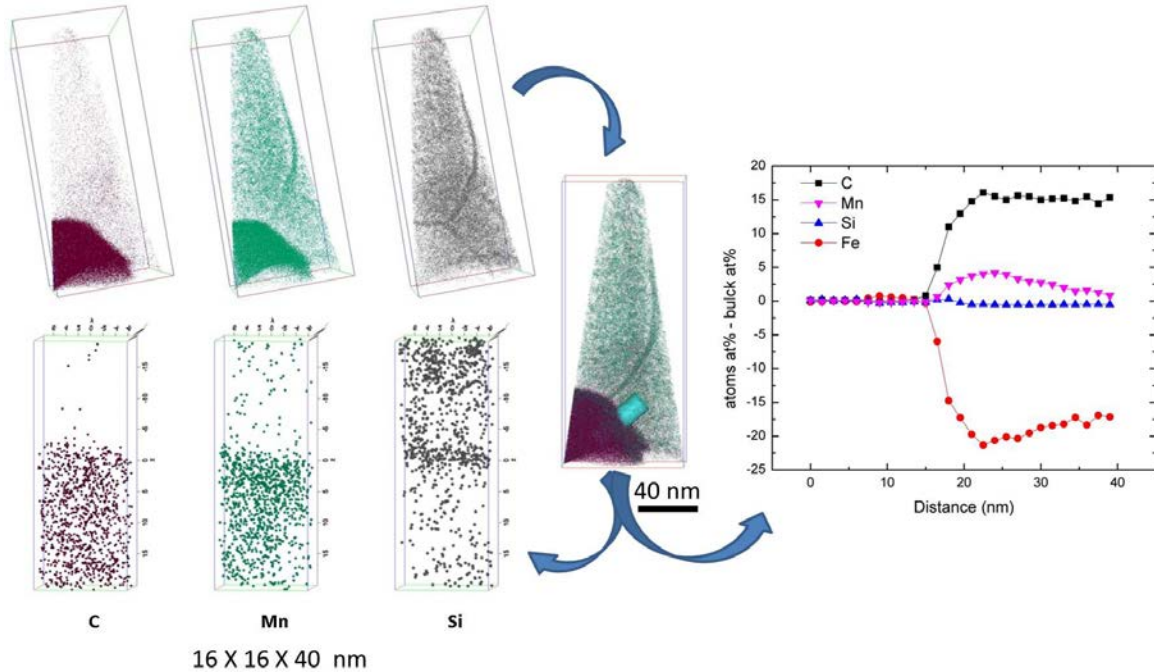


Figure 4.13: Post irradiation atomic arrangements around carbide precipitate in UFG steel. Atom concentrations inside the selected cylinder are shown in the right.

4.4 Irradiation Induced Clustering

As shown in the previous section, irradiation can cause local enrichment or depletion of solutes. If the local solute concentration exceeded the solubility limit, solute clusters or precipitates are formed. Solute atom analysis was performed using statistical methods to detect deviations from a random solid solution. While un-irradiated samples for both CG and UFG steels revealed no deviation from random solute distribution, irradiated samples showed evidence of clustering (Figure 4.14); solute atoms within a cluster will, on average, be closer to each other than solute atoms in the matrix. A maximum separation method was used to identify the clusters in the irradiated materials [108]. This process is illustrated schematically

in Figure 4.15 and it defines a cluster based on a concept of nearest neighbor analysis. The solute atoms are identified as precipitate solute atoms (not solute atoms in a random solid solution) if they are within a maximum separation distance, D_{\max} from one another. Minimum size of clusters in terms of solute atoms that constitutes a significant cluster (N_{\min}) is used to define a cut-off limit for the minimum size of a cluster, so that any cluster with less number of solute atoms will not be considered. In order to include non-solute atoms in the defined cluster, all the matrix atoms within a distance L from the solute atoms are taken as being part of the same cluster (Figure 4.15 c and d). However, this process results in a shell of matrix atoms being included around each cluster. Thus, an erosion distance E is used to remove the shell of matrix atoms that lies within a distance less than E from the nearest atom not defined as being part of the cluster (Figure 4.15 e and f) [108–110].

Based on the deviation of the solute distribution in the tested specimens from random distribution, the maximum separation between solute atoms (D_{\max}) was chosen to be 0.6 – 0.7 nm. Both the maximum separation of additional elements (L) and the erosion distance for removal of atoms near the cluster matrix interface (E) are equal to D_{\max} . The minimum size of the cluster in terms of solute atoms that constitutes a significant cluster (N_{\min}) is taken as 11 atoms. The matrices of un-irradiated UFG and CG steel are found to be solid solutions with no solute clustering. However, APT characterizations of the irradiated steel revealed formation of Mn–Si-enriched nanoclusters (Figure 4.16). The fact that these small clusters were not observed before irradiation confirms that their formation was radiation-induced. The cluster number density is estimated using:

$$Nv = \frac{n_p \xi}{nV} , \quad (4.2)$$

where n_p and n are the number of clusters in the analyzed volume and the total number of atoms in the same volume, respectively. V is the atomic volume and ξ is the detection efficiency which is $\sim 37\%$ for LEAP-HR [110]. The cluster size is estimated by finding the Guinier radius for spherical precipitates using [36, 98]:

$$r_G = \sqrt{\frac{5}{3}} l_g , \quad (4.3)$$

where l_g is the standard radius of gyration. The average size (radius) of gyration of the nanoclusters is found to be 0.75 and 0.7 nm for the UFG and CG steels, respectively. This yields an average Guinier radius of 0.97 ± 0.23 and 0.9 ± 0.16 nm, respectively (Figure 4.17). The number density of clusters is $1.2 \times 10^{24} \text{ m}^{-3}$ and $6.7 \times 10^{23} \text{ m}^{-3}$ for the UFG and CG steels, respectively.

The irradiation temperature was relatively low ($\sim 80^\circ\text{C}$) and thus defect mobility will be relatively low thereby increasing the defect recombination rate and limiting the number of defects available to annihilate at sinks. However, the large grain boundary area per unit volume and the high dislocation density (resulting from the severe plastic deformation through ECAP processing) in UFG steel, increase the probability that the defects will migrate to the sink before being recombined. Thus, significant participation of solutes in the defect fluxes results in pronounced segregation at sinks, raising the local concentration above the solubility limit and thus having higher number density of clusters in UFG steel compared to CG steel that were irradiated at the same conditions.

The observed enriched Si-Mn clusters in both irradiated steels act as barriers for dislocation motion leading to increased strength of the irradiated materials (irradiation hardening). A detailed quantitative analysis of the influence of those clusters on the mechanical properties of the irradiated steels is presented later in section 5.2.

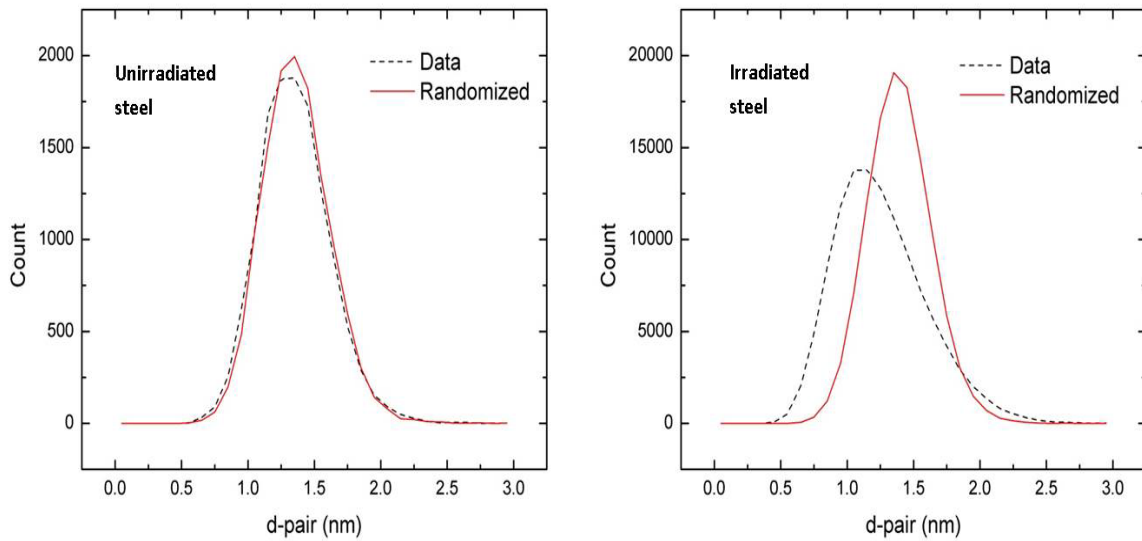


Figure 4.14: Comparison between random distribution of solutes in the matrix and the data obtained for both unirradiated (left) and irradiated CG steel (similar results were obtained from all the examined specimens for both CG and UFG steels).

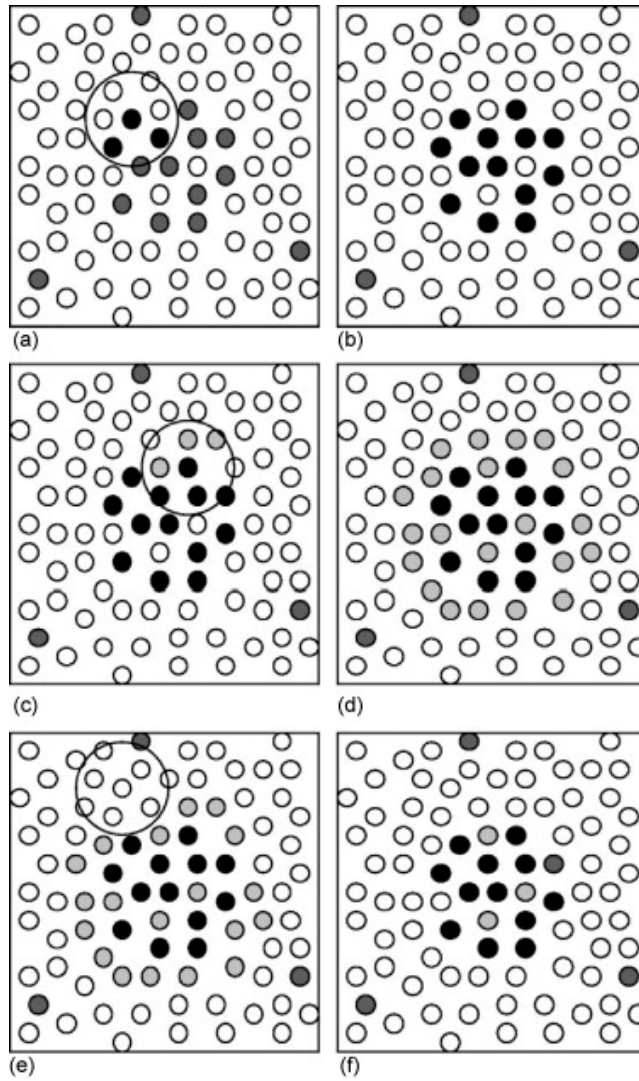


Figure 4.15: Schematic showing the maximum separation method: (a) and (b) solute atom selection (the core atoms); (c) and (d) selection of other atoms within a distance L of the core atoms; (e) and (f) erosion of atoms within a distance E of any other atom. Selected solute atoms are shown black, selected matrix atoms are shown hatched, not selected solute atoms are drawn grey and non-selected matrix atoms are shown white [110].

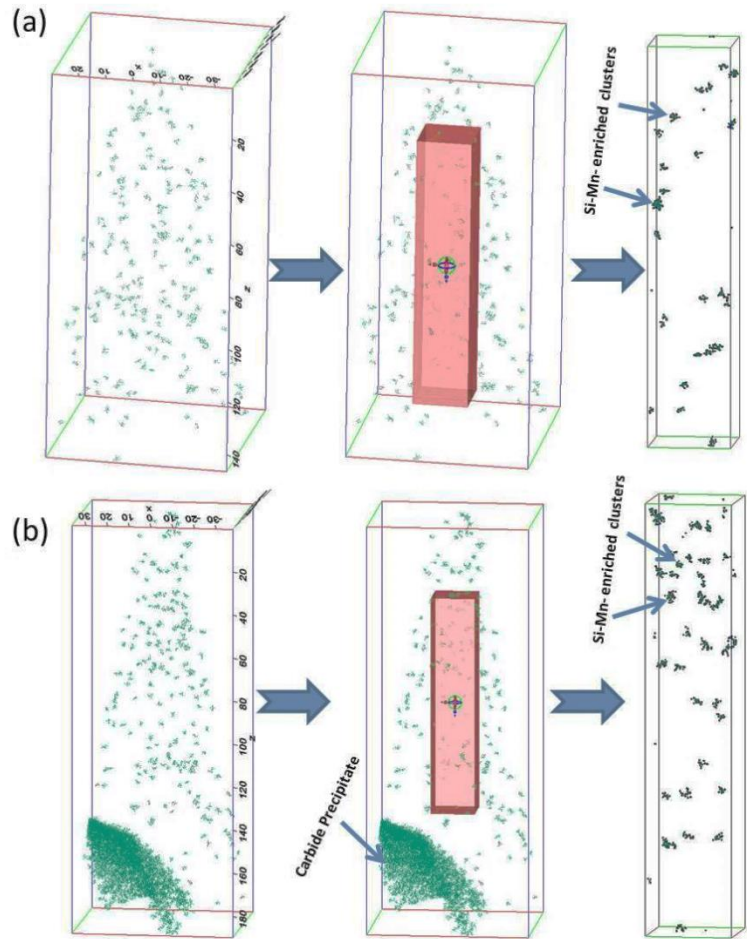


Figure 4.16: Si-Mn-enriched cluster distribution post neutron irradiation for (a) CG and (b) UFG steel. The dimension of the analysis boxes is 20X20X100 nm.

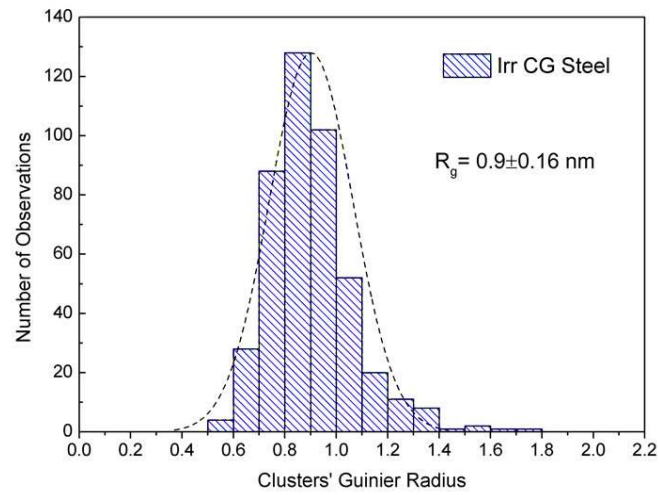
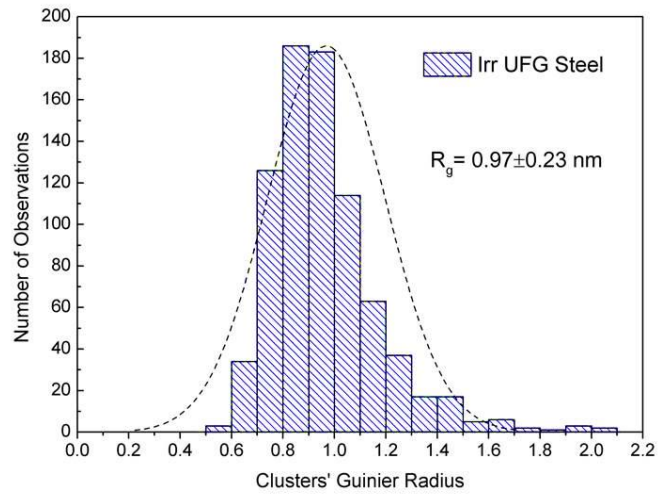


Figure 4.17: Size distribution of Si-Mn- enriched precipitates in the neutron irradiated (a) UFG and (b) CG steels.

Chapter 5. Mechanical Properties

5.1 Irradiation Induced Hardening and Embrittlement

Changes in the mechanical properties of the irradiated materials are due to the evolution of microstructural defects during neutron irradiation. Radiation hardening and embrittlement are of primary concern in neutron irradiated materials. Hardness and tensile tests were used to measure the increase in the material strength due to the radiation produced entities. Embrittlement is measured by the amount of plastic deformation that occurs before fracture and materials ductility obtained from tensile testing is used to assess this phenomenon.

5.1.1 Vickers Micro Hardness

The change in the micro hardness post irradiation was measured for both unirradiated and irradiated samples. Figure 5.1 shows Vickers micro hardness of UFG ferritic steels as a function of the irradiation dose. For comparison, micro hardness for CG counterparts was also shown. Before irradiation, Vickers hardness decreases from 3.09 GPa to 1.29 GPa as the grain size increases from 0.35 μm (UFG steel) to 4.4 μm (CG steel). After low dose irradiation, while CG shows an increase in hardness, no significant change was observed in UFG steel. However, after irradiation to 1.37 dpa, CG steel hardness increased by 62% while hardness of the UFG sample exhibited an increase of only 8.6%.

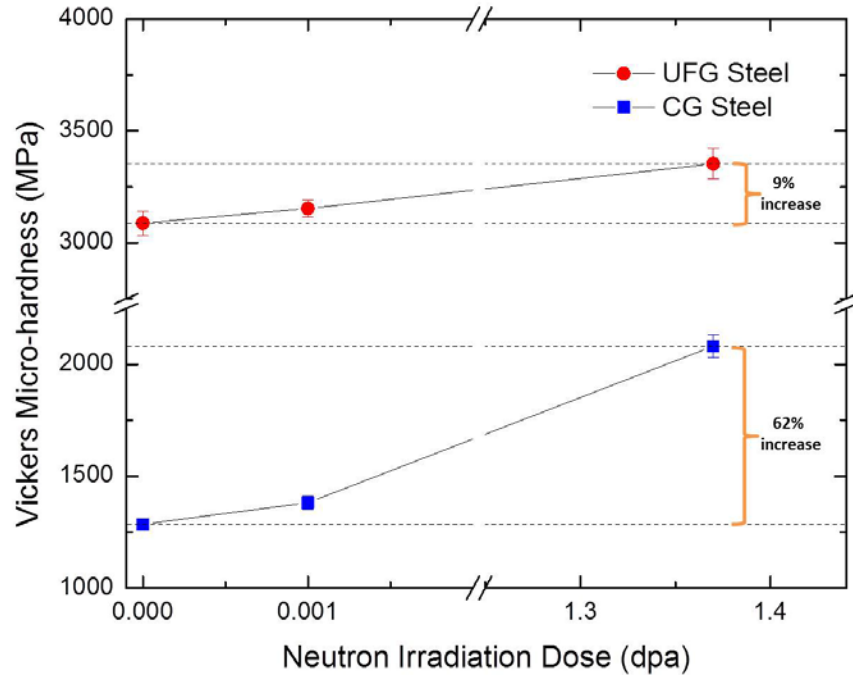


Figure 5.1: Micro-hardness before and after irradiation for both UFG and CG low carbon steels.

5.1.2 Nano Hardness

Nano indentation load-displacement curves of the tested steel samples before and after irradiation to 1.37 dpa are shown in Figure 5.2. The difference in the materials hardness is clearly indicated from the difference in the depth attained at the maximum load. It can be seen that the loading curve of the un-irradiated CG steel is not as smooth as other curves. There are jumps in the loading curve of this steel which is attributed to dynamic strain aging (DSA) observed during the plastic deformation of low carbon steels. Intermittent (locking-unlocking) movement of dislocations in the interstitial (carbon) environment is believed to be responsible for the DSA in this steel [111]. However, this phenomenon was not observed in

the irradiated CG samples, apparently because the carbon atoms are attracted to the irradiation-produced defects thus being unavailable to pin dislocations [20]. In the case of UFG steel with large grain boundary area density, the carbon impurity atoms migrate to the grain boundaries. Thereby, the impurity atoms are unavailable to move to the dislocations to hinder their motion. This agrees with the tensile results shown later in this chapter (section 5.1.3). Figure 5.3 includes the nano hardness for the materials at different loads. It is noted that the hardness didn't show substantial indentation size effect and the values didn't change significantly with load. However, the hardness tends to slightly decrease as the applied load increases and the minimum hardness value for all cases is reported for 210 or 195 mN loads. It's important to note that the range of loads used in the nano indentation tests is rather small which may be the reason for not observing indentation load effect. The results reveal that nano hardness values of UFG steel before and after irradiation to 1.37 dpa overlapped at different applied loads (Figure 5.3). The average nano hardness values for CG steel increased after irradiation by 62.5% compared to 5.7% for the UFG steel.

As shown in equ 3.16, nano hardness is defined as the maximum load divided by contact area (A_c) at peak load. Since Oliver–Pharr method applies the purely elastic solution developed by Sneddon [112] to describe the elastic/plastic indentation process [113, 114], it was found that the area deduced from the analysis of the load-displacement curves underestimates the true contact area [114, 115] which in turn leads to overestimation of the hardness. Compared to micro hardness values, the nano hardness shows higher values. Nano indentation hardness is about 37 – 57 % higher in magnitude than the micro hardness (section 5.1.1). Figure 5.4 shows the SEM images of the nano hardness indents. While CG

steel shows clear difference in the indentation size after irradiation, the UFG material shows similar indentation sizes before and after irradiation indicating less influence of the neutron irradiation on the UFG steel compared to the CG steel. This agrees with the hardness values obtained from both nano and micro hardness measurements.

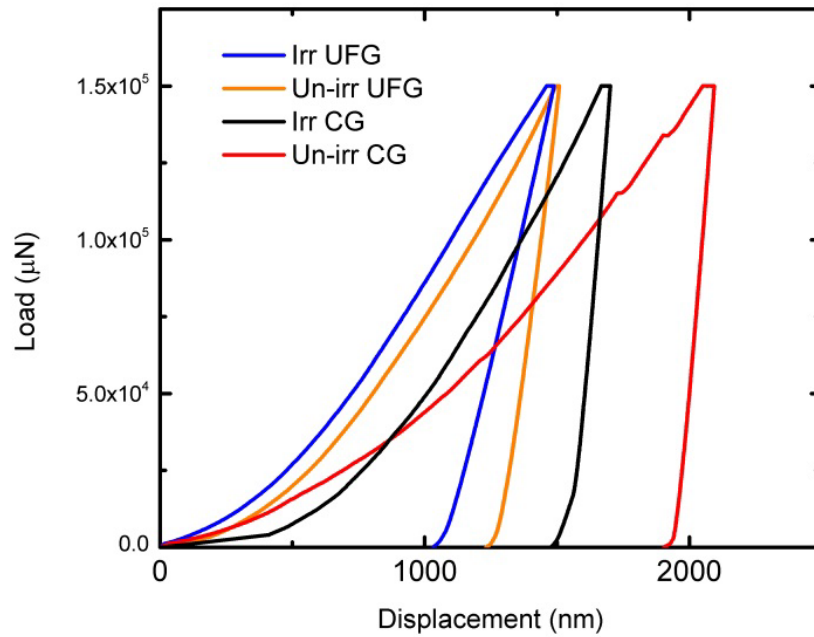


Figure 5.2: Load versus displacement for the 150 mN peak load experiment. Both UFG and CG steel were irradiated to 1.37 dpa.

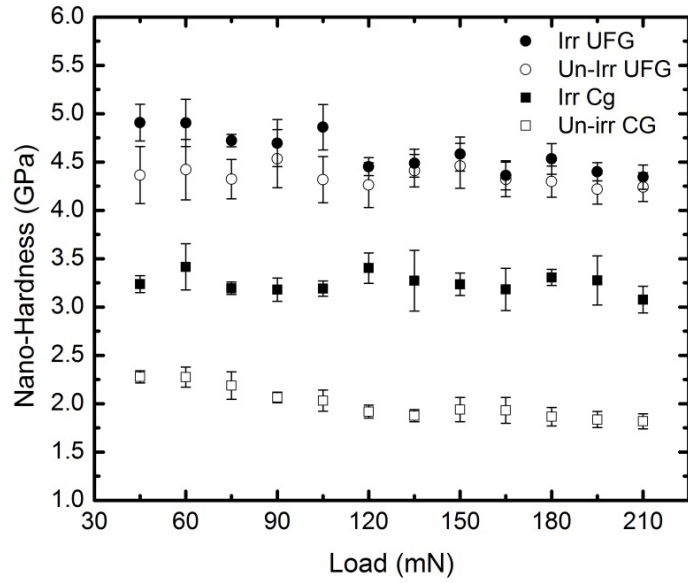


Figure 5.3: Nano hardness versus load for irradiated (1.37 dpa) and un-irradiated UFG and CG steels.

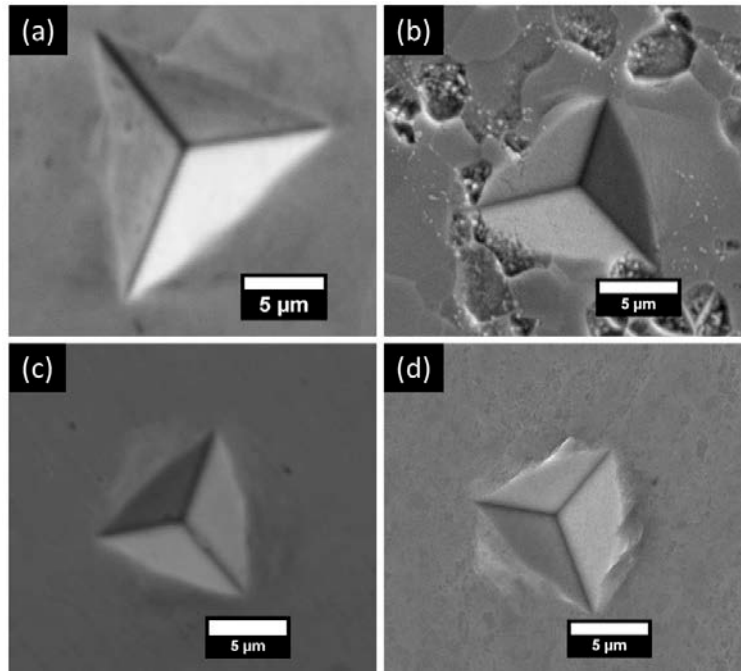


Figure 5.4: SEM images of nano indents at 210 mN for (a) Un-Irr CG (b) Irr-CG (c) Un-Irr UFG (d) Irr-UFG (1.37 dpa) low carbon steel.

5.1.3 Tensile Test

Mechanical characteristics were also evaluated from tensile tests using mini tensile samples (Figure 3.3 and Figure 3.4), and the appropriate results are tabulated in Table 5.1 and Table 5.2 for CG and UFG steels, respectively. Room temperature tensile tests were performed at a strain-rate of 10^{-3}s^{-1} , and three tests were performed for each condition. Figure 5.5 includes stress-strain curves for CG and UFG steel before and after neutron irradiation. Figure 5.5 shows that yield point phenomena is observed only in the unirradiated CG steel due to non-negligible source hardening attributable to the pinning of dislocations by impurity atoms (principally C) [28]. Before a Frank-Read (FR) source can be operated by the applied stress, dislocations have to be unpinned from the impurity atoms. However, during irradiation the impurity atoms get attracted to radiation produced defects thereby decreasing source hardening [116] resulting in reduced yield points which disappear following higher radiation dose (1.37 dpa). However, no yield point phenomena were observed in the UFG steel presumably because impurity atoms (principally carbon) tend to migrate to the grain boundaries thereby not being available for pinning the dislocations.

Higher strength of the UFG steel compared to the CG steel before irradiation is due to the grain refinement (Hall-Petch relation). After irradiation, the CG steel exhibits increased hardness and strength accompanied by decreased ductility as per the commonly observed radiation hardening and embrittlement. However, the UFG steel clearly indicates less significant changes. At low irradiation dose (0.001 dpa), the irradiation causes about 35% increase in the yield stress (YS) and 10% increase in ultimate tensile strength of the CG steel while it causes only 8% increase in the yield strength and 6% increase in ultimate tensile

strength of UFG steel. The reduction in UFG steel ductility is 10%. In contrast, the reduction in the CG steel ductility is 28%. After irradiation to 1.37 dpa the results show more extreme approach; CG yield strength increases by 132%, ultimate tensile strength increases by 94% and its ductility decreases by 82%. On the other hand, UFG steel yield strength increases by 30%, ultimate tensile strength increases by 8% and the ductility reduces by 56%.

To provide a basis for correlating the Vickers microhardness with bulk tensile properties measurements for the current low irradiation temperature experiment, a comparison between Vickers hardness and both yield and tensile strength is shown in Figure 5.6 where a linear relationship between the two property measurements is demonstrated for both UFG and CG steels. A linear least-squares fit to the Vickers hardness versus yield strength data yielded a slope of 3.19 MPa/MPa. If the Vickers hardness data is expressed in traditional units, this value corresponds to 3.19 MPa/(kgf/mm²). This value is slightly above the traditional value of 3.0 [117]. The linear least-squares fit to the Vickers hardness versus ultimate tensile stress (UTS) data showed a better fit compared to the yield stress data and yielded a slope of 2.9 MPa/MPa.

Although irradiation hardening was minute in the UFG steel compared to the CG as delineated by Figure 5.5, the irradiation induced embrittlement is clear in the UFG steel after irradiation to 1.37 dpa. However, the decrease in the ductility of UFG steel is quite less than that of CG counterparts. According to Odette and Lucas[35], the primary mechanism of embrittlement in ferritic steels is the hardening produced by nanometer size features that develop as a consequence of radiation exposure. However, since results showed that there is no significant change in dislocation density in UFG steel after irradiation, the high density of

irradiation induced Mn-Si-enriched clusters found in UFG steel is considered to be responsible for the observed irradiation induced embrittlement in UFG steel. In the next section, quantitative APT analyses as described earlier will be used to explain the observed radiation hardening.

Table 5.1: Tensile data for CG steel before and after irradiation to different doses.

CG Dose (dpa)	Yield Strength (MPa)	Tensile Strength (MPa)	Uniform Strain (%)	Ductility (%)	Hardness (MPa)
0	296±17.08	389.7±17.6	30.23±4	63±3.4	1285±13
1.00E-03	399.8±8.91	427.95±1	21.7±3.18	45.5±6.01	1381±30
1.37	687±20.43	754±20.39	2.4±0.53	11.3±1.37	2081±52

Table 5.2: Tensile data for UFG steel before and after irradiation to different doses.

UFG Dose (dpa)	Yield Strength (MPa)	Tensile Strength (MPa)	Uniform Strain (%)	Ductility (%)	Hardness (MPa)
0	775.3±8.7	980.3±11	4.1±0.3	18.4±1.99	3088±54
1.00E-03	840±7.1	1042.7±37.8	3.6±0.9	16.5±2.76	3153±39
1.37	1009±49.48	1060.35±42.7	0.6±0.3	8.1±1.2	3353±68

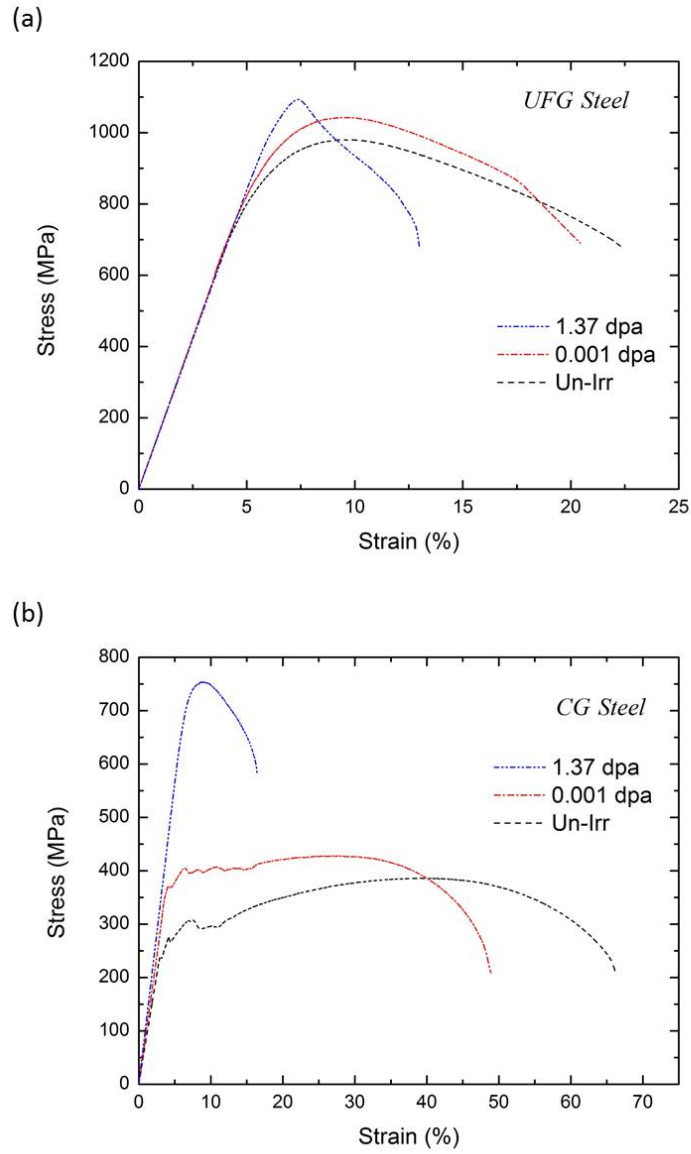


Figure 5.5: Engineering stress-strain curves for both steels (UFG and CG) before and after irradiation to different doses.

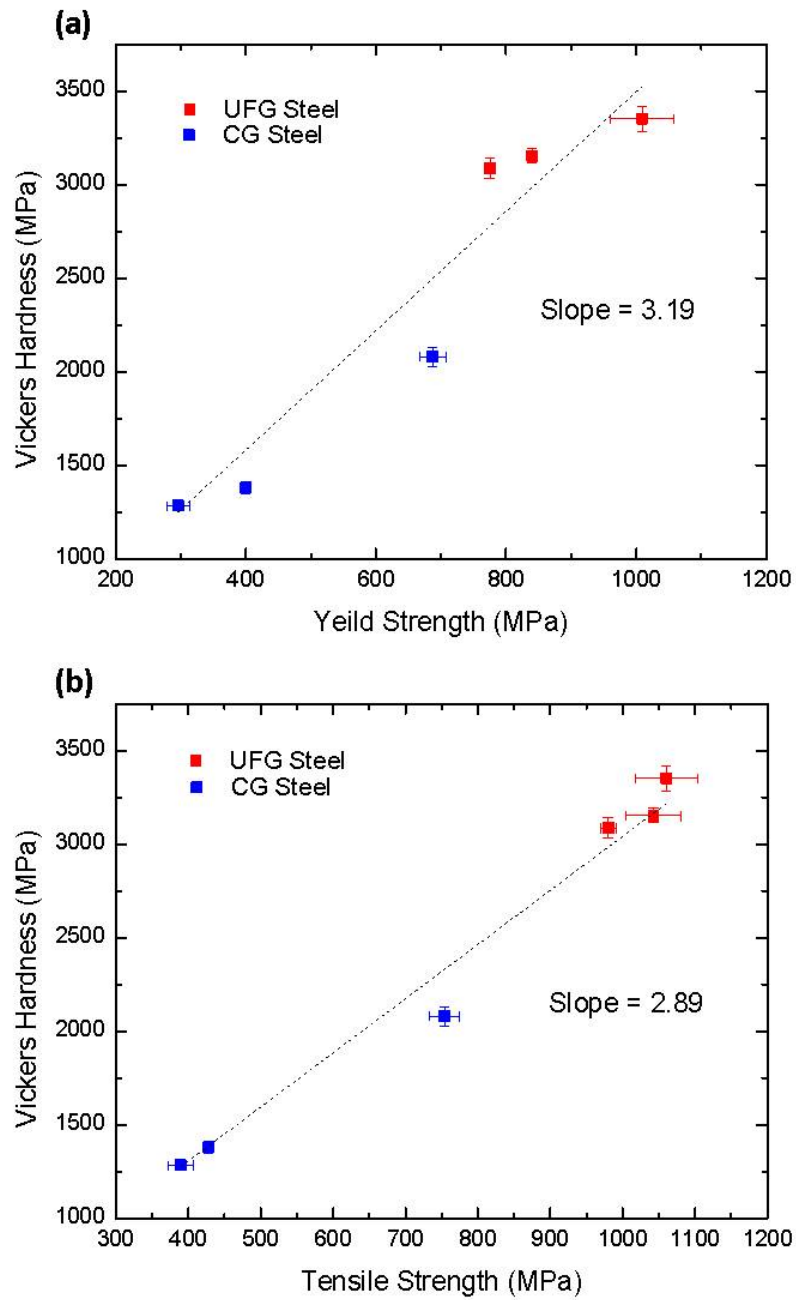


Figure 5.6: Correlation of yield (a) and tensile (b) strengths with hardness for UFG and CG ferritic steels before and after neutron irradiation.

5.2 *Hardening Mechanisms*

To achieve better understanding of the effect of irradiation microstructural changes on the steel's mechanical properties, the increase in yield stress is related to different strengthening mechanisms. After irradiation, four major mechanisms may be responsible for increased strength as shown in the following:

$$\Delta\sigma_{irr} = \Delta\sigma_{GS} + \Delta\sigma_{SS} + \Delta\sigma_{Clu} + \Delta\sigma_{Dis}, \quad (5.1)$$

where the subscripts GS, SS, Clu and Dis correspond to strengthening due to grain size, solid solution, clusters and dislocations, respectively. Grain boundaries impede dislocation motion and propagation to adjacent grains therefore any irradiation induced grain growth/shrinkage results in changes in the strength of the material (Hall-Petch effect, $\Delta\sigma_{GS}$). Interstitial or substitutional impurities cause lattice strain. As a result, these impurities interact with dislocation strain fields and hinder dislocation motion (solid solution strengthening, $\Delta\sigma_{SS}$). The interactions between dislocations and irradiation produced clusters restrict dislocation motion thereby making the material stronger and harder (Orowan hardening, $\Delta\sigma_{Clu}$). Irradiation increases the dislocation density. Thus, the average distance between dislocations decreases and dislocations start blocking the motion of each other (forest hardening, $\Delta\sigma_{Dis}$). However, no significant change in grain size is observed for both UFG and CG steels after irradiation to 1.37 dpa (Table 4.1). Thus, strengthening due to Hall-Petch effect is neglected ($\Delta\sigma_{GS}=0$). APT results showed that the percentage of solute atoms that left the matrix to produce clusters is very small (mean atomic concentration of solutes reduces by 0.05% after irradiation). Therefore, the change in the concentration of solutes before and after irradiation

doesn't cause any significant change in the hardening due to solid solution and the solid solution strengthening is ignored. As a result, the remaining two strengthening mechanisms dominate and they cause the increase in the strength after irradiation: cluster strengthening (Orowan precipitate strengthening) and strengthening by dislocations (forest strengthening). Thus, the change in the yield strength due to irradiation can be represented as:

$$\Delta\sigma_y = \sigma_{after\ irr} - \sigma_{before\ irr} = \Delta\sigma_{Clu} + \Delta\sigma_{Dis}. \quad (5.2)$$

As discussed earlier, APT analyses of the samples revealed presence of Mn–Si-enriched clusters in the irradiated UFG and CG steels. However, no clusters were observed in both the un-irradiated steels. Hence, the strength increase due to irradiation-induced clusters can be described using Orowan-Ashby model [118, 119] shown in Equ 5.3. It is important to note that Orowan-Ashby model is commonly used for incoherent precipitates, however previous studies [120, 121] on different alloys showed that hardening due to nano clusters modeled by Orowan model is capable of rendering explanation for observed yield stress.

$$\Delta\sigma_{Or-Ash} = M \frac{0.83Gb}{2\pi(1-\nu)^{0.5}} \frac{1}{\lambda} \ln\left(\frac{2r_s}{4b}\right) \left. \vphantom{\Delta\sigma_{Or-Ash}} \right\}, \quad (5.3)$$

$$r_s = \sqrt{\frac{2}{3}}r$$

where G is the shear modulus of the α -Fe matrix (78 GPa), b is the magnitude of the matrix Burgers vector (0.248nm), ν is the Poisson's ratio (0.33) [122], M is Taylor factor used for converting shear strength to an equivalent uniaxial yield strength (3.06) [123], r_s is the average radius of cross section of clusters on the slip planes, r is the mean radius of the clusters and λ is inter-particle spacing which describes the basic characteristics of the clusters

inside the irradiated material in terms of the their volume fraction and the average cluster radius, and is given by [118, 124]:

$$\lambda = \left(\sqrt{\frac{\pi}{f}} - 2 \right) r_s, \quad (5.4)$$

where f is the volume fraction of the clusters.

To evaluate the role of dislocations to strengthening in the CG and UFG steels, yield strength increment due to dislocation forest strengthening is given by [125]:

$$\Delta\sigma_{dis} = \alpha M G b (\sqrt{\rho_{irr}} - \sqrt{\rho_{un-irr}}), \quad (5.5)$$

where ρ_{irr} and ρ_{unirr} are dislocation densities in irradiated and unirradiated materials respectively, and α is the corresponding strengthening coefficient; for body-centered cubic metals, $\alpha=0.4$ [126]. The change in the material yield strength due to irradiation can then be found through the following equation:

$$\Delta\sigma_y = \Delta\sigma_{Or-Ash} + \Delta\sigma_{Dis} = M \frac{0.83Gb}{2\pi(1-\nu)^{0.5}} \frac{1}{\lambda} \ln\left(\frac{2r_s}{4b}\right) + \alpha M G b (\sqrt{\rho_{irr}} - \sqrt{\rho_{un irr}}), \quad (5.6)$$

Using the results obtained from both X-ray and APT analyses, the increase in yield strength due to neutron irradiation ($\Delta\sigma_y$) is calculated using Equ 5.6. Error calculations were made using error propagation method (Equ 5.7) starting from the standard deviation of the cluster size distribution (Figure 4.17) and propagating forward by finding the error in each equation leading to Equ 5.6. Calculated results for different strengthening mechanisms and their contributions to yield strength with their corresponding errors (uncertainty) are tabulated in Table 5.3.

$$\sigma_{f(x,y)} = \sqrt{\left(\frac{d}{dx} f(x, y)\right)^2 (\sigma_x)^2 + \left(\frac{d}{dy} f(x, y)\right)^2 (\sigma_y)^2} , \quad (5.7)$$

were $\sigma_{f(x,y)}$ is the standard deviation or error in the function $f(x,y)$. Both tensile yield stress measurements and strengthening mechanisms calculations illustrate similar results. Agreement between the two methods indicates that the Orowan-Ashby along with Taylor strengthening model is sufficient and can be useful for explaining the contribution of nano-cluster strengthening and dislocation forest hardening to the overall strength of the ECAP ultra-fine grained and the CG steels. The results show that while irradiation induced dislocation density has a high influence on the total irradiation induced yield stress increase in neutron irradiated CG steel, the irradiation induced hardening in the UFG steel was mainly due to the irradiation induced clusters.

Table 5.3: Estimated strength increment for both UFG and CG steels.

	$\Delta\sigma_{Oro-Ash}$ (MPa)	$\Delta\sigma_{Dis}$ (MPa)	$\Delta\sigma_{Calculated}$ (MPa)	$\Delta\sigma_{Measured}$ (Mpa)
CG Steel	137.2 ± 44.3	245 ± 35.2	382.2 ± 56.6	391 ± 26.6
UFG Steel	230.7 ± 89.7	-20.3 ± 72.6	210.4 ± 115.4	233.7 ± 50.2

Chapter 6. Conclusions and Future Work

6.1 *Summary and Conclusions*

In this work, neutron irradiation effects on UFG low carbon ferritic steel processed by ECAP were investigated after irradiation to 0.001 and 1.37 dpa doses in the PULSTAR reactor at North Carolina State University and in the ATR reactor at Idaho National Laboratory, respectively. Alterations in both microstructural and mechanical properties due to irradiation were analyzed using transmission electron microscopy, electron back scattered diffraction, atom probe tomography, X-ray diffraction, micro and nano-hardness and tensile testing. The following conclusions are drawn:

- While TEM results revealed an increase in dislocations density in irradiated CG steel, no such increase is noted in UFG steel. After irradiation to 1.37 dpa, high density of radiation-induced defects (black sand-like dots) was observed in CG steel. Quantitative XRD analysis revealed that the dislocation density in CG after irradiation to 1.37 dpa increased more than four times higher than before irradiation. However, dislocation densities in UFG steel didn't show any significant difference; a slight decrease is observed.

- High number densities of nano Mn–Si-enriched precipitates were observed in both CG and UFG steels after irradiation to 1.37 dpa. However, the number density and the radius of the clusters were larger in the case of the UFG steels due to the shorter path that the defects need to diffuse before they reach the grain boundary and hence less defect recombination probability in the matrix. The fact that these small clusters were not observed before irradiation confirms that their formation was radiation-induced.

- Nano and micro-hardness and tensile tests revealed radiation hardening in the conventional grain sized steel as expected. However, UFG steel showed minute changes after irradiation indicating less radiation hardening effect.
- Irradiation induced precipitate strengthening and irradiation produced dislocation forest strengthening were evaluated and correlated to the experimental measurements. Irradiation induced dislocation density in the UFG steel is found to be negligible and thus the change in the strength of UFG steel after irradiation is considered to be due mainly to the cluster hardening.
- As the area of grain boundaries (which act as sinks for radiation-induced point defects) is significantly increased by grain refinement, UFG steel revealed better irradiation tolerance properties. However, irradiation induced solute clustering in UFG alloys needs to be carefully considered.

6.2 *Future Work*

In this work the effect of grain size on irradiation resistance of materials was investigated on both the microstructures and mechanical properties. Current study confined to low irradiation doses and room temperature testing following neutron radiation exposures. Extensions to higher doses will shed light on the dose effects on strengthening and embrittlement. However, high irradiation doses lead to very high radioactive materials and special precautions will be needed for handling the samples during post irradiation examination. In order to avoid high residual radioactivity, charged particle irradiation can be used to reach high doses in a fast and relatively cheap manner albeit the damage may be

different from neutron radiation exposures. Light particles (ex: electrons) can be used to get further irradiation depth. As this work drew clear conclusions about the effect of high grain boundary density on radiation tolerance of ferritic steel, future research at high irradiation temperatures will elucidate the temperature effects and annealing mechanisms that may take place during irradiation. More simulation studies can also help in illustrating the interaction mechanisms between grain boundaries and irradiation induced defects for different alloys with various compositions.

Finally, as the reactor structural materials are the main enabling technology to sustain safe operation for next generation reactors, more and continued experimental results are required to produce improved reactor materials and damage tolerant designs where defects can be removed before they affect the integrity of these materials to extend the reliability and efficiency of future nuclear reactors.

References

1. OECD Nuclear Energy Agency (2000) Nuclear Energy in a Sustainable Development Perspective.
2. Cochran T, Feiveson H, Von Hippel F (2009) Fast Reactor Development in the United States. *Sci Glob Secur* 17:109–131.
3. Pryde P, Pryde L (1974) Soviet Nuclear Power: A different approach to nuclear safety. *Environ Sci Policy Sustain Dev* 16:26–34.
4. Ingersoll D (2009) Deliberately small reactors and the second nuclear era. *Prog Nucl Energy* 51:589–603.
5. (2002) U.S. DOE Nuclear Energy Research Advisory Committee. A Technology Roadmap for generation IV Nuclear Energy Systems.
6. Power Reactor Information System (PRIS), Vienna: International Atomic Energy Agency; 2014.
7. Novak S, Podest M (1987) Nuclear power plant ageing and life extension: Safety aspects. *IAEA Bull* 29:31–33.
8. Murty KL (2013) *Materials Ageing and Degradation in Light Water Reactors: Mechanisms and Management*, 1st ed. 440.
9. Murty KL, Charit I (2008) Structural materials for Gen-IV nuclear reactors: Challenges and opportunities. *J Nucl Mater* 383:189–195.
10. Zinkle SJ, Busby JT (2009) Structural materials for fission & fusion energy. *Mater Today* 12:12–19.
11. Murty KL (2012) Nuclear Materials Science: Enabling Technology for Sustained Operation of Nuclear Power Generation & Development of Next Generation Power Plants. *J Nucl Ene Sci Power Gener Tech* 1:1–3.
12. Grimes RW, Konings RJM, Edwards L (2008) Greater tolerance for nuclear materials. *Nat Mater* 7:683–5. doi: 10.1038/nmat2266
13. Allen TR, Busby JT, Klueh RL, et al. (2008) Cladding and duct materials for advanced nuclear recycle reactors. *JOM* 60:15–23.

14. Samaras M, Hoffelner W, Victoria M (2007) Modelling of advanced structural materials for GEN IV reactors. *J Nucl Mater* 371:28–36.
15. Gleiter H (1989) Nanocrystalline Materials. *Prog Mater Sci* 33:223–315.
16. Estrin Y, Vinogradov A (2013) Extreme grain refinement by severe plastic deformation: A wealth of challenging science. *Acta Mater* 61:782–817.
17. Chang Y, Guo Q, Zhang J, et al. (2013) Irradiation effects on nanocrystalline materials. *Front Mater Sci* 7:143–155.
18. Andrievski RA (2011) Behavior of Radiation Defects in Nanomaterials. *Rev Adv Mater Sci* 29:54–67.
19. Was GS (2007) *Fundamentals of Radiation Materials Science*. Springer, New York
20. Olander D (1976) *Fundamental Aspects of Nuclear Reactor Fuel Elements*. US Dept of Energy
21. Samaras M, Derlet P, Swygenhoven H Van, Victoria M (2006) Atomic scale modelling of the primary damage state of irradiated fcc and bcc nanocrystalline metals. *J Nucl Mater* 351:47–55.
22. Norris D (1972) Voids in irradiated metals (Part I). *Radiat Eff* 14:1–37.
23. Trinkaus H (1983) Energetics and formation kinetics of helium bubbles in metals. *Radiat Eff* 78:189–211.
24. Garner F, Toloczko M, Sencer B (2000) Comparison of swelling and irradiation creep behavior of fcc-austenitic and bcc-ferritic/martensitic alloys at high neutron exposure. *J Nucl Mater* 276:123–142.
25. Maziasz PJ (1993) Overview of microstructural evolution in neutron-irradiated austenitic stainless steels. *J Nucl Mater* 205:118–145.
26. Barnes RS, Mazey DJ (1960) The nature of radiation-induced point defect clusters. *Philos Mag* 5:1247–1253.
27. Murty KL, Seok CS (2001) Fracture in ferritic reactor steel—dynamic strain aging and cyclic loading. *JOM* 53:23–26.
28. Murty KL, Oh DJ (1983) Friction and Source Hardening in Irradiated Mild Steel. *Scr Metall* 17:317–320.

29. Murty KL, Charit I (2013) *An Introduction to Nuclear Materials: Fundamentals and Applications*. Wiley
30. Was GS, Wharry JP, Frisbie B, et al. (2011) Assessment of radiation-induced segregation mechanisms in austenitic and ferritic–martensitic alloys. *J Nucl Mater* 411:41–50.
31. Murty KL (1985) Interstitial-Impurity Radiation-Defect Interactions in Ferritic Steels. *JOM* 37:34–39.
32. Zinkle SJ, Was GS (2013) Materials challenges in nuclear energy. *Acta Mater* 61:735–758.
33. (2009) Integrity of reactor pressure vessels in nuclear power plants: assessment of irradiation embrittlement effects in reactor pressure vessel steels, report no NP-T-3.11. Vienna: International Atomic Energy Agency
34. (2013) Appendix H to Part 50—Reactor Vessel Material Surveillance Program Requirements. United States Nuclear Regulatory Commission.
35. Odette GR, Lucas GE (2001) Embrittlement of Nuclear Reactor Pressure Vessels. *JOM* 53:18–22.
36. Miller MK, Russell KF (2007) Embrittlement of RPV steels: An atom probe tomography perspective. *J Nucl Mater* 371:145–160.
37. Haywood B (2010) Post Weld Heat Treating (PWHT) failure - Safety Engineering Network (SAFTENG). *Saf. Eng. Netw.*
38. Odette GR, Nanstad RK (2009) Predictive reactor pressure vessel steel irradiation embrittlement models: Issues and opportunities. *JOM* 61:17–23.
39. Valiev RZ (2008) On Grain Boundary Engineering of UFG Metals and Alloys for Enhancing their Properties. *Mater Sci Forum* 584-586:22–28.
40. Koch CC, Ed. (2007) *Nanostructured Materials: Processing, Properties and Potential Applications*, second. Norwich
41. Cheung C, Palumbo G, Erb U (1994) Synthesis of Nanocrystalline Permalloy by Electrodeposition. *Scr Metall Mater* 31:735–740.
42. Averback RS, Höfler HJ, Tao R (1993) Processing of nano-grained materials. *Mater Sci Eng A* 166:169–177.

43. Valiev R, Islamgaliev R, Alexandrov I (2000) Bulk nanostructured materials from severe plastic deformation. *Prog Mater Sci* 45:103–189.
44. Zhilyaev A, Langdon T (2008) Using high-pressure torsion for metal processing: Fundamentals and applications. *Prog Mater Sci* 53:893–979.
45. Stolyarov V, Zhu Y, Alexandrov I, et al. (2001) Influence of ECAP routes on the microstructure and properties of pure Ti. *Mater Sci Eng A* 299:59–67.
46. Valiev R, Langdon TG (2006) Developments in the use of ECAP processing for grain refinement. *Rev Adv Mater* 13:15–26.
47. Iwahashi Y, Wang J, Horita Z, et al. (1996) Principle of Equal-Channel Angular Pressing for the Processing of Ultra-Fine Grained Materials. *Scr Mater* 35:143–146.
48. Nakashima K, Horita Z, Nemoto M, Langdon TG (2000) Development of a multi-pass facility for equal-channel angular pressing to high total strains. *Mater Sci Eng A* 281:82–87.
49. Furukawa M, Iwahashi Y, Horita Z, et al. (1998) The shearing characteristics associated with equal-channel angular pressing. *Mater Sci Eng A* 257:328–332.
50. Segal VM (1995) Materials processing by simple shear. *Mater Sci Eng A* 197:157–164.
51. Wurster S, Pippin R (2009) Nanostructured metals under irradiation. *Scr Mater* 60:1083–1087.
52. Beyerlein IJ, Caro A, Demkowicz MJ, et al. (2013) Radiation damage tolerant nanomaterials. *Mater Today* 16:443–449.
53. Singh BN (1974) Effect of grain size on void formation during high energy electron irradiation of austenitic stainless steel. *Philos Mag* 29:1:25–42.
54. Rose M (1997) Instability of irradiation induced defects in nanostructured materials. *Nucl Instruments Methods Phys Res* 128:119–122.
55. Chimi Y, Iwase A, Ishikawa N, et al. (2001) Accumulation and recovery of defects in ion-irradiated nanocrystalline gold. *J Nucl Mater* 297:355–357.
56. Nita N, Schaeublin R, Victoria M, Valiev RZ (2005) Effects of irradiation on the microstructure and mechanical properties of nanostructured materials. *Philos Mag* 85:723–735.

57. Matsuoka H, Yamasaki T, Zheng YJ, et al. (2007) Microstructure and mechanical properties of neutron-irradiated ultra-fine-grained SUS316L stainless steels and electrodeposited nanocrystalline Ni and Ni–W alloys. *Mater Sci Eng A* 449-451:790–793.
58. Yamasaki T, Schlobmacher P, Ehrlich K, Ogino Y (1998) Formation of Amorphous Electrodeposited Ni-W Alloys and Their Nanocrystallization. *NanoStructured Mater* 10:375–388.
59. Kurishita H, Kobayashi S, Nakai K, et al. (2008) Development of ultra-fine grained W–(0.25–0.8)wt%TiC and its superior resistance to neutron and 3MeV He-ion irradiations. *J Nucl Mater* 377:34–40.
60. Sun C, Yu KY, Lee JH, et al. (2012) Enhanced radiation tolerance of ultrafine grained Fe–Cr–Ni alloy. *J Nucl Mater* 420:235–240.
61. Wang S, Lumpkin G, Wang L, Ewing R (2000) Ion irradiation-induced amorphization of six zirconolite compositions. *Nucl Instruments Methods Phys Res Sect B Beam Interact with Mater Atoms* 166-167:293–298.
62. Plewnia A, Heinz B, Ziemann P (1999) Amorphization of metal films by low temperature ion irradiation . An in situ PAC-study for AuIn₂ and In₃Pd films. *Nucl Instruments Methods Phys Res Sect B Beam Interact with Mater Atoms* 148:901–906.
63. Meldrum A, Boatner L, Ewing R (2003) Size effects in the irradiation-induced crystalline-to-amorphous transformation. *Nucl Instruments Methods Phys Res Sect B Beam Interact with Mater Atoms* 207:28–35.
64. Kilmametov AR, Gunderov DV, Valiev RZ, et al. (2008) Enhanced ion irradiation resistance of bulk nanocrystalline TiNi alloy. *Scr Mater* 59:1027–1030.
65. Jiang W, Wang H, Kim I, et al. (2009) Response of nanocrystalline 3C silicon carbide to heavy-ion irradiation. *Phys Rev B* 80:161301.
66. Shen TD, Feng S, Tang M, et al. (2007) Enhanced radiation tolerance in nanocrystalline MgGa₂O₄. *Appl Phys Lett* 90:263115.
67. Ovid'ko I, Sheinerman A (2004) Irradiation-induced amorphization processes in nanocrystalline solids. *Appl Phys A* 81:1083–1088.
68. Voegeli W, Albe K, Hahn H (2003) Simulation of grain growth in nanocrystalline nickel induced by ion irradiation. *Nucl Instruments Methods Phys Res Sect B Beam Interact with Mater Atoms* 202:230–235.

69. Rose M, Gorzawski G, Miehe G, et al. (1995) Phase stability of nanostructured materials under heavy ion irradiation. *NanoStructured Mater* 6:731–734.
70. Radiguet B, Etienne A, Pareige P, et al. (2008) Irradiation behavior of nanostructured 316 austenitic stainless steel. *J Mater Sci* 43:7338–7343.
71. Kaoumi D, Motta A, Birtcher R (2008) A thermal spike model of grain growth under irradiation. *J Appl Phys* 104:073525.
72. Nita N, Schaeublin R, Victoria M (2004) Impact of irradiation on the microstructure of nanocrystalline materials. *J Nucl Mater* 329-333:953–957.
73. Stoller RE, Odette GR, Wirth BD (1997) Primary damage formation in bcc iron. *J Nucl Mater* 251:49–60.
74. Bacon DJ, Diaz de la Rubia T (1994) Molecular dynamics computer simulations of displacement cascades in metals. *J Nucl Mater* 216:275–290.
75. Millett P, Aidh D, Desai T, et al. (2009) Grain-boundary source/sink behavior for point defects: An atomistic simulation study. *Int J Mater Res* 100:550.
76. Mohamed W (2012) Influence of Fast Neutron Irradiation on Mechanical Properties and Microstructure of Nanocrystalline Copper. PhD Dissertation / North Carolina State University
77. Bai X, Voter AF, Hoagland RG, et al. (2010) Efficient annealing of radiation damage near grain boundaries via interstitial emission. *Science* 327:1631–1634.
78. Samaras M, Derlet P, Van Swygenhoven H, Victoria M (2002) Computer Simulation of Displacement Cascades in Nanocrystalline Ni. *Phys Rev Lett* 88:125505.
79. ASTM E170-10 (2010) Standard Terminology Relating to Radiation Measurements and Dosimetry.
80. Mascitti J, Madariaga M (2011) Method for the Calculation of DPA in the Reactor Pressure Vessel of Atucha II. *Sci Technol Nucl Install* 2011:1–6.
81. Greenwood LR (1994) Neutron interactions and atomic recoil spectra. *J Nucl Mater* 216:29–44.
82. ASTM E261-10 Standard Practice for Determining Neutron Fluence , Fluence Rate , and Spectra by radioactivation Techniques.

83. Kuijpers L, Herzing R, Cloth P, Jilich K (1977) On The Determination Of Fast Neutron Spectra With Activation Techniques ; Its Application In A Fusion Reactor Blanket Model. Nucl Instruments Methods 144:215–224.
84. Knoll GF (2000) Radiation Detection and Measurement. Wiley
85. Negoita CC (2004) Measurement of Neutron Flux Spectra in a Tungsten Benchmark by Neutron Foil Activation Method. PhD Dissertation / Dresden University of Technology
86. Tsoulfanidis N, Landsberger S (2010) Measurement and Detection of Radiation. CRC Press
87. Evaluated Nuclear Data File (ENDF/B-VII.1).
88. Perey FG (1977) Least-Squares Dosimetry Unfolding: The Program STAY'SL.
89. L. R. Greenwood, Smither RK (1985) SPECTER: Neutron Damage Calculations for materials Irradiations.
90. (2012) Chart of Nuclides (official web site of the IAEA).
91. (2012) Lawrence Berkeley National Laboratory (Online).
92. (2012) WebElements Periodic Table of the Elements (Online).
93. Alsabbagh A, Xiao Z, Hawari A (2010) Developing Neutron Tomography Capabilities at the PULSTAR Reactor. Trans Am Nucl Soc 103:229–230.
94. Marshall F (2005) Advanced Test Reactor Testing Experience – Past , Present , and Future. Proc. Int. Symp. Res. React. Neutron Sci.
95. Hibbit, Karlsson, Sorensen. Abaqus, Abaqus User's manual (2011) ABAQUS.
96. X-5 Monte Carlo Team, MCNP LANL (2003) X-5 Monte Carlo Team, MCNP – A general Monte Carlo N-particle transport code.
97. Cerezo A, Clifton P, Galtrey M, et al. (2007) Atom probe tomography today. Mater Today 10:36–42.
98. Miller MK (2000) Atom probe tomography : analysis at the atomic level. Kluwer Academic, New York

99. Oliver W, Pharr G (1992) An improved technique for determining hardness and elastic modulus using load and displacement sensing indentation experiments. *J Mater Res* 6:1564.
100. Johnson R, Lam N (1976) Solute segregation in metals under irradiation. *Phys Rev B* 13:4364.
101. Lutterotti L, Scardi P (1990) Simultaneous structure and size-strain refinement by the Rietveld method. *J Appl Crystallogr* 23:246–252.
102. H. M. Rietveld (1967) Line profiles of neutron powder-diffraction peaks for structure refinement. *Acta Cryst* 22:151.
103. Chowdhury PS, Sarkar A, Mukherjee P, et al. (2010) Studies of microstructural imperfections of powdered Zirconium-based alloys. *Mater Charact* 61:1061–1065.
104. Williamson GK, Smallman RE (1956) Dislocation densities in some annealed and cold-worked metals from measurements on the X-ray debye-scherrer spectrum. *Philos Mag* 1:34–46.
105. McLean D (1957) *Grain Boundaries in Metals*. Oxford University Press, London
106. Smallman RE, Bishop RJ (1999) *Modern Physical Metallurgy and Materials Engineering: Science, Process, Applications*, 6th ed. 438.
107. Allen TR, Busby JT, Was GS, Kenik EA (1998) On the mechanism of radiation-induced segregation in austenitic Fe–Cr–Ni alloys. *J Nucl Mater* 255:44–58.
108. Hyde JM, Marquis EA, Wilford KB, Williams TJ (2011) A sensitivity analysis of the maximum separation method for the characterisation of solute clusters. *Ultramicroscopy* 111:440–7.
109. Vaumousse D, Cerezo A, Warren PJ (2003) A procedure for quantification of precipitate microstructures from three-dimensional atom probe data. *Ultramicroscopy* 95:215–221.
110. Marquis E, Hyde JM (2010) Applications of atom-probe tomography to the characterisation of solute behaviours. *Mater Sci Eng R* 69:37–62.
111. Murty KL (1999) Role and significance of source hardening in radiation embrittlement of iron and ferritic steels. *J Nucl Mater* 270:115–128.

112. Sneddon IANN (1965) The Relation between Load and Penetration in the Axisymmetric Boussinesq Problem for a Punch of Arbitrary Profile. *Int J Eng Sci* 3:47–57.
113. Bolshakov A, Pharr GM (2011) Influences of pileup on the measurement of mechanical properties by load and depth sensing indentation techniques. *J Mater Res* 13:1049–1058.
114. Qian L, Li M, Zhou Z, et al. (2005) Comparison of nano-indentation hardness to microhardness. *Surf Coatings Technol* 195:264–271.
115. Bolshakov A, Oliver WC, Pharr GM (2011) Influences of stress on the measurement of mechanical properties using nanoindentation: Part II. Finite element simulations. *J Mater Res* 11:760–768.
116. Charit I, Seok CS, Murty KL (2007) Synergistic effects of interstitial impurities and radiation defects on mechanical characteristics of ferritic steels. *J Nucl Mater* 361:262–273.
117. Ashby M, Jones D (1996) *Engineering Materials 1*, second edi. Butterworth-Heinemann, Oxford
118. Anand L, Gurland J (1976) Effect of Internal Boundaries on the Yield Strengths of Spheroidized Steels. *Metall Trans A* 7:191.
119. Martin J (1980) *Micromechanisms in particle-hardened alloys*. Cambridge University Press
120. Lambrecht M, Meslin E, Malerba L, et al. (2010) On the correlation between irradiation-induced microstructural features and the hardening of reactor pressure vessel steels. *J Nucl Mater* 406:84–89.
121. Bergner F, Pareige C, Hernández-Mayoral M, et al. (2014) Application of a three-feature dispersed-barrier hardening model to neutron-irradiated Fe–Cr model alloys. *J Nucl Mater* 448:96–102.
122. Park K-T, Kim Y-S, Lee JG, Shin DH (2000) Thermal stability and mechanical properties of ultrafine grained low carbon steel. *Mater Sci Eng A* 293:165–172.
123. Stoller RE, Zinkle SJ (2000) On the relationship between uniaxial yield strength and resolved shear stress in polycrystalline materials. *J Nucl Mater* 283-287:349–352.
124. Hsu CJ, Chang CY, Kao PW, et al. (2006) Al–Al₃Ti nanocomposites produced in situ by friction stir processing. *Acta Mater* 54:5241–5249.

125. Ashby M (1971) Strengthening methods in crystals.

126. Courtney T (2000) Mechanical Behavior of Materials, second. 179.

Appendices

Appendix A

Dislocation Densities and Their Associated Error Calculations

X-ray diffraction line profile analyses have been applied on the UFG and CG steel before and after irradiation to 1.37 dpa to characterize the microstructural parameters like domain size, microstrain and dislocation density. The average dislocation density was estimated using the equations described in section 4.2. In this appendix, the dislocation density calculations and their associated error calculations are presented for each case where *unirr* represents the as-received (not irradiated) case and *irr* represents the case of samples irradiated to 1.37 dpa.

Dislocation Density Obtained from XRD measurements

Unirr CG

$$D_s := 1850 \cdot 10^{-10} \text{ m} \quad \text{error}_{D_s} := 12 \cdot 10^{-10} \text{ m}$$

$$\epsilon_L := 7.4 \cdot 10^{-4} \quad \text{error}_{\epsilon_L} := 0.9 \cdot 10^{-4}$$

$$b := 0.248 \text{ nm}$$

$$k := 14.4$$

$$\rho_D := \frac{3}{D_s^2} = 8.766 \times 10^{13} \frac{1}{\text{m}^2}$$

$$\rho_s := \frac{(k \cdot \epsilon_L^2)}{b^2} = 1.282 \times 10^{14} \frac{1}{\text{m}^2}$$

$$\rho := (\rho_D \cdot \rho_s)^{0.5} = 1.06 \times 10^{14} \frac{1}{\text{m}^2}$$

$$\text{error}_{\rho, D} := \left[\left(\frac{d}{dD_s} \frac{3}{D_s^2} \right)^2 \cdot \text{error}_{D_s}^2 \right]^{0.5} = 1.137 \times 10^{12} \frac{1}{\text{m}^2}$$

$$\text{error}_{\rho, s} := \left[\left[\frac{d}{d\epsilon_L} \frac{(k \cdot \epsilon_L^2)}{b^2} \right]^2 \cdot \text{error}_{\epsilon_L}^2 \right]^{0.5} = 3.119 \times 10^{13} \frac{1}{\text{m}^2}$$

$$\text{error}_{\rho} := \left[\left[\frac{d}{d\rho_D} (\rho_D \cdot \rho_s)^{0.5} \right]^2 \cdot \text{error}_{\rho, D}^2 + \left[\frac{d}{d\rho_s} [(\rho_D \cdot \rho_s)^{0.5}] \right]^2 \cdot \text{error}_{\rho, s}^2 \right]^{0.5} = 1.291 \times 10^{13} \frac{1}{\text{m}^2}$$

Irr CG

$$D_s := 622 \cdot 10^{-10} \text{ m} \quad \text{error}_{D,s} := 8 \cdot 10^{-10} \text{ m}$$

$$\epsilon_L := 10 \cdot 10^{-4} \quad \text{error}_{\epsilon L} := 1.3 \cdot 10^{-4}$$

$$\rho_D := \frac{3}{D_s^2} = 7.754 \times 10^{14} \frac{1}{\text{m}^2}$$

$$\rho_s := \frac{(k \cdot \epsilon_L^2)}{b^2} = 2.341 \times 10^{14} \frac{1}{\text{m}^2}$$

$$\rho := (\rho_D \cdot \rho_s)^{0.5} = 4.261 \times 10^{14} \frac{1}{\text{m}^2}$$

$$\text{error}_{\rho,D} := \left[\left(\frac{d}{dD_s} \frac{3}{D_s^2} \right)^2 \cdot \text{error}_{D,s}^2 \right]^{0.5} = 1.995 \times 10^{13} \frac{1}{\text{m}^2}$$

$$\text{error}_{\rho,s} := \left[\left(\frac{d}{d\epsilon_L} \frac{(k \cdot \epsilon_L^2)}{b^2} \right)^2 \cdot \text{error}_{\epsilon L}^2 \right]^{0.5} = 6.087 \times 10^{13} \frac{1}{\text{m}^2}$$

$$\text{error}_{\rho} := \left[\left[\frac{d}{d\rho_D} (\rho_D \cdot \rho_s)^{0.5} \right]^2 \cdot \text{error}_{\rho,D}^2 + \left[\frac{d}{d\rho_s} [(\rho_D \cdot \rho_s)^{0.5}] \right]^2 \cdot \text{error}_{\rho,s}^2 \right]^{0.5} = 5.566 \times 10^{13} \frac{1}{\text{m}^2}$$

Unirr UFG

$$D_s := 385 \cdot 10^{-10} \text{ m} \quad \text{error}_{D,s} := 3 \cdot 10^{-10} \text{ m}$$

$$\epsilon_L := 13.8 \cdot 10^{-4} \quad \text{error}_{\epsilon_L} := 1.8 \cdot 10^{-4}$$

$$\rho_D := \frac{3}{D_s^2} = 2.024 \times 10^{15} \frac{1}{\text{m}^2}$$

$$\rho_s := \frac{(k \cdot \epsilon_L^2)}{b^2} = 4.459 \times 10^{14} \frac{1}{\text{m}^2}$$

$$\rho := (\rho_D \cdot \rho_s)^{0.5} = 9.4997 \times 10^{14} \frac{1}{\text{m}^2}$$

$$\text{error}_{\rho,D} := \left[\left(\frac{d}{dD_s} \frac{3}{D_s^2} \right)^2 \cdot \text{error}_{D,s}^2 \right]^{0.5} = 3.154 \times 10^{13} \frac{1}{\text{m}^2}$$

$$\text{error}_{\rho,s} := \left[\left(\frac{d}{d\epsilon_L} \frac{(k \cdot \epsilon_L^2)}{b^2} \right)^2 \cdot \text{error}_{\epsilon_L}^2 \right]^{0.5} = 1.163 \times 10^{14} \frac{1}{\text{m}^2}$$

$$\text{error}_{\rho} := \left[\left[\frac{d}{d\rho_D} (\rho_D \cdot \rho_s)^{0.5} \right]^2 \cdot \text{error}_{\rho,D}^2 + \left[\frac{d}{d\rho_s} [(\rho_D \cdot \rho_s)^{0.5}] \right]^2 \cdot \text{error}_{\rho,s}^2 \right]^{0.5} = 1.241 \times 10^{14} \frac{1}{\text{m}^2}$$

Irr UFG

$$D_s := 366 \cdot 10^{-10} \text{ m} \quad \text{error}_{D,s} := 7 \cdot 10^{-10} \text{ m}$$

$$\epsilon_L := 12.4 \cdot 10^{-4} \quad \text{error}_{\epsilon L} := 1.9 \cdot 10^{-4}$$

$$\rho_D := \frac{3}{D_s^2} = 2.24 \times 10^{15} \frac{1}{\text{m}^2}$$

$$\rho_s := \frac{(k \cdot \epsilon_L^2)}{b^2} = 3.6 \times 10^{14} \frac{1}{\text{m}^2}$$

$$\rho := (\rho_D \cdot \rho_s)^{0.5} = 8.979 \times 10^{14} \frac{1}{\text{m}^2}$$

$$\text{error}_{\rho,D} := \left[\left(\frac{d}{dD_s} \frac{3}{D_s^2} \right)^2 \cdot \text{error}_{D,s}^2 \right]^{0.5} = 8.567 \times 10^{13} \frac{1}{\text{m}^2}$$

$$\text{error}_{\rho,s} := \left[\left(\frac{d}{d\epsilon_L} \frac{(k \cdot \epsilon_L^2)}{b^2} \right)^2 \cdot \text{error}_{\epsilon L}^2 \right]^{0.5} = 1.103 \times 10^{14} \frac{1}{\text{m}^2}$$

$$\text{error}_{\rho} := \left[\left[\frac{d}{d\rho_D} (\rho_D \cdot \rho_s)^{0.5} \right]^2 \cdot \text{error}_{\rho,D}^2 + \left[\frac{d}{d\rho_s} (\rho_D \cdot \rho_s)^{0.5} \right]^2 \cdot \text{error}_{\rho,s}^2 \right]^{0.5} = 1.386 \times 10^{14} \frac{1}{\text{m}^2}$$

Appendix B

Calculated Irradiation Induced Dislocation Density

Irradiation-induced dislocation density was measured directly from XRD analysis. However, it can also be calculated using Equ 5.6 assuming that $\Delta\sigma_y$ is the measured change in yield stress. Rearranging Equ 5.6:

$$\Delta\rho^* = \left(\sqrt{\rho_{irr}} - \sqrt{\rho_{unirr}}\right) = \frac{\Delta\sigma_y - \Delta\sigma_{Or-Ash}}{\alpha M G b} = \frac{\Delta\sigma_y - M \frac{0.83 G b}{2\pi(1-\nu)^{0.5}} \frac{1}{\lambda} \ln\left(\frac{2r_s}{4b}\right)}{\alpha M G b} \quad (B.1)$$

The associated error (uncertainty) for calculated and measured changes in dislocation density, $\Delta\rho^*$ can be obtained using Equ 5.7:

$$error_{\Delta\rho^* (calculated)} = \sqrt{\left(\frac{1}{M \alpha G b}\right)^2 \cdot (error_{\Delta\sigma_y, measured})^2 + \left(\frac{1}{M \alpha G b}\right)^2 \cdot (error_{\Delta\sigma_{Or-Ash}})^2} \quad (B.2)$$

$$error_{\Delta\rho^* (measured)} = \sqrt{\left(\frac{1}{2\sqrt{\rho_{irr}}}\right)^2 \cdot (error_{\rho_{irr}})^2 + \left(\frac{1}{2\sqrt{\rho_{unirr}}}\right)^2 \cdot (error_{\rho_{unirr}})^2} \quad (B.3)$$

The error values used in equations B.2 and B.3 are given in Table 5.3 and Table 4.2, respectively. Table B.1 delineates the corresponding change in dislocation density after irradiation for both UFG and CG steels. As expected from the previous results, the calculated and measured values show a good agreement. The dislocations density in UFG steel didn't show any significant change and $\Delta\rho^*$ was about zero, while in CG steel substantial increase in dislocation density after irradiation was observed.

Table B.1: Irradiation-induced dislocation density for both UFG and CG steels.

	$\Delta\rho^*_{Measured} (\times 10^6 \text{ m}^{-1})$	$\Delta\rho^*_{Calculated} (\times 10^6 \text{ m}^{-1})$
UFG Steel	-0.86±3.07	0.13±4.34
CG Steel	10.35±1.49	10.72±2.19